



Royal Netherlands
Meteorological Institute
Ministry of Infrastructure and the Environment

Sentinel-4 Level-2 ATBD
Total and Tropospheric NO_2



Document ID	:	S4-L2-IUP_KNMI-ATBD-2004
Authors	:	A.F.J. Sanders, A. Richter, H. Eskes
Issue	:	4.5
Date	:	2026-06-30
Status	:	Final
Class	:	Unclassified – Releasable to the Public
DOI	:	https://doi.org/10.5281/zenodo.15359616

© University of Bremen, 2026. The copyright in this document is vested in University of Bremen. This document may only be reproduced in whole or in part, or stored in a retrieval system, or transmitted in any form, or by any means electronic, mechanical, photocopying or otherwise, either with the prior permission of University of Bremen or in accordance with the terms of ESA Contract No. 4000114101/15/NL/MP.

Document approval record

	digital signature	
prepared:	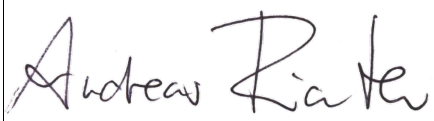	
		---
checked:	S4 L2 team	
approved PM:		Digitally signed by Dr.-Ing. Diego Loyola 2026.06.29 13:57:34+02'00'
approved CM:	Ronny Lutz	Digitally signed by Ronny Lutz DN: C=DE, CN=Ronny Lutz, O=Deutsches Zentrum fuer Luft- und Raumfahrt e. V. (DLR), ST=Nordrhein-Westfalen, E=ronny.lutz@dlr.de, postalCode=51147, street=Linder Höhe Reason: I am approving this document Location: Oberpfaffenhofen Date: 2026.06.29 12:53:05+02'00' Foxit PDF Reader Version: 2026.1.1

Document change record

Issue	Date	Section	Comments
0.5.0	2014-06-26	All	First draft.
0.6.0	2016-05-18	-	Released for internal review by S4 L2 Team.
0.6.1	2016-06-08	All	Updated with feedback from S4 L2 Team; completed ATBD for System Requirement Review.
1.0.0	2016-06-08	-	Released for System Requirement Review.
1.0.1	2016-09-15	 3.1 5.2.4 4.5, 4.6.4, 5.5.4 4.5, 4.6.3, 5.4.1 4.3, 5.4.2 5.4.2, 6.1.2 6.3 2.2	Updated in response to System Requirement Review (changes highlighted): BV-NO2-01 (definition of terms) BV-NO2-02 (high-sampling interpolation) BV-NO2-03 (regional model baseline) BV-NO2-04 (global model baseline) BV-NO2-04 (TM5 commitment and development) OLR-NO2-01 (clarification of auxiliary data) OLR-NO2-02 (output product file size) OLR-NO2-03 (document reference)
1.0.2	2016-09-15	4.6, 5.2-5 All	Many clarifications, additions and some restructuring. Minor corrections and clarifications throughout the ATBD.
1.1.0	2016-09-15	-	Updated release following System Requirement Review.
1.1.1	2017-03-01	All	Many clarifications, additions and restructuring.
1.2.0	2017-03-01	-	Released for internal review by S4 L2 Team.
1.2.1	2017-04-10	All	Updated with feedback from S4 L2 Team; completed ATBD for Preliminary Design Review.
1.5.0	2017-04-10	-	Released for Preliminary Design Review.
1.5.1	2017-06-30	 5.6.2 2, 5.2.3 6.1.2 - 7.2.2 5.5.8 - 6.4 -	Updated in response to Preliminary Design Review (changes highlighted in yellow): MA-ATBD_NO2-01 (covariance matrix from CAMS) OLR-ATBD_NO2-[01-09,10] (references and caption) OLR-ATBD_NO2-11 (table with L1b data) OLR-ATBD_NO2-12 [answered elsewhere] OLR-ATBD_NO2-13 (error budget) BV-NO2-01 (inconsistent cloud input data) BV-NO2-02 [no action needed] MA-PUM_NO2-01 (errors needed for assimilation) MA-PUM_NO2-02 [a priori profiles not needed in output]
1.5.2	2017-06-30	All	Various other modifications (most important ones highlighted in red).
1.6.0	2017-06-30	-	Updated release following Preliminary Design Review.
1.6.1	2018-12-17	 2.2 6.1.2 5.5.9	Updated in response to open RIDs at the close-out of the Preliminary Design Review (see minutes): - references to ESA internal technotes removed - naming of L1b product corrected - alternative implementation for cloud treatment enforces radiometric closure
1.6.2	2018-12-17	 5.5.4.4, 6.1.3 6.3	Updated following the Critical Design Review: BV_DLR_DPM_10 (spatial interpolation GSR coefficients) NW-33 (SRS) (variability computation time)
1.6.2	2018-12-17	 5.5.4 4.2, 6.2.3, 6.4	Updates to (see presentation at PM14) - description of the treatment of directional surface reflectance

		6.4 5.2.3.2 5.5.9	- table summarizing main user applications and related output variables - list of variables in output product and associated variable names (harmonization between NO2, SO2, HCHO and CHOCHO) - description of spectral calibration - cloud correction
1.6.3	2018-12-17	 4.6.7, 5.5.4.4, 5.5.5 6.1.8 5.4.4 6.1.5 All	Further updates to - discussion of possibility of look-up table or online calculations for box air mass factors - listed configurable parameters - description of model bias corrections - described BG engineering product - list of processing flags updated and harmonized between NO2, SO2, HCHO and CHOCHO processors - many minor modifications throughout
1.6.4	2018-12-17	5.5.8	Description of model data pre-processing moved to and continued in a separate document (ECA ATBD, [RD10]).
2.0.0	2018-12-17	-	Released for review by ESA
2.0.1	2019-06-28	 2.1, 4.4 6.3 5.5.7, 5.5.8, 6.1.3, 6.1.4, 6.4	Update following review. NO2-ATBD-1: update ref for reqs. NO2-ATBD-2: updated allocated core minutes in PP/OP. ALL-ATBDs-2: updated ECA input variables, removed boundary layer wind.
2.0.2	2019-06-28	6.1.5 6.1.8 6.4 6.1.6 6.1.2	- Updated description of BG product. - Listed processor configuration parameters. - Specified breakpoint variables. - Updated table with DOAS common processor elements. - Minor clarifications.
2.1.0	2019-06-28	-	Updated release for CDR close-out.
3.0	2021-12-17	7.3	Added section on cloud uncertainties Updated references
3.1	2022-03-31	6.4	- Removed draft status - Finalised Table 6.12 - Removed last TBDs - Updated Table 6.7 for consistency with other lv2 products
3.5	2023-09-29	6.2 6.2.4 6.1.8 All All 5.4 5.5 5.6	- Updated discussion of error and warning flags - Updated description of QA value computation - Updated BG processor configurable parameters - Adding of missing information, correction of typos, improvement of consistency - Removed outdated descriptions of bread-board algorithm - Updated description of BG processor - Updated discussion of BAMF calculations - Updated discussion on error calculation

3.6	2023-11-30	2 all 6.4 6.4 6.4 all	- Updated references - Removed references to HSC product (RIDs OLR-13, OLR-21) - Corrected wavelength for aerosol properties (RID OLR-17) - Renamed “static backup” columns in Table 6.1 and Table 6.3 (RID NW-28) - Updated Table 6.6 (RID NW-29) - Reorganised discussion of processor options and included a section on Future Developments (Section 5.8) (RID OLR-19)
3.7	2023-12-13		- Changed tropopause pressure to tropopause index (RID OLR-20) - Clarified initialisation and error handling with respect to the background processor (RID OLR-9).
3.9	2024-02-29		- preparation for public release
4.0	2025-06-30	5.2.2	- added description of pseudo cross-sections - updated references - release version for L2OP v2+
4.1	2025-08-18	5.2.2, 5.8.2	- added link to and example of inhomogeneity tests performed on GEMS data - updated references
4.5	2026-06-30	6.1.8,6.2.2, 6.2.3	- updated flags - update QA thresholds - updated variable naming - updated background processor product description - version for L2OP v2.7

Contents

Document approval record **2**
Document change record **3**
Contents **6**
1 Introduction to the document **9**
1.1 Purpose 9
1.2 Document overview 9
1.3 Acknowledgements 9
2 Applicable and reference documents, electronic references **11**
2.1 Applicable documents 11
2.2 Reference documents 11
2.3 Electronic references 12
3 Terms, symbols and abbreviations **13**
3.1 Terms and symbols 13
3.2 Abbreviations 16
4 Introduction to the Sentinel-4 NO_2 product **19**
4.1 Sentinel-4 UVN 19
4.2 Product description 22
4.3 Heritage 25
4.4 Product requirements 27
4.5 Overview of the retrieval method 28
5 Algorithm description **30**
5.1 Overview 30
5.2 Spectral fit (DOAS) 31
5.2.1 Background 31
5.2.2 Reference spectra and absorption cross-sections 36
5.2.3 Spectral calibration and interpolation, treatment of outliers 40
5.3 Separation of stratospheric and tropospheric columns (STRAT) 42
5.3.1 Background 42
5.3.2 Model forecast with data assimilation 44
5.4 Background corrections (BG) 44
5.4.1 Background 44
5.4.2 Pixel selection 46
5.4.3 Stripe offsets 46
5.4.4 Model biases 48
5.5 Calculation of air mass factors (AMF) 49
5.5.1 Background 49
5.5.2 Air mass factor for the fit window 54
5.5.3 Radiative transfer modelling 55
5.5.4 Directional surface reflectance 57
5.5.5 Treatment of aerosols 63
5.5.6 Look-up tables of box air mass factors 63
5.5.7 A priori NO_2 and temperature profiles, surface pressures and other model data 64
5.5.8 Pre-processing of model data 65
5.5.9 Cloud parameters for the NO_2 fit window 66
5.5.10 Column air mass factor for a clear, cloudy and partly cloudy atmosphere 67
5.5.11 Temperature correction 69
5.6 Characterisation and error analysis 70
5.6.1 Averaging kernels and air mass factors 70
5.6.2 Error propagation for the vertical columns 72

5.6.3 Averaging kernels and smoothing errors....78
5.7 Corrections for instrument or model errors....79
5.7.1 De-striping of slant columns....79
5.7.2 Scene heterogeneity....79
5.7.3 Thermal variation of ISRFs in orbit....80
5.7.4 Spectral mis-registration of radiance and irradiance....81
5.7.5 Intra-band and inter-band spatial mis-registration....82
5.7.6 Polarisation sensitivity....82
5.8 Future Developments....83
5.8.1 DOAS fitting....83
5.8.2 Scene heterogeneity....83
5.8.3 Spectral mis-registration....83
5.8.4 Polarisation sensitivity....84
5.8.5 AMF calculation....85
5.8.6 Directional effects of surface reflectance....85
5.8.7 Aerosols....85
5.8.8 Cloud Radiance fraction....86
5.8.9 Stratospheric Correction....86
6 Feasibility....87
6.1 Processing approach....87
6.1.1 Overview....87
6.1.2 Level-1b data requirements....87
6.1.3 Auxiliary data requirements....89
6.1.4 Dependence on other Level-2 products....92
6.1.5 BG engineering product....93
6.1.6 Common processor elements....93
6.1.7 Pixel selection....96
6.1.8 Configurable parameters....96
6.2 S4 NO_2 quality assurance....100
6.2.1 Overview....100
6.2.2 S4 NO_2 processing errors and warnings....100
6.2.3 S4 NO_2 user flags....103
6.2.4 Quality Assurance value....105
6.3 Estimated computational effort and timeliness....105
6.4 S4 NO_2 data product description....106
7 Retrieval characterisation and error analysis....112
7.1 Vertical sensitivity....112
7.1.1 Box air mass factors....112
7.1.2 Averaging kernels....114
7.2 Error budget....117
7.2.1 Approach....117
7.2.2 Error budget for previous instruments....117
7.2.3 Errors in fitted slant columns....119
7.2.4 Errors in stratospheric slant columns....122
7.2.5 Errors in tropospheric column air mass factors....122
7.2.6 Expected total error in tropospheric NO_2 columns....122
7.3 Other sensitivity studies....124
7.3.1 Temperature dependence of the ISRF....124
7.3.2 Cloud Threshold values....126
8 Validation....130
8.1 Validation requirements....130
8.2 Algorithm testing and verification....130

8.3 Stratospheric NO_2 validation 131
8.4 Tropospheric NO_2 validation 131
9 Discussion and conclusions 133
10 References 134

1 Introduction to the document

1.1 Purpose

The present document is the Algorithm Theoretical Basis Document (ATBD) for the Sentinel-4 (S4) Level-2 (L2) algorithm that will deliver total and tropospheric nitrogen dioxide (NO_2) column amounts. The purpose of the ATBD is to provide the theoretical basis for the algorithm and to describe the corresponding data product (identifier: S4-L2-NO2). This ATBD is a joint effort of the Institut für Umweltphysik in Bremen (IUP, Universität Bremen, Bremen, Germany; development lead) and the Koninklijk Nederlands Meteorologisch Instituut (KNMI, De Bilt, Netherlands).

Within the Sentinel-4 Level-2 project, development of an operational product proceeds in several steps. The consolidated algorithm is implemented as a science code or bread-board algorithm and is run at the developer team's host institute (for NO_2, this is IUP Bremen). Based on the bread-board algorithm a prototype and an operational processor are developed at the Deutsches Zentrum für Luft- und Raumfahrt (DLR, Oberpfaffenhofen, Germany). The L2 Prototype Processor (L2PP) will be run at the European Space Agency's European Space Research and Technology Center (ESA-ESTEC, Noordwijk, Netherlands) and the final L2 Operational Processor (L2OP) will be run at the European Organisation for the Exploitation of Meteorological Satellites (EUMETSAT, Darmstadt, Germany). The bread-board algorithm and the prototype / operational algorithms are in principle the same although small differences may exist for practical reasons (e.g. implementation issues, computational performance). *This document describes the bread-board algorithm*.

Sentinel-4 Level-2 development activities are coordinated by DLR and are split up into algorithm bread-boarding activities performed by the various developer teams and headed by the Rutherford Appleton Laboratory (RAL, Didcot, UK), verification activities performed by the various verification teams and headed by the Max-Planck-Institut für Chemie (MPIC, Mainz, Germany) and processor suite activities performed by the various processor teams and headed by DLR. The purpose of the verification activities, which take place in parallel to the bread-boarding activities, is to generate synthetic S4 Level-1b (L1b) test data and to independently verify performance of the Level-2 algorithms. Results from these verification activities directly feed back into bread-board algorithm development.

This document is maintained during the development phase and lifetime of the product, and updates are foreseen when there are changes to the algorithm or data product.

1.2 Document overview

Section 2 lists applicable and reference documents within the Sentinel-4/5 project as well as electronic references. Section 3 provides an overview on terms, symbols and abbreviations. Section 4 introduces the NO_2 product, followed by the algorithm description in section 5 and the feasibility discussion in section 6. Section 7 discusses retrieval characterisation and error analysis, followed by section 8 on validation. The document ends with the conclusions in section 9 and the references.

1.3 Acknowledgements

We thank Steffen Beirle, Andreas Hilboll, Diego Loyola and Pieter Valks for the internal review of the document. We thank Jos van Geffen, Sebastian Gimeno Garcia, Johan de Haan, Ronny Lutz, Sander Slijkhuis and our colleagues at IUP Bremen for many useful discussions. Retrieval of NO_2 for Sentinel-4 as described in this document builds upon the heritage retrievals for GOME, GOME-2, SCIAMACHY, OMI and Sentinel-5 Precursor to which many people have made many valuable contributions over the years.

2 Applicable and reference documents, electronic references

2.1 Applicable documents

[AD01] Sentinel-4 Level-2 Processor Component Development – Signed Contract;
source: ESA; **ref**: 4000114101/15/NL/MP; **issue**: 1.0; **date**: 2015-07-15

[AD02] Sentinel-4 Level-2 Processor Component Development – Final Agreement Minutes;
source: DLR; **ref**: -; **issue**: 1.0; **date**: 2015-04-28

[AD03] Sentinel-4 Level-2 Processor Requirements Specification;
source: ESA; **ref**: S4.ESA.UVN.RS.0093; **issue**: 2.1; **date**: 2018-11-27

[AD04] Sentinel-4 L2 Processor Component Development – Project Management Plan;
source: DLR; **ref**: S4-L2-DLR-PMP-1004; **issue**: 2.1; **date**: 2017-05-31

[AD05] Sentinel-4 Level-2 Geophysical Algorithm Development Plan;
source: RAL; **ref**: S4-L2-RAL-GADP-2001; **issue**: 1.2; **date**: 2016-04-15

[AD06] Sentinel-4 Level-2 Geophysical Algorithm Verification Plan;
source: MPIC; **ref**: S4-L2-MPIC-GAVP-3001; **issue**: 1.2; **date**: 2016-04-15

[AD07] Sentinel-4 L2 Software Requirements Specification (SRS);
source: DLR; **ref**: S4-L2-DLR-SRS-4003; **issue**: 2.0; **date**: 2018-10-15

[AD08] Sentinel-4 L2 Input Output Data Specification (IODS);
source: DLR; **ref**: S4-L2-DLR-IODS-4004; **issue**: 2.9.0; **date**: 2023-09-29

2.2 Reference documents

[RD01] Sentinel-4 Level 2 Product User Manual (PUM) Nitrogen dioxide NO_2
source: DLR; **ref**: S4-L2-DLR-PUM-4104; **issue**: 2.9.1; **date**: 2025-08-18

[RD02] S4 L2 Terms and symbols used in the ATBDs;
source: DLR; **ref**: S4-L2-DLR-ATBD-2019; **issue**: 1.0; **date**: 2017-05-15

[RD03] GMES Sentinels 4 and 5 Mission Requirements Traceability Document;
source: ESA; **ref**: EOP-SM/2413/BV-bv; **issue**: 1.0; **date**: 2012-09-20

[RD04] Sentinel-4 Level 2 ATBD Cloud;
source: DLR; **ref**: S4-L2-DLR-ATBD-2009; **issue**: 4.1; **date**: 2025-08-18

[RD05] Sentinel-4 Level 2 ATBD Heterogeneous Scene Correction;
source: DLR; **ref**: S4-L2-DLR-ATBD-2012; **issue**: 3.6; **date**: 2023-11-30

[RD06] Sentinel-4 Surface Reflectance and AOD ATBD;
source: LOA / CAT / RAY; **ref**: S4-L2-LOA_CAT_RAY-ATBD-2010; **issue**: 4.0;
date: 2025-06-30

[RD07] Sentinel-4 Level-2 ATBD Sulphur Dioxide (SO_2);
source: BIRA; **ref**: S4-L2-BIRA-ATBD-2005; **issue**: 4.0; **date**: 2025-06-30

[RD08] Sentinel-4 Level-2 ATBD Formaldehyde (HCHO);
source: BIRA; **ref**: S4-L2-BIRA-ATBD-2006; **issue**: 4.1; **date**: 2025-08-18

[RD09] Sentinel-4 Level-2 ATBD Tropospheric Glyoxal;
source: IUP; **ref**: S4-L2-IUP-ATBD-2007; **issue**: 4.0; **date**: 2025-06-30

[RD10] Sentinel-4 Level-2 ATBD ECMWF and CAMS model data preprocessing;
source: IUP / BIRA / KNMI; **ref**: S4-L2-IUP_BIRA_KNMI-ATBD-2020; **issue**: 4.0;
date: 2025-06-30

[RD11] Sentinel-4 Instrument Design;
source: ESA; **ref**: S4-L2-ESA-TEC-2016; **issue**: 1.0; **date**: 2016-04-13

[RD12] Sentinel 4 UVN: Level 0-1b Prototype Data Processor Algorithm Theoretical Basis Document;
source: Airbus; **ref**: GS4.ASG.UVN.DS.00001; **issue**: 7.0; **date**: 2016-10-14

[RD13] TROPOMI ATBD of the total and tropospheric NO_2 data products;
source: KNMI; **ref**: S5P-KNMI-L2-0005-RP; **issue**: 2.2.0; **date**: 2021-06-16

[RD14] Sentinel-5 precursor/TROPOMI Level 2 Product User Manual Nitrogen Dioxide;
source: KNMI; **ref**: S5P-KNMI-L2-0021-MA; **issue**: 4.0.2; **date**: 2021-11-05

[RD15] S5P/TROPOMI Science Verification Report;
source: IUP; **ref**: S5P-IUP-L2-ScVR-RP; **issue**: 2.1; **date**: 2015-12-22

[RD16] Wavelength calibration in the Sentinel 5-Precursor Level 2 data processors;
source: KNMI; **ref**: S5P-KNMI-L2-0126-TN, **issue**: 1.0.0; **date**: 2015-09-11

[RD17] Sentinel 5 precursor Level 2 File Format Guidelines;
source: DLR / KNMI; **ref**: S5P-KNMI-L2CO-0005-TN; **issue**: 0.0.5; **date**: 2016-05-25

[RD18] CAMS Forecast Data Needs for Sentinel-4 and -5 Data Processing;
source: ESA; **ref**: ESA-EOPSM-S4-MEM-3412; **issue**: 0.6; **date**: 2018-06-15

[RD19] Sentinel-4: Level 2 Needs for External Data;
source: RAL; **ref**: S4-L2-RAL-TEC-2021; **issue**: 1.0; **date**: 2017-07-20

[RD20] Impact of Spaceborne Observations on Tropospheric Composition Analysis and Forecast (ISOTROP);
source: ESA; **ref**: contract 4000105743/11/NL/AF; **issue**: …; **date**: 2017-03-10

[RD21] Sentinel-5 L2 Prototype Processors: Algorithm Theoretical Basis Document for NO_2;
source: KNMI; **ref**: KNMI-ESA-S5L2PP-ATBD-001; **issue**: 3.1 **date**: 2019-05-17

[RD22] Sentinel-4 Instrument Polarisation Sensitivity Knowledge from On-Ground Characterisation for Level-2 Impact Mitigation;
source: ESA; **ref**: [BV]; **issue**: -; **date**: 2016-05-26

2.3 Electronic references

[ER01] http://www.spec.org/cpu2006/results/cpu2006

[ER02] http://atmosphere.copernicus.eu/services/air-quality-atmospheric-composition

[ER03] https://www.ecmwf.int/en/forecasts

3 Terms, symbols and abbreviations

Terms, symbols and abbreviations that are used within the Sentinel-4 Level-2 project are described in [RD02]. Terms, symbols and abbreviations that are specific for this document can be found below.

3.1 Terms and symbols

Term	Symbol	Definition
accuracy		absence of systematic and random errors
uncertainty		presence of systematic and random errors
trueness		absence of systematic errors
bias / offset		presence of systematic errors
precision		absence of random errors
noise		presence of random errors
error		difference between measured and true value
hyperspectral imager		imager with a large number of spectral channels, often at high spectral resolution (better than about 0.5-1 nm), e.g. GOME-2, SCIAMACHY
multispectral imager		imager with a number of spectral channels (typically 30-50) that are generally not contiguous and have coarser spectral resolution (2-10 nm), e.g. MODIS
imaging spectrometer		spectrometer that images the entrance slit on a two-dimensional CCD detector having wavelength on one axis and along-slit position on the other axis, e.g. OMI
columns of the CCD		different columns correspond to different wavelengths in S4
rows of the CCD		different rows correspond to different across-track viewing directions in S4
height	z	vertical distance above some reference surface, e.g. above ground level (a.g.l.) or above mean sea level (a.s.l.)
altitude	z	vertical distance above mean sea level (geoid)
elevation	z_s	altitude of ground surface
pressure	p	
surface pressure	p_s	
'full-level' pressure	p_l	layer pressure midpoint; $l \in \{1, 2, \ldots, \mathrm{nlev}\}$; layer 1 is uppermost layer and layer nlev is lowermost layer; we have by definition $p_l = (p_{l+0.5} + p_{l-0.5})/2$
'half-level' pressure	$p_{l+0.5}$	layer interface pressure; $l \in \{0, 1, 2, \ldots, \mathrm{nlev}\}$; $p_{0.5}$ is pressure at top-of-atmosphere and $p_{nlev+0.5} = p_s$ is pressure at bottom-of-atmosphere (surface pressure)
	Δp_l	$\Delta p_l = p_{l+0.5} - p_{l-0.5}$
altitude-resolved air mass factor	$m(z)$	

box air mass factors	$\mathbf{m}$, m_l	box air mass factors (column vector), l-th element is box air mass factor for model layer l
	$\mathbf{m}^*$	temperature-corrected box air mass factors
	$\mathbf{m}^{\mathrm{trop}}$	as $\mathbf{m}$, but with stratospheric elements set to zero
	$\mathbf{m}^{\mathrm{strat}}$	as $\mathbf{m}$, but with tropospheric elements set to zero
air mass factor	M	column or total air mass factor
tropopause pressure	p_{tp}	tropopause pressure
tropopause	l_{tp}	index of uppermost layer assigned to troposphere; $p_{l_{tp}-0.5} < p_{tp} < p_{l_{tp}+0.5}$
number concentration	$n(z)$	in units of m^{-3}
(total) vertical column	N_v	in units of mol m^{-2}
partial vertical columns	$\mathbf{N_v}$, $N_{v,l}$	partial vertical columns (column vector), l-th element is partial vertical column of model layer l; note that occasionally $N_{v,i}$ refers to the total vertical column for species *i*, but this will be clear from the context
	$\mathbf{N_v^*}$	partial vertical columns corrected for model biases (i.e. the a priori profile)
	$\mathbf{N_v}^{\mathrm{trop}}$	as $\mathbf{N_v}$, but with stratospheric elements set to zero
	$\mathbf{N_v}^{\mathrm{strat}}$	as $\mathbf{N_v}$, but with tropospheric elements set to zero
(total) slant column	N_s	
partial slant columns	$\mathbf{N_s}$, $N_{s,l}$	partial slant columns (column vector), l-th element is partial slant column of model layer l; note that occasionally $N_{s,i}$ refers to the total slant column for species *i*, but this will be clear from the context
temperature profile	$\mathbf{T}$, T_l	temperature profile (column vector); l-th element is temperature of model layer l
temperature correction factor	$\mathbf{c^T}$, c_l^T	(possible confusion with matrix transpose, should be clear from context)
model profile		profile forecasts from CAMS, interfaced through the ECA engineering product
a priori profile	$\mathbf{N_v^*}$, $N_{v,l}^*$	bias-corrected model profile
	λ	monochromatic wavelength
	λ_i	central wavelength of spectral channel i
	$I(\lambda)$	monochromatic radiance (intensity)
	$\tilde{I}(\lambda_i)$	measured radiance (i.e. convolution with ISRF implied)
reflectance	R	$\pi I / \mu_0 E_0$ (top-of-atmosphere reflectance)
sun-normalized radiance	I_n	I / E_0

processing flag		A processing flag is understood to be binary; a technical processing flag is raised in case of processing errors (failures) or processing warnings.
Bidirectional Reflectance Factor (matrix)	$\boldsymbol{\rho_s}$	describes the ground surface; the intensity reflected is $\mathbf{I}^+(\mu,\varphi) = \frac{1}{\pi}\int_0^{2\pi}\int_0^1 \boldsymbol{\rho_s}(\mu,\varphi;\mu',\varphi')\cdot\mathbf{I}^-(-\mu',\varphi')\mu' d\mu' d\varphi'$
	ρ_s	(1,1)-element of the BRF matrix
	$\boldsymbol{\rho}$	vector of BRF model coefficients; $\boldsymbol{\rho}$ = (k, k_{vol}, k_{geo}) over land and $\boldsymbol{\rho}$ = (σ, δ_{Fr}, a_0) over water
BRF and BRDF		A surface's BRF is the BRDF of that surface divided by the BRDF of an ideal (lossless) Lambertian surface.
(hemispherical) flux	F	$F^+(\lambda) = \int_0^{2\pi}\int_0^1 I^+(\mu',\varphi';\lambda)\mu' d\mu' d\varphi'$ (upward) $F^-(\lambda) = \int_0^{2\pi}\int_0^1 I^-(-\mu',\varphi';\lambda)\mu' d\mu' d\varphi'$ (downward)
surface albedo	A_s	The surface albedo is the ratio of reflected flux to incident flux. It generally depends on the BRF of the surface *and* on the incident radiance field $I^-(-\mu',\varphi')$. We have $A_s(\lambda) = \frac{F^+(\lambda)}{F^-(\lambda)} = \frac{\frac{1}{\pi}\int_0^{2\pi}\int_0^1\int_0^{2\pi}\int_0^1 \rho_s(\mu,\varphi;\mu',\varphi';\lambda)I^-(-\mu',\varphi';\lambda)\mu' d\mu' d\varphi'\mu d\mu d\varphi}{\int_0^{2\pi}\int_0^1 I^-(-\mu',\varphi';\lambda)\mu' d\mu' d\varphi'}$.
spherical albedo	A_{spher}	The spherical albedo is a special case of the surface albedo for an isotropic incident radiance field (I^- is constant). We have $A_{spher}(\lambda) = \frac{1}{\pi^2}\int_0^{2\pi}\int_0^1\int_0^{2\pi}\int_0^1 \rho_s(\mu,\varphi;\mu',\varphi';\lambda)\mu' d\mu' d\varphi'\mu d\mu d\varphi$. The spherical albedo is also called the bi-hemispherical reflectance for isotropic illumination or white-sky albedo.
Lambertian albedo	A_{Lamb}	The albedo of a Lambertian surface, or Lambertian albedo for short, is a special case of the surface albedo for a surface with constant BRF, $\rho_s(\mu,\varphi;\mu',\varphi';\lambda) = \rho_s(\lambda)$. We have $A_{Lamb}(\lambda) = \rho_s(\lambda)$.
	$(\mu,\varphi;\mu',\varphi')$	function argument describing angles; order of angles is always (outgoing angles; incoming angles)
reflectance matrix	$\mathbf{R}(\mu,\varphi;\mu',\varphi')$	describes the atmosphere; the atmospheric reflectance for illumination from above is defined by $\mathbf{I}^+(\mu,\varphi) = \frac{1}{\pi}\int_0^{2\pi}\int_0^1 \mathbf{R}(\mu,\varphi;\mu',\varphi')\cdot\mathbf{I}^-(-\mu',\varphi')\mu' d\mu' d\varphi'$
transmittance matrix	$\mathbf{T}(\mu,\varphi;\mu',\varphi')$	describes the atmosphere; the atmospheric transmittance for illumination from above is defined by $\mathbf{I}^-(-\mu,\varphi) = \frac{1}{\pi}\int_0^{2\pi}\int_0^1 \mathbf{T}(\mu,\varphi;\mu',\varphi')\cdot\mathbf{I}^-(-\mu',\varphi')\mu' d\mu' d\varphi'$
	$\mathbf{R}^*(\mu,\varphi;\mu',\varphi')$	the atmospheric reflectance for illumination from below is defined by $\mathbf{I}^-(-\mu,\varphi) = \frac{1}{\pi}\int_0^{2\pi}\int_0^1 \mathbf{R}^*(\mu,\varphi;\mu',\varphi')\cdot\mathbf{I}^+(\mu',\varphi')\mu' d\mu' d\varphi'$

	$\mathbf{T}^*(\mu,\varphi;\mu',\varphi')$	the atmospheric transmittance for illumination from below is defined by $\mathbf{I}^+(\mu,\varphi)=\frac{1}{\pi}\int_0^{2\pi}\int_0^1 \mathbf{T}^*(\mu,\varphi;\mu',\varphi')\cdot\mathbf{I}^+(\mu',\varphi')\mu' d\mu' d\varphi'$
	$\mathbf{R}(2\pi;\mu',\varphi')$	$(2\pi;\mu',\varphi')$ implies integration over hemisphere (μ,φ) as in $\mathbf{R}(2\pi;\mu',\varphi')=\frac{1}{\pi}\int_0^{2\pi}\int_0^1 \mathbf{R}(\mu,\varphi;\mu',\varphi')\mu d\mu d\varphi$
	$\mathbf{R}(\mu,\varphi;2\pi)$	$(\mu,\varphi;2\pi)$ implies integration over hemisphere (μ',φ') as in $\mathbf{R}(\mu,\varphi;2\pi)=\frac{1}{\pi}\int_0^{2\pi}\int_0^1 \mathbf{R}(\mu,\varphi;\mu',\varphi')\mu' d\mu' d\varphi'$
	k_{abs}	aerosol volume absorption coefficient
	k_{sca}	aerosol volume scattering coefficient
	k_{ext}	aerosol volume extinction coefficient
latitude	δ_{geo}	
longitude	ϑ_{geo}	

3.2 Abbreviations

Abbreviation	Meaning
a.g.l.	above ground level
AMF	Air Mass Factor
AOT	Aerosol Optical Thickness
a.s.l.	above sea level
ATBD	Algorithm Theoretical Basis Document
AVK	Averaging Kernel
BAMF	Box Air Mass Factor
BHR	Bi-Hemispherical Reflectance
BOA	Bottom-of-atmosphere
BRDF	Bidirectional Reflectance Distribution Function
BRF	Bidirectional Reflectance Factor
CALIOP	Cloud-Aerosol Lidar with Orthogonal Polarization
CAMS	Copernicus Atmosphere Monitoring Service
CCD	Charge-Coupled Device
CTM	Chemical Transport Model
DLR	Deutsches Zentrum für Luft- und Raumfahrt (Oberpfaffenhofen, Germany)
DOAS	Differential Optical Absorption Spectroscopy
ECA	ECMWF-CAMS
ECMWF	European Centre for Medium-Range Weather Forecasts
ESA	European Space Agency
ESTEC	European Space Research and Technology Center (Noordwijk, Netherlands)
EUMETSAT	European Organisation for the Exploitation of Meteorological Satellites (Darmstadt, Germany)
FWHM	Full Width at Half Maximum
GEMS	Geostationary Environment Monitoring Spectrometer
GEO	Geostationary Orbit
GOME	Global Ozone Monitoring Experiment
GSR	Gapless Surface Reflectance (an S4 L2 support product)
HSC	Heterogeneous Scene Correction (an S4 L2 support algorithm)

Abbreviation	Meaning
IUP Bremen	Institut für Umweltphysik (Bremen, Germany)
ISRF	Instrument Spectral Response Function
KNMI	Koninklijk Nederlands Meteorologisch Instituut (De Bilt, Netherlands)
L0	Level-0
L1	Level-1
L2	Level-2
L2OP	Level-2 Operational Processor
L2PP	Level-2 Prototype Processor
LEO	Low Earth Orbit
LER	Lambertian-Equivalent Reflectivity
LUT	Look-up table
MAX-DOAS	Multi-AXis DOAS
MODIS	Moderate Resolution Imaging Spectroradiometer
MPIC	Max-Planck-Institut für Chemie (Mainz, Germany)
MTG-S	Meteosat Third Generation Sounder
NDACC	Network for the Detection of Atmospheric Composition Change
NIR	Near-infrared
NRT	Near real-time
NWP	Numerical Weather Prediction
OCRA	Optical Cloud Recognition Algorithm
OMI	Ozone Monitoring Instrument
PMD	Polarisation Measuring Devices
POLDER	Polarization and Directionality of the Earth's Reflectances
PUM	Product User Manual
QA	Quality Assurance
QA4ECV	Quality Assurance for Essential Climate Variables
RAA	Relative Azimuth Angle
RAL	Rutherford Appleton Laboratory (Didcot, UK)
ROCINN	Retrieval of Cloud Information using Neural Networks
S4	Sentinel-4
S5	Sentinel-5
S5P	Sentinel-5 Precursor
SCD	Slant Column Density
SCIAMACHY	Scanning Imaging Spectrometer for Atmospheric Cartography
SRR	System Requirement Review
SSD	Spatial Sampling Distance
SSI	Spectral Sampling Interval
SUR	Surface Reflectance and AOD (an S4 L2 core product)
SZA	Solar Zenith Angle
TEMPO	Tropospheric Emissions: Monitoring of Pollution
TM5	Transport Model 5 (a CTM)
TOA	Top-of-atmosphere
TP	Tropopause
TROPOMI	Tropospheric Monitoring Instrument
UV	Ultraviolet
UVis	Ultraviolet and visible
UVN	Ultraviolet, visible and near-infrared
VCD	Vertical Column Density
Vis	Visible
VZA	Viewing Zenith Angle

Abbreviation	Meaning
WMO	World Meteorological Organization

4 Introduction to the Sentinel-4 NO_2 product

4.1 Sentinel-4 UVN

A separate document describes the Sentinel-4 mission and the satellite instrument in detail ([RD11]). Here we briefly summarize the main aspects, focusing on those points that are important for understanding the present document.

Sentinel-4 is an operational satellite mission providing atmospheric composition data for the European region with a fast, hourly revisit time in support of the Copernicus Atmosphere Monitoring Service (CAMS). The S4 instrument is an Ultraviolet Visible Near-infrared (UVN) spectrometer that will be carried on the geostationary Meteosat Third Generation Sounder (MTG-S) platforms. The satellites' nominal longitude is 0°. The first MTG-S platform is expected to be put into orbit around 2021 and the second platform around 2029.

The instrument measurement concept combines a scan mirror with a push-broom design. A mirror scanning slowly from east to west captures the light from a narrow strip on the Earth running in the north-to-south direction and reflects it into the telescope. The telescope system in turn images the strip onto the slits of the ultraviolet and visible (UVis) and near-infrared (NIR) spectrometer channels. The across-slit dimension is collapsed into a spectral dimension and spectra are recorded by two-dimensional Charge-Coupled Device (CCD) detectors. The UVN instrument covers the visible wavelength range with a spectral resolution of about 0.5 nm at a sampling ratio of three.

Inhomogeneities in the radiance distribution across the slit may cause small changes to the instrument's nominal spectral response function. A dedicated S4 L2 support product addresses this issue and the S4 NO_2 algorithm optionally uses parameters provided by this support product. Furthermore, because the UVis and the NIR light are treated by two different spectrometer systems, there may be slight mismatches or co-registration errors between ground pixels for the two wavelength bands (in both across-track and along-track directions). These mismatches have to be corrected when information from the two channels is combined. In case of S4 NO_2, this mainly concerns the use of cloud parameters retrieved from the O_2 A band.

The spatial sampling distance varies across the geographic coverage area due to projection and curvature effects and is about 8 x 8 km at a reference location at 45° N and the satellite's nominal longitude. There are 551 pixels in the north-to-south direction and about 580 pixels in a single east-to-west scan. A daily Earth observation will consist of about 16 to 20 one-hour east-to-west scans with fast retraces in-between. The total area covered in a single day by Sentinel-4 is the European extended region. The area captured by a single one-hour scan is smaller and varies within the geographic coverage area in a systematic way depending on the time of day and season. Most importantly for S4 NO_2, there is a large westward shift in the afternoon bringing the unpolluted North Atlantic region into the field of view only for the second half of the day. Typical viewing zenith angles and solar zenith angles for S4 are illustrated in Figure 4.1 and Figure 4.2, respectively.

S4 will be the first mission carrying a UVN imaging spectrometer in a geostationary orbit over Europe. Other, similar spectrometers are the Tropospheric Emissions: Monitoring of Pollution (TEMPO) mission (Zoogman et al., 2016), which covers the North American extended region, and the Geostationary Environment Monitoring Spectrometer (GEMS; Kim, 2012), which covers the East Asian extended region. A clear synergy between geostationary observations and observations by similar spectrometers in polar orbits is expected. The latter typically have global coverage daily but observe a particular location only once a day, at least at low and mid latitudes. For S4 NO_2, it is planned to use data from the polar-orbiting Sentinel-5 Precursor (S5P) and Sentinel-5 (S5) instruments, whose global observations of stratospheric NO_2 will be used to validate the stratospheric correction step in the S4 tropospheric NO_2 retrieval.

Throughout this document we refer to the Sentinel-4 satellite instrument as S4 or as UVN interchangeably. Furthermore, we call the east-to-west scanning direction the along-track or across-slit direction and the north-to-south direction the across-track or along-slit direction. Finally, we adopt the project convention that rows of the two-dimensional CCD correspond to the different viewing directions (the across-track dimension of the CCD) and columns to the different wavelengths (the spectral dimension of the CCD).

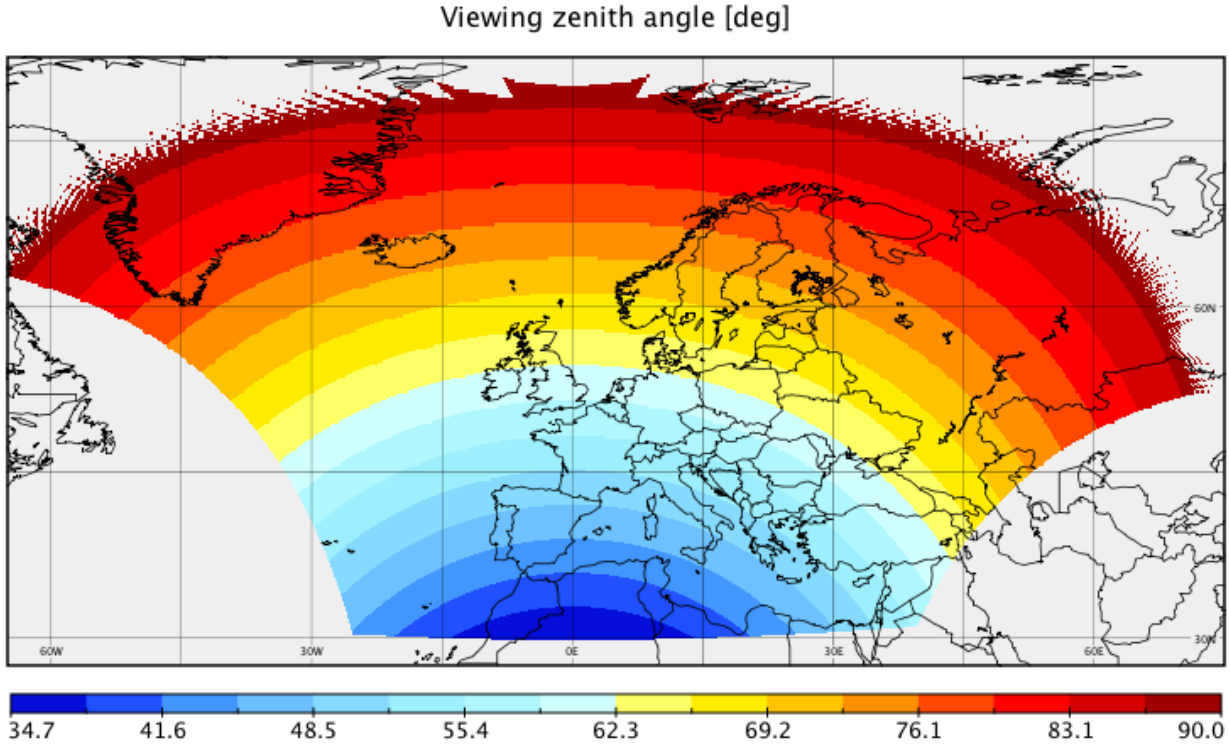

Figure 4.1. Viewing zenith angle at sea level across S4's entire geographic coverage area. Here, the satellite is positioned at 0° longitude and 0° latitude. The position of the satellite will vary slightly while in orbit with a north-to-south amplitude of about 2° and an east-to-west amplitude of about 0.5°. At the eastern and western edges of the geographic coverage area only about half of the CCD rows correspond to line-of-sights that actually hit the Earth's surface. The area covered by a single one-hour scan is smaller than the geographic coverage area and varies in a systematic way. Most significant is a large westward shift in the afternoon, see also in this respect Figure 7.3.

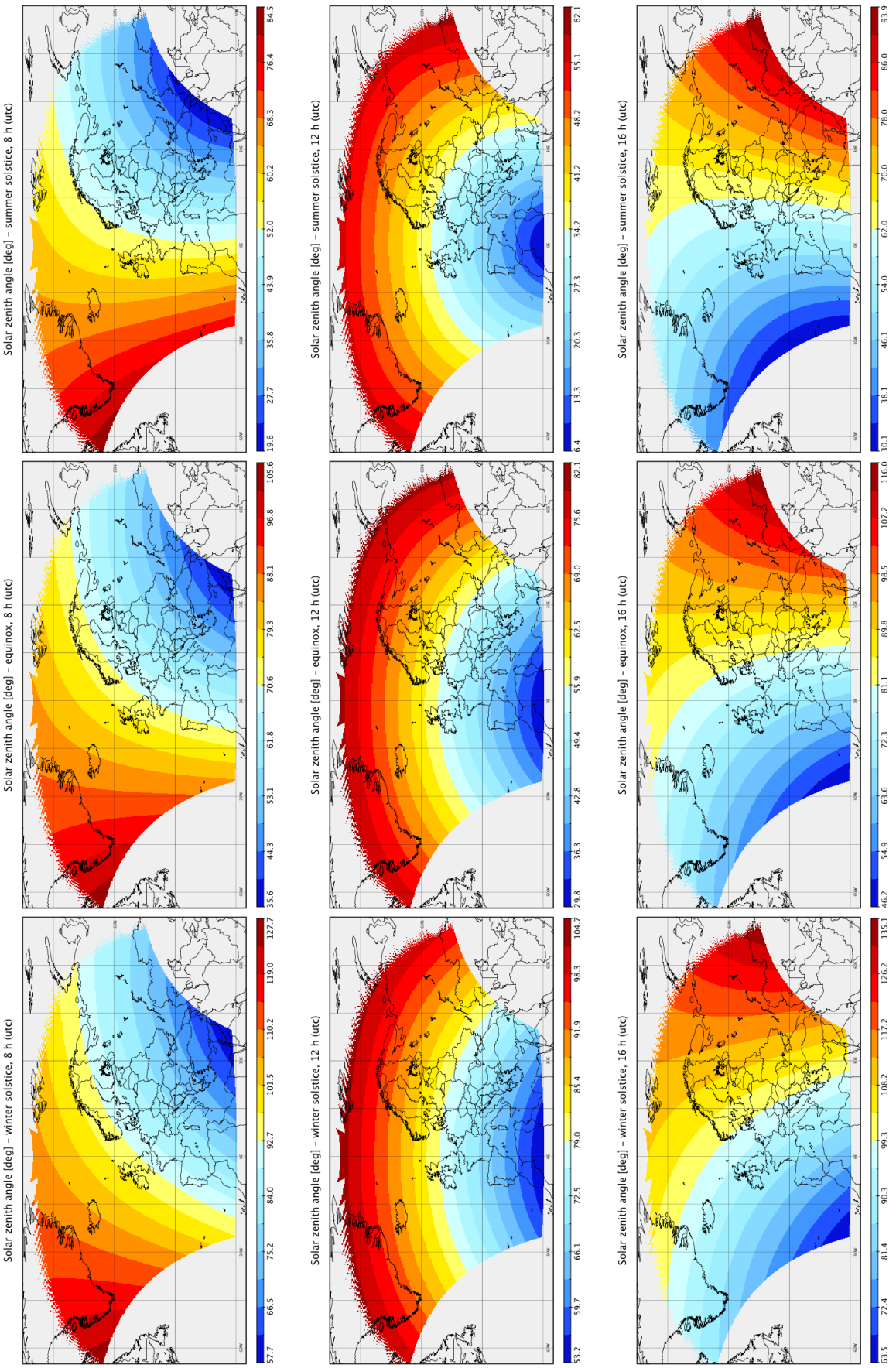
Solar zenith angle [deg] – summer solstice, 8 h (utc)
19.6 27.7 35.8 43.9 52.0 60.2 68.3 76.4 84.5
Solar zenith angle [deg] – equinox, 8 h (utc)
35.6 44.3 53.1 61.8 70.6 79.3 88.1 96.8 105.6
Solar zenith angle [deg] – winter solstice, 8 h (utc)
57.7 66.5 75.2 84.0 92.7 101.5 110.2 119.0 127.7
Solar zenith angle [deg] – summer solstice, 12 h (utc)
6.4 13.3 20.3 27.3 34.2 41.2 48.2 55.1 62.1
Solar zenith angle [deg] – equinox, 12 h (utc)
29.8 36.3 42.8 49.4 55.9 62.5 69.0 75.6 82.1
Solar zenith angle [deg] – winter solstice, 12 h (utc)
53.2 59.7 66.1 72.5 79.0 85.4 91.9 98.3 104.7
Solar zenith angle [deg] – summer solstice, 16 h (utc)
30.1 38.1 46.1 54.0 62.0 70.0 78.0 86.0 93.9
Solar zenith angle [deg] – equinox, 16 h (utc)
46.2 54.9 63.6 72.3 81.1 89.8 98.5 107.2 116.0
Solar zenith angle [deg] – winter solstice, 16 h (utc)
63.5 72.4 81.4 90.3 99.3 108.2 117.2 126.2 135.1

Figure 4.2 (previous page). Solar zenith angle at sea level across S4's geographic coverage area. Depicted UTC times are 8 h, 12 h and 16 h (rows) for winter solstice, equinox and summer solstice (columns). Note that the range of each colour bar extends from the minimum to the maximum value for that map and is therefore different in every panel. Furthermore, solar zenith angles in these maps can be larger than 90°: only pixels with viewing zenith angles larger than 90° have been masked, as in Figure 4.1.

4.2 Product description

Nitrogen oxides (NO_x = NO + NO_2) play important roles in many aspects of atmospheric chemistry. In the stratosphere, they act as ozone depleting catalysts but they also form reservoir substances for chlorine and bromine, which in turn limits ozone depletion. In the troposphere, they are one of the key ingredients for the formation of ozone and they increase aerosol concentrations through nitrate formation. NO_2 is an air pollutant itself as well with adverse effects on human health. In addition, deposition of nitrogen leads to acidification and eutrophication of water bodies. While the warming potential of NO_2 is relevant only locally in highly polluted regions, nitrogen oxides have indirect climate effects via the formation of O_3, their impact on OH and thus CH_4 lifetime, and through aerosol formation. NO_2 concentrations in the stratosphere are mainly driven by photochemistry and are characterised by a clear diurnal cycle with rapid photolysis of NO_2 at dawn and rapid reformation at dusk. In contrast, NO_2 amounts in the troposphere are primarily governed by local emissions as result of the short lifetime of NO_2 (a few hours) with transport playing a secondary role. Figure 4.3 shows a typical vertical distribution of background NO_2 and one can see that tropospheric and stratospheric NO_2 are quite well separated.

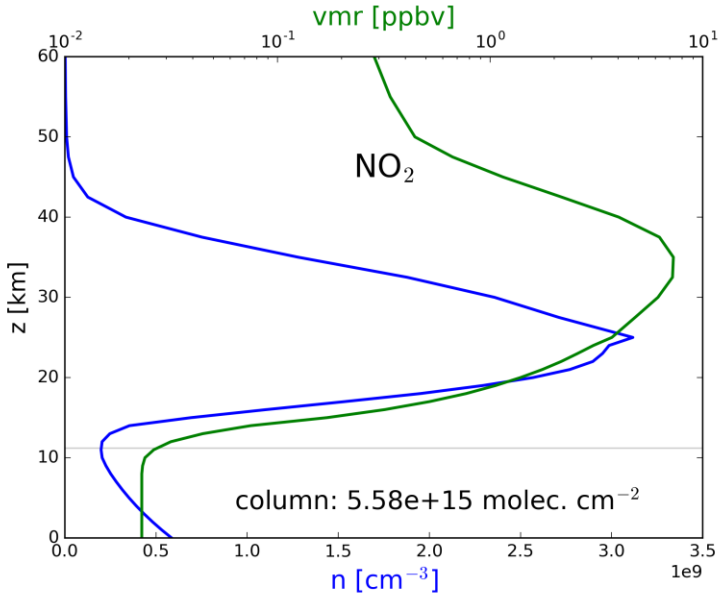

Figure 4.3. The NO_2 profile in the US Standard Atmosphere. The tropopause according to the temperature gradient criterion is at 11 km (thin grey line). In polluted regions, surface concentrations can be much higher causing the tropospheric column to dominate the total column.

In the context of S4, particularly the tropospheric NO_2 is of interest. In most parts of Europe, anthropogenic sources from fossil fuel combustion and occasional biomass burning dominate over natural emissions from soils and lightning. In many urban areas, NO_2 levels at the surface exceed EU air quality thresholds, creating the need for monitoring of NO_2 levels as well as driving measures to reduce NO_x emissions. By using sophisticated inversion schemes, spatially resolved emission maps of NO_x can be determined from satellite data. Thus, satellite data can provide the spatial distribution of tropospheric NO_2 amounts, their change over time, and estimates of the emissions. As an illustration, Figure 4.4 shows average tropospheric NO_2 columns over Europe from the Ozone Monitoring Instrument (OMI) for the summer of 2015. Areas with high pollution levels as well as pollution outflows can be seen.

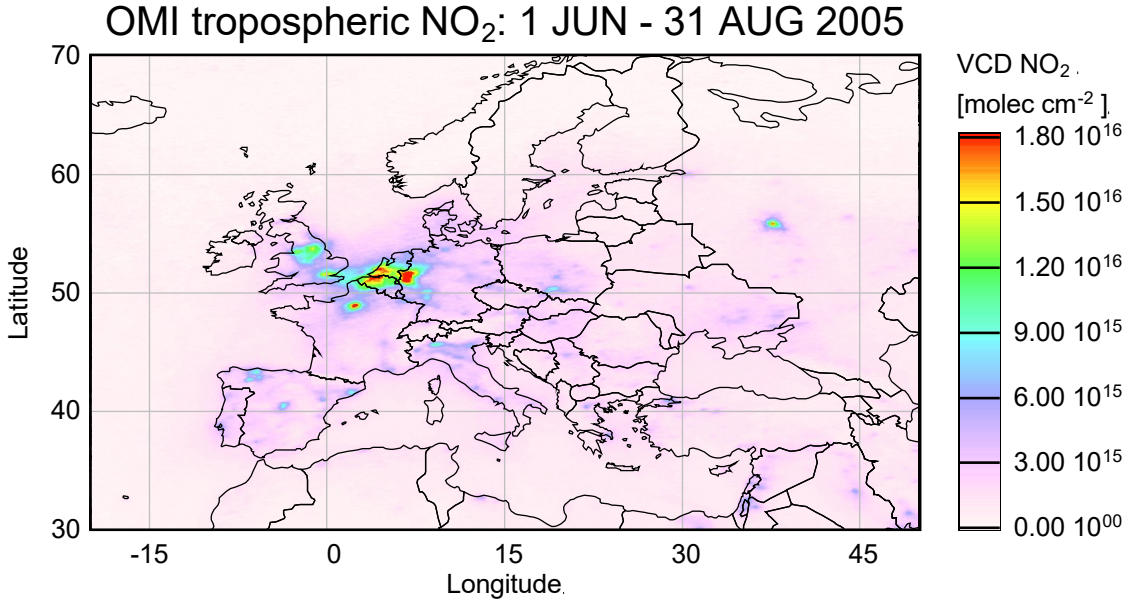

Figure 4.4. OMI tropospheric NO_2 columns from IUP Bremen over Europe in summer of 2015.

Measurements from S4 will improve on the existing satellite data sets mainly in two aspects: by their good spatial resolution and by the hourly instead of daily revisit time. This combination is expected to improve the spatial detail of the retrieved fields, to reduce the number of days where clouds prevent measurements, and most importantly to enable – for the first time – the observation of the diurnal evolution of the NO_2 burden and thereby NO_x emission strengths over Europe from space. The primary applications of the S4 NO_2 product will thus be pollution monitoring and emission estimation, and the main output field of the data product will be tropospheric NO_2 column amounts. The data are processed in granules of five minutes and the operational NO_2 product is delivered in near real-time. This means that Level-2 files become available for end-users within about one hour after sensing.

The use of NO_2 observations from Sentinel-4 with their high temporal sampling also has the potential to be a significant innovation for the data assimilation systems of the Copernicus Atmosphere Monitoring Service. This could for example be in the form of tropospheric columns with averaging kernels representing the (limited) number of degrees of freedom. The fast chemical conversions between NO_2 and NO make data assimilation of NO_2 from polar orbiting satellites far from trivial; having a much better constraint on the diurnal cycle should improve this situation, both for the global and regional data assimilation and forecasting systems. The much higher temporal sampling will also support the estimation of emissions, in independent systems as well as potentially in the data assimilation systems themselves. With the deployment of similar geostationary satellite instruments by other agencies, there is significant potential to improve the chemical data assimilation globally.

The retrieval of NO_2 column amounts is based on absorption by NO_2 in the visible wavelength range. The S4 NO_2 baseline fit window extends from 425 to 497 nm. A meanwhile established retrieval scheme is applied in which quantification from Earth radiance measurements of the absorption by NO_2 along photon paths in the atmosphere is separated from the actual calculation of this photon path distribution (the radiative transfer problem). In an intermediate step, total column amounts are split into a tropospheric and a stratospheric part. In addition to tropospheric NO_2 column amounts, the S4 NO_2 product will also contain total and stratospheric column amounts, estimates of their uncertainties, column averaging kernels, quality assurance parameters and other information that increases the usability of the data product.

Table 4.1 gives an overview of the main user applications of the NO_2 product and the corresponding data fields of interest. The product user manual ([RD01]) provides further examples and explanations of how the NO_2 product can and should be appropriately used.

Table 4.1. Main user applications of the NO_2 product and the corresponding data fields of interest. See also Section 0 for an explanation and a list of all user flags.

User application	**NO_2 product data fields**
Air quality assessments / scientific investigations of geophysical phenomena (emission estimates, correlational analyses, trend analyses, etc.).	nitrogendioxide_tropospheric_column nitrogendioxide_tropospheric_column_precision *User flags:* tropospheric_column_nominal pixel_sufficiently_clear
Tropospheric chemistry / air quality model evaluation and data assimilation. Validation with tropospheric NO_2 profile measurements.	nitrogendioxide_tropospheric_column nitrogendioxide_tropospheric_column_precision_kernel nitrogendioxide_total_column_averaging_kernel nitrogendioxide_total_column_air_mass_factor nitrogendioxide_tropospheric_column_air_mass_factor tropopause_layer_index_uvvis
Whole atmosphere (troposphere and stratosphere) data assimilation.	nitrogendioxide_doas_total_column nitrogendioxide_doas_total_column_precision_kernel nitrogendioxide_total_column_averaging_kernel
Tropospheric and total column comparisons with other satellites.	nitrogendioxide_tropospheric_column nitrogendioxide_tropospheric_column_precision nitrogendioxide_summed_total_column nitrogendioxide_summed_total_column_precision *User flags:* tropospheric_column_nominal pixel_sufficiently_clear air_mass_factors_nominal stratospheric_slant_column_nominal

4.3 Heritage

The S4 NO_2 retrieval algorithm is based on a long-standing heritage of NO_2 retrievals from a family of polar orbiting satellite spectrometers. Various NO_2 retrieval schemes have been developed over the years by independent groups for the Global Ozone Monitoring Experiment (GOME; e.g. Leue et al., 2001, Richter and Burrows, 2000, 2002, Martin et al., 2002, Boersma et al., 2004), Scanning Imaging Spectrometer for Atmospheric Cartography (SCIAMACHY; Richter et al., 2004), OMI (Boersma et al., 2011, Bucsela et al., 2013), GOME-2 (Valks et al., 2011, Richter et al., 2011) and S5P ([RD13]). All retrieval schemes share a common approach that is based on the following three steps.

1. The spectral retrieval of NO_2 slant columns (i.e. the concentration of NO_2 integrated along photon paths in the atmosphere) using the Differential Optical Absorption Spectroscopy (DOAS) technique (Platt and Stutz, 2008; Richter and Wagner, 2011). The generic assumption is that absorption by NO_2 is weak, which is valid in most situations and allows for various simplifications.
2. The separation of slant columns into a stratospheric and tropospheric part. A number of methods with different levels of complexity have been developed over the years. These methods all rely, in one way or another, on the observation that stratospheric and tropospheric NO_2 are well separated in the atmosphere (see Figure 4.3), and stratospheric NO_2 fields vary smoothly in space and time while in unpolluted regions tropospheric NO_2 is absent.
3. A conversion of tropospheric slant columns to tropospheric vertical columns using so-called air mass factors (AMF). Air mass factors are computed using radiative transfer models and depend on wavelength, observation geometry, surface height, surface reflectance, the expected NO_2 profile shape and sometimes also aerosol and cloud parameters. In this step, the temperature dependence of the NO_2 cross-section is often treated as well.

The specific NO_2 retrieval algorithm that will be used for S4 originates from IUP Bremen and is based on the retrievals first developed for GOME (Richter and Burrows, 2002, Richter et al., 2005) and later applied to the SCIAMACHY (Richter et al., 2004), GOME-2 (Richter et al., 2011) and OMI data sets. The IUP Bremen algorithm has served as one of the pre-launch verification algorithms for the operational S5P NO_2 algorithm ([RD15]) and is being further developed for application to real S5P spectra. We will now summarize the main characteristics of the heritage IUP Bremen NO_2 retrieval scheme.

The spectral fit is performed on the logarithm of the sun-normalized radiance. Small differences between the implementations for the various satellite instruments exist, which are mainly related to the fit window, the degree of the background polynomial and the absorption cross-sections used in the fit. For example, the baseline fit window for GOME and SCIAMACHY runs from 425 to 450 nm and the degree of the polynomial is typically three or four. The baseline fit window for GOME-2 was extended and runs from 425 to 497 nm, the degree of the polynomial being increased accordingly to five or six. The longer fit window proved to reduce the noise error. OMI slant columns are available for the same fit window and background polynomial as for GOME-2. Other differences are due to the specifics of the instrument design, such as corrections for spectral undersampling by GOME or corrections for spectral signatures of polarisation sensitivity in GOME and SCIAMACHY measurements. For OMI, fitted slant columns are post-processed to remove so-called stripe offsets that are related to the use of a two-dimensional CCD detector.

For the separation of slant columns into a stratospheric and tropospheric part, two approaches are currently implemented simultaneously at IUP Bremen for all of the satellite instruments mentioned above. In the reference sector approach, clean remote regions covering all latitudes are identified and retrieved columns for these regions, which can be assumed to be almost completely due to stratospheric NO_2, are extrapolated to a global field (Richter and Burrows, 2002; Martin et al., 2002). This approach is possible for instruments in a sun-synchronous orbit, as stratospheric NO_2 is mainly driven by photochemistry. However, it does not account for longitudinal variations in the stratospheric field. In the model stratosphere approach, stratospheric NO_2 fields are provided by a free-running dedicated stratospheric chemical transport model (CTM) (Richter et al., 2005). An offset correction is needed and calculated from the differences in measured and modelled columns over again clean remote regions. We remark that for SCIAMACHY, a third approach was implemented based on limb measurements (Beirle et al., 2010; Hilboll et al., 2013b). Here, stratospheric NO_2 fields are determined from the vertical NO_2 profiles retrieved from limb spectra of the same instrument (which cover the same area but have a coarser spatial resolution) with an offset correction calculated from the differences in retrieved columns between the limb and nadir measurement for unpolluted regions.

Finally, look-up tables of box air mass factors are calculated with the in-house radiative transfer model SCIATRAN (Rozanov et al., 2014). SCIATRAN is an extensive code package that has been intensively used over the years inside and outside IUP Bremen to solve a wide range of radiative transfer problems. In earlier IUP retrievals, tropospheric air mass factors were calculated from box air mass factors assuming a static NO_2 profile shape that was based on vertical distributions calculated by a CTM for a certain reference year in the past and subsequently averaged per month. In more recent retrievals, daily model profiles are used as a priori profiles for the air mass factor calculations. Surface reflection is described using Lambertian-equivalent reflectivity (LER) values from, for example, the GOME LER climatology. Previously, tropospheric columns were calculated only for pixels that had passed strict cloud filtering criteria and these pixels were then assumed to be entirely cloud-free. Aerosols used to be taken into account but in a simplified way where air mass factors were calculated for three different aerosol profiles and one of the three was chosen based on the pixel's geolocation. In the latest look-up tables, aerosols are not anymore considered explicitly. However, cloud corrections are applied to the air mass factors for pixels with moderate cloud fractions.

Data produced with the IUP Bremen NO_2 algorithm have been used in many scientific publications covering different aspects of NO_2 in the atmosphere, including trends (Richter et al., 2005, Hilboll et al., 2013a), shipping emissions (Richter et al., 2004, Franke et al., 2009, Richter et al., 2011), power plant emissions (Kim et al., 2006), soil emissions (Bertram et al., 2005), biomass burning (Schreier et al., 2014) and transport events (Zien et al., 2014).

As mentioned above, three stratospheric correction schemes are currently available in the IUP Bremen NO_2 retrieval setup. For S4 NO_2, however, the baseline scheme to separate stratospheric and tropospheric contributions to the retrieved slant columns will be based on a heritage assimilation system originating from KNMI. In the data assimilation approach retrieved columns are assimilated in a CTM to update the calculated NO_2 distribution within the model (Boersma et al., 2004). In this approach, measurements over unpolluted or cloudy regions get the largest weight. The resulting analysed global stratospheric NO_2 fields are used to calculate stratospheric slant columns. The assimilation system is part of the KNMI NO_2 retrieval algorithm, which has also been applied to the GOME, SCIAMACHY, GOME-2 and OMI data sets. Furthermore, the KNMI NO_2 retrieval algorithm is the operational algorithm for S5P. The motivation for the assimilation approach is that the CTM captures the dynamics of the stratosphere well but treats stratospheric chemistry in an approximate way resulting in biases between measurement and model that can be resolved by way of assimilating measured stratospheric columns into the model. The CTM that is used for GOME, SCIAMACHY, GOME-2 and OMI is TM4, while for S5P a newer version, TM5, is used. TM5 is actively developed by KNMI together with other partners in the TM5 consortium and this CTM will remain to be used in the S5P NO_2 processor during the operational lifetime of the instrument.

Data produced with the KNMI NO_2 algorithm (Boersma et al., 2011), using the assimilation approach for the stratospheric correction, have been used in many scientific publications, including the evaluation of models to reproduce atmospheric chemistry (e.g. Huijnen et al., 2010), the use of the observations in data assimilation or inverse modelling (e.g. Miyazaki et al., 2014) or identification of new emerging sources (e.g. Zhang et al., 2009).

Since there is a clear heritage, the general code framework and many of the code modules in the S4 NO_2 bread-board algorithm are adaptations of existing code that has been thoroughly tested and used at IUP Bremen and KNMI over the years. The algorithm settings reflect the latest insights into retrieval of NO_2 from the visible part of the spectrum. They benefit from recent developments made in the frameworks of the DLR funded S5P verification project at IUP Bremen and the European Union funded Quality Assurance for Essential Climate Variables (QA4ECV) project. Improvements and further developments of the S4 NO_2 retrieval algorithm are related to the specific challenges posed by S4, which are further discussed below.

4.4 Product requirements

As outlined above, tropospheric NO_2 columns are used in many applications, from air quality assessments to emission estimates and atmospheric chemistry studies. Each of these applications has its own required maximum uncertainty. In addition, satellite data often cannot directly provide the type of information that would ideally be needed (e.g. NO_2 mixing ratios at two meter above the ground in a street canyon) and subsequent analysis steps with further assumptions introducing additional uncertainties are needed. This makes formulating general product requirements somewhat problematic.

Requirements on the total uncertainty in tropospheric NO_2 column amounts from the S4 instrument are defined in [AD03]:

L2-GEO-NO2-10 → The uncertainty in the NO_2 tropospheric column density shall be smaller than $1.5 \cdot 10^{15}$ molec. cm^{-2} (threshold / goal) or 50% (threshold) to 30% (goal). Depending on the scenario, the least stringent of the absolute and the relative requirements applies.

L2-GEO-NO2-20 → The uncertainty requirement formulated in L2-GEO-NO2-10 shall be applicable for sun zenith angles up to 60°, viewing zenith angle up to 60°, and cloud fraction up to 20%.

L2-GEO-NO2-30 → The absolute uncertainty goal requirement formulated in L2-GEO-NO2-10 shall apply to NO_2 tropospheric column density smaller than $5 \cdot 10^{15}$ molec. cm^{-2}.

L2-GEO-NO2-40 → The relative uncertainty goal requirement formulated in L2-GEO-NO2-10 shall apply to NO_2 tropospheric column density larger than $5 \cdot 10^{15}$ molec.

The main drivers for uncertainty in the tropospheric NO_2 product are (i) the signal-to-noise ratio of the radiance and irradiance measurements for the absolute uncertainty of the slant columns, (ii) the trueness of the stratospheric correction for the absolute uncertainty of the tropospheric slant columns and (iii) the trueness of the assumptions made in the air mass factor calculations for the relative uncertainty of the tropospheric vertical columns. As the signal-to-noise of the spectra cannot be changed by the NO_2 algorithm and the actual DOAS fit and radiative transfer calculations have been shown to have very small uncertainties, the main challenges for the S4 NO_2 retrieval algorithm are to control the trueness of the stratospheric correction and to make appropriate choices for the parameters used in the AMF computation (including a priori profiles).

4.5 Overview of the retrieval method

The S4 NO_2 retrieval setup is described in detail in Section 5. A retrieval of NO_2 columns is attempted for all pixels with processing flags indicating situations with increased uncertainty. The baseline retrieval can be summarized as follows.

1. First, the spectral calibration of the solar irradiance measurement in the NO_2 fit window is optimised using the external Fraunhofer atlas by Chance and Kurucz (2010). The calibrated wavelength grid of the irradiance spectrum is the grid on which the spectral fit of the next step is performed.
2. Second, the NO_2 slant column is retrieved from a spectral fit of the logarithm of the ratio between radiance and irradiance measurement. Spectral calibration of the radiance measurement and interpolation to the irradiance wavelength grid is done as part of the fit, either using a non-linear optimisation or the linearized radiance wavelength calibration method of Beirle et al. (2013). Removal of spectral outliers is also included in the fit. Apart from NO_2, the fit includes absorption cross-sections of the interfering trace gases O_3, O_4, and H_2O_{vap}, the absorption coefficient of H_2O_{liq}, and cross-sections of pseudo-absorbers related to rotational Raman scattering, stray light and the linearized radiance wavelength calibration. The fit window runs from 425 to 497 nm and the degree of the background polynomial is 4. In the baseline setup, nominal S4 Instrument Spectral Response Functions (ISRFs) are used for convolution of the absorption cross-sections.
3. Third, a de-striping of fitted slant columns is applied. Correction offsets are calculated from an analysis of slant columns retrieved over clean regions in combination with model stratospheric NO_2 fields. This step may be switched off in the processor if it turns out to be unnecessary for S4.
4. Fourth, tropospheric slant columns are determined from total slant columns by subtracting the stratospheric forecast from a global model using the data assimilation approach. The baseline for the operational S4 algorithm is the CAMS global analysis system in combination with assimilation of S5(P) NO_2 columns. These stratospheric estimates are first de-biased by direct comparison with S4 observations over clean and cloudy regions.

5. The last step in the retrieval is the application of tropospheric air mass factors to determine the tropospheric vertical columns. In this step, also the uncertainty estimates and the column averaging kernels are calculated. In the operational algorithm, the baseline is to use vertical profiles for the lower troposphere from the CAMS regional model ensemble and from the CAMS global analysis system for the remaining part of the troposphere. To account for clouds, air mass factors for partly cloudy pixels are calculated as weighted averages of air mass factors for clear and cloudy atmospheres. The necessary cloud parameters are taken from the S4 L2 Cloud product. Aerosols are not explicitly considered in the baseline. Surface reflection is either considered as LER as in heritage algorithms (baseline) or using the dynamic map of the Bidirectional Reflectance Factor (BRF) model coefficients for both surface types provided by the S4 L2 Gapless Surface Reflectance (GSR) support product ([RD06]) (future development).

5 Algorithm description

5.1 Overview

The basic structure of the S4 NO_2 algorithm with its most important data fields is illustrated in Figure 5.1. The NO_2 column retrieval flow is indicated in green. The algorithm consists of four processing modules, which are indicated in red. These are the DOAS, STRAT, BG and AMF modules. An additional module called ECA pre-processes the model data and is common to all relevant S4 Level-2 algorithms. Auxiliary input or intermediate output fields are shown in light blue for static data and dark blue for dynamic data. Except for the BG module (see below), processing is data-driven: the data flow is the data stream for a single pixel.

Earth radiance spectra and the daily solar irradiance measurement (L1 spectra) are read by the DOAS module, which performs the spectral fit and yields total slant column densities (SCDs). Auxiliary inputs for the spectral fit are the high-resolution absorption cross-sections for NO_2, other trace gases and pseudo-absorbers (reference spectra), the instrument spectral response functions and a high-resolution solar irradiance reference spectrum (Fraunhofer atlas).

The separation of slant columns into a stratospheric and tropospheric part is performed in the STRAT module. Inputs are the stratospheric air mass factor (AMF_{strat}) and the stratospheric vertical column from a model forecast (VCD_{strat}). Stratospheric slant columns are calculated and subtracted from the total slant column to give the tropospheric slant column density (SCD_{trop}). Whenever needed, striping corrections to the fitted slant column densities are applied first. As a final step, the conversion of tropospheric slant columns to vertical columns using the tropospheric air mass factor (AMF_{trop}) is performed in this module as well. The main auxiliary input fields for the STRAT module originate from the AMF module.

The AMF module contains look-up tables of altitude-resolved air mass factors. Box air mass factors are a function of the observation geometry, the reflection properties of the atmosphere's lower bounding surface (i.e. the ground surface or an optically thick cloud) and the pressure of the lower bounding surface (i.e. surface pressure or cloud pressure). NO_2 profile shapes and temperature profiles are needed to calculate air mass factors including corrections for the temperature dependence of the NO_2 absorption cross-section. A sub-module called CLD (not shown here) calculates the relevant cloud parameters for the NO_2 fit window based on the cloud parameters provided by the S4 L2 Cloud product.

The BG module calculates background corrections that are applied in the STRAT module. Corrections may be needed for stripe offsets in fitted slant columns applied in STRAT. Bias correction patterns are updated once per day (time-driven processing) by the BG auxiliary processor from analyses of the differences in retrieved and modelled columns over a period of hours to days.

The main output field of the S4 NO_2 product is the tropospheric vertical column. The sum of the tropospheric column and the background-corrected stratospheric column as given by the global analysis system is a true estimate of the total NO_2 column. Many error diagnostics and the column averaging kernel (AVK) are transferred to the output product as well. The individual processing modules will be described in detail in the following sections.

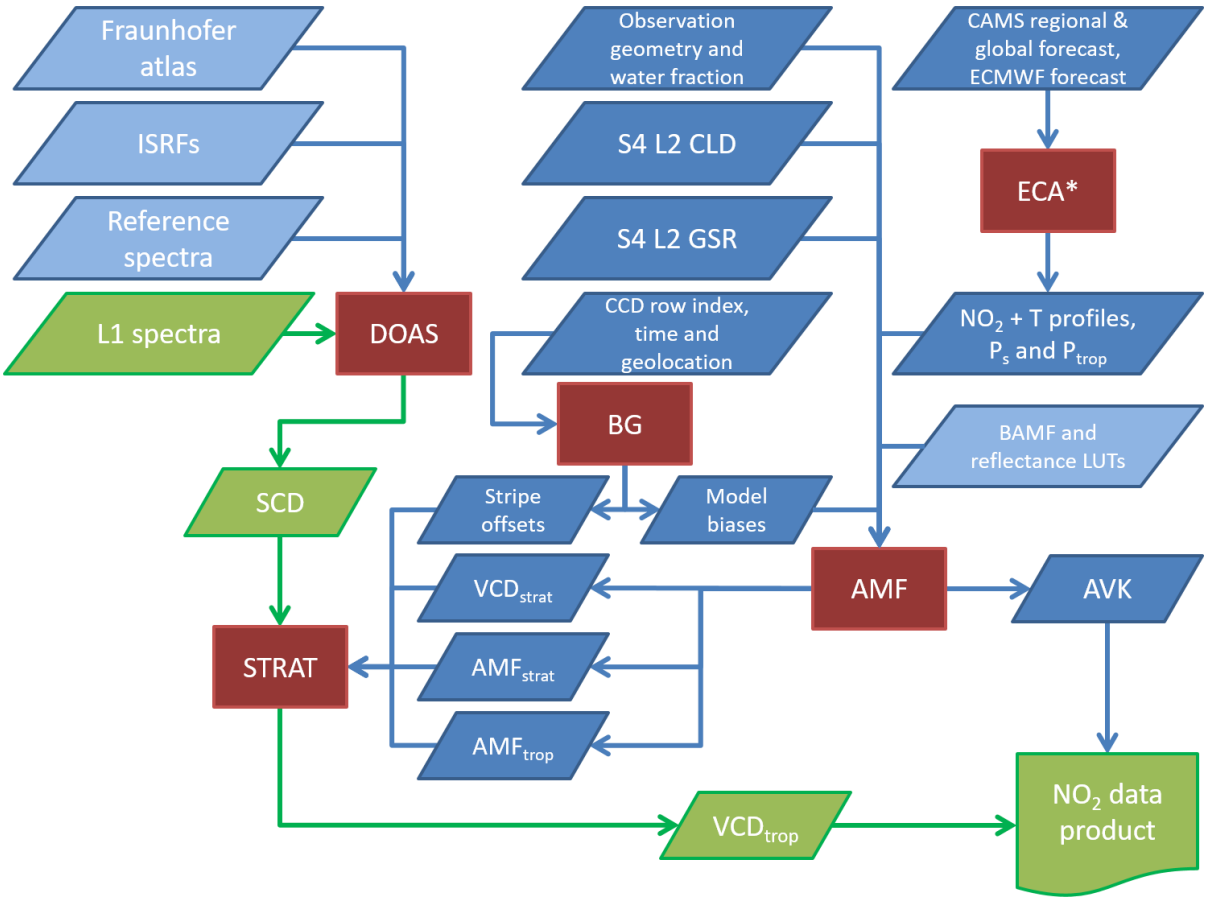

Figure 5.1. The basic structure of the S4 NO_2 algorithm with its most important data fields. The NO_2 column retrieval data flow is indicated in green. The algorithm consists of four processing modules, which are indicated in red (modules DOAS, STRAT, BG and AMF). An additional module called ECA pre-processes the model data and is common to all applicable S4 Level-2 processors (indicated by the *). A sub-module of the AMF module calculates cloud parameters for the NO_2 fit window (sub-module CLD, not shown here). Auxiliary input or intermediate output fields are shown in blue (light blue for static data and dark blue for dynamic data). The four modules are described in detail in Sections 5.2 to 5.5. All flow diagrams describe the algorithm's current baseline implementation.

5.2 Spectral fit (DOAS)

5.2.1 Background

Consider an elastically scattering molecular atmosphere bounded from below by a reflecting surface and containing several absorbing trace gases. Photons travel through the atmosphere along certain paths. Now temporarily 'switch off' absorption by one of the trace gases. For each photon that reaches the sensor, count the number of molecules of the particular trace gas that the photon encounters along its path. (See also the discussion of photon paths and the equivalence theorem in chapter 17.1 of Van de Hulst, 1980.) This defines a probability distribution function ρ for the number of molecules $N_{p,j}$ of species j along photon paths to the sensor per unit area perpendicular to the scattered and reflected beams. The probability distribution function is normalized such that

$$\int_0^\infty \rho\left(N_{p,j};\lambda\right) dN_{p,j} = 1 \qquad 5\text{-}1.$$

The distribution depends on the characteristics of the observation (the observation geometry μ, μ_0, φ-φ_0) and on the state of the atmosphere-surface system: reflection and scattering properties, the number density profile of the trace gas under consideration, number density profiles and absorption properties of the other trace gases. The probability distribution will thus also depend on wavelength. 'Switch on' absorption again and repeat this procedure for each absorbing trace gas to determine the respective probability distributions.

For scattered light observations, the Lambert-Beer law applies to each photon path individually and we can thus write the radiance arriving at the sensor I as

$$I(\lambda) = I^{sca}(\lambda) \cdot \int_0^\infty \rho\left(N_{p,1};\lambda\right) e^{-N_{p,1}\sigma_1(\lambda)} dN_{p,1} \cdot \int_0^\infty \rho\left(N_{p,2};\lambda\right) e^{-N_{p,2}\sigma_2(\lambda)} dN_{p,2} \cdot \ldots \qquad 5\text{-}2,$$

where I^{sca} is the radiance in absence of molecular absorption and σ_j are the absorption cross-sections of the various trace gases. In the following, we will indicate the target species with index 1 (e.g. NO_2) and interfering species with index 2 or higher (e.g. O_3). Next we define a quantity N_s according to

$$\int_0^\infty \rho\left(N_{p,j};\lambda\right) e^{-N_{p,j}\sigma_j(\lambda)} dN_{p,j} = e^{-N_{s,j}(\lambda)\sigma_j(\lambda)} \qquad 5\text{-}3.$$

Equation 5-3 is generally valid as for a given wavelength the equation can always be solved for N_s; this quantity typically depends on wavelength.

In the DOAS method, the assumption is made that absorption by each trace gas is weak, i.e. for every λ: $N_{p,j}\sigma_j(\lambda) \ll 1$ for every $N_{p,j}$, hence $N_{s,j}(\lambda)\sigma_j(\lambda) \ll 1$. This assumption has two implications here. First, when absorption by trace gas j is weak the exponential can be approximated by a truncated Taylor series, as in

$$\begin{aligned}\int_0^\infty \rho\left(N_{p,j};\lambda\right) e^{-N_{p,j}\sigma_j(\lambda)} dN_{p,j} &\approx \int_0^\infty \rho\left(N_{p,j};\lambda\right)\left(1 - N_{p,j}\sigma_j(\lambda)\right) dN_{p,j} \\ &= 1 - \sigma_j(\lambda)\int_0^\infty \rho\left(N_{p,j};\lambda\right) N_{p,j} dN_{p,j} \approx e^{-\sigma_j(\lambda)\int_0^\infty \rho\left(N_{p,j};\lambda\right) N_{p,j} dN_{p,j}}\end{aligned} \qquad 5\text{-}4.$$

Comparing the right-hand sides of Equations 5-3 and 5-4, it becomes clear that quantity N_s can now be interpreted as the number of molecules along an average photon path to the sensor per unit area perpendicular to the beam. This quantity is called the slant column density. Second, when absorption by the other trace gases is weak, we can assume that the probability distribution $\rho\left(N_{p,j};\lambda\right)$ of species j no longer depends on the concentration profiles and absorption properties of these other trace gases. The probability distribution will be smoothly wavelength dependent as it only depends on the scattering and reflection properties of the atmosphere-surface system and on the observation geometry. Hence, also the slant column density $N_{s,j}$ will be at most smoothly wavelength dependent.

For now we simply assume that the slant column densities of the target species as well as of all other absorbers are constant with wavelength and write

$$N_{s,j}(\lambda) = N_{s,j} \qquad 5\text{-}5.$$

Combining Equations 5-2, 5-3 and 5-5, dividing by the solar irradiance E_0 and taking the natural logarithm, we get

$$\ln\left(\frac{I(\lambda)}{E_0(\lambda)}\right) = \ln\left(\frac{I^{sca}(\lambda)}{E_0(\lambda)}\right) - \sum_j N_{s,j}\sigma_j(\lambda) \quad \text{5-6.}$$

In absence of molecular absorption, the (logarithm of the) sun-normalized radiance is only smoothly wavelength dependent and can thus be described by a low-order polynomial. We now arrive at the classic DOAS equation

$$\ln\left(\frac{I(\lambda)}{E_0(\lambda)}\right) = \sum_p c_p\lambda^p - \sum_j N_{s,j}\sigma_j(\lambda) \quad \text{5-7.}$$

For later reference we remark that since we assume weak absorption, the exponential can be linearized and Equation 5-7 may be further approximated as

$$\frac{I(\lambda)}{E_0(\lambda)} = \sum_p c_p\lambda^p\left(1 - \sum_j N_{s,j}\sigma_j(\lambda)\right) \quad \text{5-8,}$$

where the polynomial coefficients are different.

Strictly speaking, Equation 5-7 has been derived for monochromatic radiation. If we indeed want to use measured radiance $\tilde{I}(\lambda_i)$ and irradiance $\tilde{E}_0(\lambda_i)$ spectra, we need to account for the finite resolution of the instrument. Thus, if S and S_0 are the ISRFs of the radiance and irradiance measurements, respectively, which are normalized over the integration range for the convolution as

$$\int S(\lambda;\lambda_i)\,d\lambda = 1 \text{ and } \int S_0(\lambda;\lambda_i)\,d\lambda = 1 \quad \text{5-9,}$$

the measured radiance and irradiance are then written as

$$\tilde{I}(\lambda_i) = \int S(\lambda;\lambda_i)\,I(\lambda)d\lambda \text{ and } \tilde{E}_0(\lambda_i) = \int S_0(\lambda;\lambda_i)\,E_0(\lambda)d\lambda \quad \text{5-10.}$$

In the following we assume that the two ISRFs are the same (written as S), but we come back to this point in Section 5.7.2 when discussing effects of inhomogeneous slit illumination.

The measured sun-normalized radiance is given by

$$\frac{\tilde{I}(\lambda_i)}{\tilde{E}_0(\lambda_i)} = \frac{\int S(\lambda_i,\lambda)I(\lambda)d\lambda}{\int S(\lambda_i,\lambda)E_0(\lambda)d\lambda} \quad \text{5-11.}$$

Substituting the monochromatic radiance using Equation 5-8, we get after some rearrangement of terms (see also Section 5.7.2)

$$\frac{\tilde{I}(\lambda_i)}{\tilde{E}_0(\lambda_i)} = \sum_p c_p\lambda^p\left(1 - \sum_j N_{s,j}\tilde{\sigma}_j(\lambda_i)\right) \quad \text{5-12,}$$

where the absorption cross-section after convolution $\tilde{\sigma}(\lambda_i)$ - to be distinguished from the monochromatic cross-section $\sigma(\lambda)$ - is given by

$$\tilde{\sigma}(\lambda_i) = \frac{\int S(\lambda_i,\lambda)E_0(\lambda)\sigma(\lambda)d\lambda}{\int S(\lambda_i,\lambda)E_0(\lambda)d\lambda} \approx \int S(\lambda_i,\lambda)\sigma(\lambda)d\lambda \quad \text{5-13.}$$

Thus, the convolution of monochromatic absorption cross-sections is weighted with the irradiance spectrum (also known as the 'I_0-effect') in case of weak absorption. The correction for the I_0-effect actually implemented in the bread-board algorithm proceeds in a slightly different way following Aliwell et al. (2002). However, from experience we know that ignoring the I_0-effect in the NO_2 retrieval has a negligible impact on the retrieval outcome and therefore the correction is not implemented in the NO_2 baseline algorithm.

Finally, the DOAS equation for measured spectra then reads

$$\ln\left(\frac{\tilde{I}(\lambda_i)}{\tilde{E}_0(\lambda_i)}\right) = \sum_{p=0}^{4} c_p \lambda_i^p - \sum_j N_{s,j}\tilde{\sigma}_j(\lambda_i) + \epsilon \qquad 5\text{-}14,$$

where ϵ is the error to be minimized. This is the central equation to solve. It is a system of m equations, where m is the number of spectral points in the fit window. The equations are linear in the unknown quantities $N_{s,j}$ and c_p, and the least-squares solution can be readily obtained, the NO_2 slant column density being the quantity of interest here. The absorption cross sections $\tilde{\sigma}(\lambda_i)$ are given by the right-hand side of Equation 5-13. In the DOAS module, solving the DOAS equation is however implemented as part of a more convolved iterative scheme, because additional steps have to be taken that are related to spectral calibration, spectral interpolation and treatment of outliers for the radiance and irradiance spectra. This is described in detail in the following sections.

A flow diagram of the DOAS module is given in Figure 5.2. Once a day, when a new irradiance measurement becomes available, the irradiance spectrum is wavelength calibrated and the absorption cross sections are prepared for the DOAS fit from reference spectra, the ISRFs and the calibrated irradiance wavelength grid. The DOAS equation is solved and the main result is the NO_2 slant column.

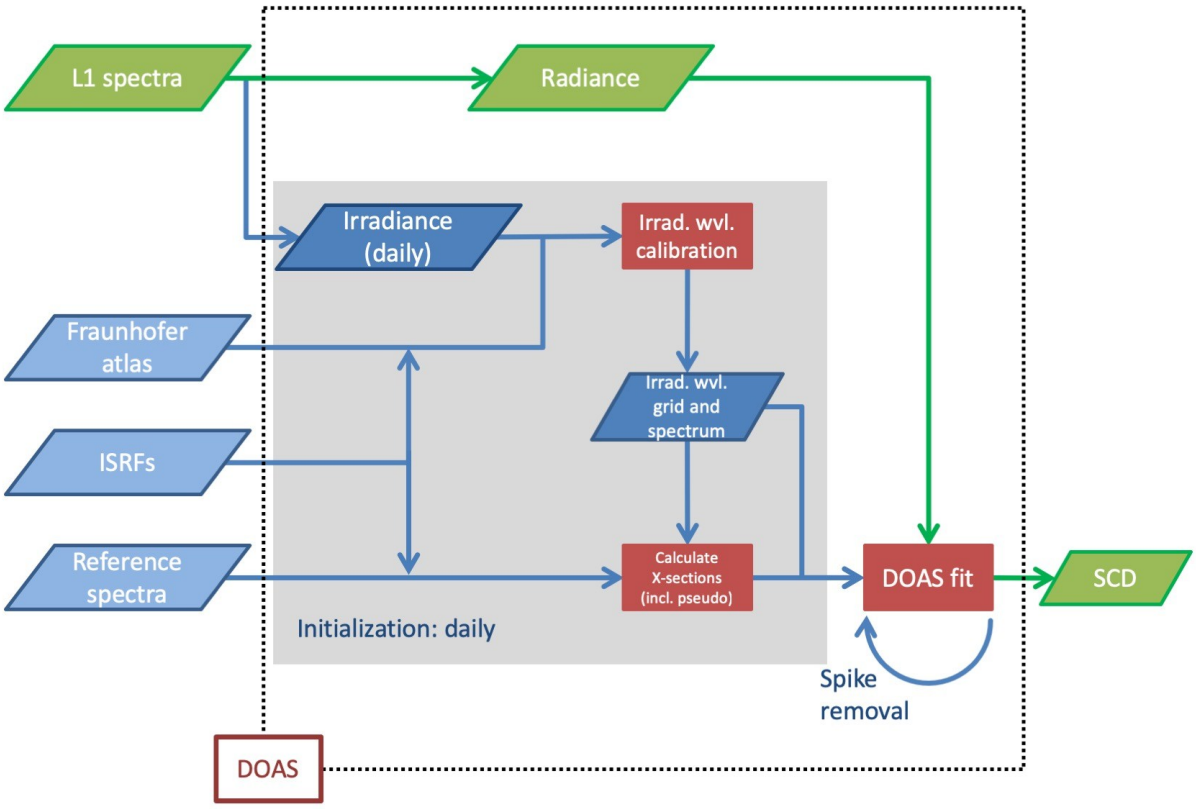

Figure 5.2. The structure of the DOAS algorithm module with its most important data fields. See also the caption of Figure 5.1. For a list of the absorbers and pseudo-absorbers included in the baseline fit, see Table 5.1.

In our derivation we have assumed that the absorption cross-sections do not vary along photon paths. This is typically not the case because of the temperature and pressure variations in the atmosphere. For species absorbing in the ultraviolet and visible wavelength range, the pressure dependence can often be ignored and only temperature variations need to be taken into account. For NO_2, the temperature dependence is strong, but it mainly results in a scaling of the differential structure of the absorption cross-section while leaving the spectral shape mostly unaffected. There are various ways to account for this temperature dependence. Because the scaling of the differential absorption cross-section with temperature directly translates into a scaling of fitted slant column densities, a convenient approach is to simply fit slant columns using an NO_2 differential absorption cross-section at a certain reference temperature and apply temperature correction factors to the altitude-resolved air mass factors in the AMF module (Boersma et al., 2004). This will be described in Section 5.5.11.

Inelastic scattering is also not considered explicitly in the derivation of the DOAS equation. Rotational Raman scattering in the atmosphere can be modelled as a perturbation to the solution for elastically scattered light by introducing a particular pseudo-absorber. A so-called Ring cross-section, calculated with a radiative transfer model, is included in the fit. This accounts for the spectral signature of the filling-in by rotational Raman scattering of Fraunhofer lines but not of NO_2 absorption structures (Fish et al, 1995). Inelastic scattering on water molecules can be relevant over ocean and can in principle be treated in the same way. However, vibrational Raman scattering is ignored here as it can in good approximation be approximated by the stray light correction (Vountas et al., 2003). Other possible pseudo-absorbers are related to instrument stray light or not fully corrected polarisation features, correct for spectral undersampling or inhomogeneous scene effects, account for any wavelength dependence of the air mass factor across the fit window, or result from a linearization of the spectral calibration step.

Finally, we haven't taken into account the effect of aerosols. Aerosols scatter and sometimes also absorb, and aerosol scattering and absorption cross-sections are smoothly wavelength dependent. Particle extinction will affect the probability distributions and the background radiance I^{sca} (i.e. the radiance in absence of molecular absorption) in Equation 5-2.

The fit window extends from 425 to 497 nm. A large fit window is preferred in the sense that more spectral points make for a smaller noise error. The upper limit is set at 497 nm, because at longer wavelengths strong water vapour absorption starts to interfere (but we also reach the end of the spectral range of S4's VIS band). Below 425 nm, absorption by NO_2 becomes less and from experience we know that extending to smaller wavelengths gives no significant improvement. This point should however be revisited once real S4 measurements become available. The degree of the background polynomial is 4 (i.e. 5 coefficients), which sufficiently captures the spectral variation of atmospheric scattering and surface reflection across the fit window. In case of S4 Level-1 calibration issues, a larger polynomial degree might become necessary.

Finally, the DOAS module not only outputs slant column densities but also an estimate of their uncertainties. The uncertainty in the spectrum (considered as a white noise error) is estimated from the root-mean-square deviation of the fit and subsequently propagated to an uncertainty in the retrieved slant column. Here, the root-mean-square deviation Δ_{RMS} is defined according to

$$\Delta_{RMS}^2 = \frac{1}{m}\sum_{i=1}^{m}\left[y_{meas}(\lambda_i) - y_{fit}(\lambda_i)\right]^2 \qquad 5\text{-}15,$$

where y is the logarithm of the sun-normalized radiance and m is the number of spectral points used in the final fit. The error covariance matrix $\mathbf{S}$ for the vector of fit parameters is given by

$$\mathbf{S} = \frac{m}{m-n}\Delta_{RMS}^2(\mathbf{K}^T\mathbf{K})^{-1} \quad \text{5-16,}$$

where n is the number of fit parameters, m-n is the number of degrees of freedom of the estimator and $\mathbf{K}$ is the matrix of coefficients of the linear model (λ_i^p and $\tilde{\sigma}_j(\lambda_i)$). The uncertainty in the NO_2 slant column is the square root of the corresponding diagonal element.

We remark that the DOAS equation and the equations for the spectral calibration (Section 5.2.3) are solved using non-weighted least squares (i.e. the error covariance matrix of the measurement is the identity matrix) implying that any noise and uncertainty spectra in the Level-1b product are not used. Similarly, the uncertainty in the fitted slant column is estimated from the fit residual rather than from a propagation of L1b noise and uncertainties.

For imaging spectrometers using a two-dimensional CCD detector, like S4, some characteristics of the radiance measurement such as slit function and spectral alignment are expected to be much more similar within a row across subsequent integration times than across rows for a particular read-out. The rows of the CCD correspond to the different across-track viewing directions. In order to take advantage of this similarity, we analyse the data stream as much as possible by row. For each row, a slit function is provided by the calibration team and a daily irradiance measurement is made. Hence, also the wavelength grid on which the DOAS fit is performed and the absorption cross-sections need to be determined for each row once a day. If the linearized radiance wavelength calibration is used (see Section 5.2.3.2), it is important to have good first guesses for the wavelength shift and stretch. In the bread-board algorithm, these values are provided by the fit result of the previous along-track pixel in the same row. However, due to the specific processing topology, this is not possible in the S4 L2 operational processor.

5.2.2 Reference spectra and absorption cross-sections

In addition to the target species NO_2, other trace gases that show significant absorption in the fit window are O_3, O_4 and H_2O_{vap}. Absorption by liquid water (H_2O_{liq}) will be taken into account as well, because it can have a large contribution over the ocean at clear sky conditions and small solar zenith angle. Pseudo-absorbers considered in any case are related to rotational Raman scattering in the atmosphere, which is described by a Ring spectrum, and instrument stray light, which is assumed to be inversely proportional to the irradiance spectrum.

If this proves to be necessary for S4, pseudo-absorbers may have to be added that account for spectral undersampling of the spectrometer, the instrument's polarisation sensitivity (see section 5.8.4) or spectral artefacts introduced by molecular contamination. Inclusion of a cross-section representing the non-linear wavelength dependence of the air mass factor is currently under investigation. The same holds for pseudo-absorber cross-sections related to inhomogeneous slit illumination (see section 5.8.2). The decision on which corrections are actually needed and what they should look like will be determined once the instrument is in orbit and has been measuring for a sufficiently long period. The current implementation contains five placeholder cross-sections based on preliminary data provided by Airbus. Details on the pseudo cross-sections will be provided as soon as the cross-sections have been finalised during the commissioning phase of S4.

Finally, in case the spectral calibration of the radiance spectrum is linearized, two additional cross-sections representing the effects of shifts and stretches of the wavelength axis need to be included in the DOAS fit. A list of all absorbers and their reference spectra is given in Table 5.1, while Figure 5.3 shows the cross-sections. Below we will discuss in somewhat more detail how the absorption cross-sections $\tilde{\sigma}(\lambda_i)$ for the different absorbers are calculated.

The absorption cross-sections for the trace gases are determined from high-resolution reference spectra according to Equation 5-13. Reference spectra are convolved with the nominal S4 ISRF (rectangle method) for each detector row. All absorption cross-sections are prepared in this way at a high-sampling wavelength grid (typically 0.01 nm) offline with the exception of the liquid water absorption coefficient, which is assumed to be broadband. Once per day, the absorption cross-sections are interpolated to the actual irradiance wavelength grid (cubic spline interpolation).

Table 5.1: Absorbers and pseudo-absorbers included in the DOAS fit in the baseline implementation and the source of their reference spectra.

Absorber	Reference spectrum	Remark
NO_2	Vandaele et al. (1998) or Vandaele et al. (2002)	Reference temperature of 220 K.
O_3	Serdyuchenko et al. (2014), Gorshelev et al. (2014)	Reference temperature of 243 K.
O_4	Thalman and Volkamer (2013)	Reference temperature of 293 K.
H_2O_{vap}	HITRAN line parameters (Rothman et al., 2013)	Average absorption cross section for a reference atmosphere.
H_2O_{liq}	Absorption coefficient measured by Pope and Frey (1997)	No convolution with the S4 ISRF is performed, but other preparation steps are needed. See text for details.
Ring	$\ln\left(\frac{\int S(\lambda_i,\lambda) I_{Ray+Ram}(\lambda) d\lambda}{\int S(\lambda_i,\lambda) I_{Ray}(\lambda) d\lambda}\right)$	Calculated with SCIATRAN following Vountas et al. (1998), see main text.
Stray light	$\left(1/\tilde{E}_0(\lambda_i)\right)_{diff}$	Stray light is additive radiance offset constant with wavelength, see main text.
Shift spectrum	$\frac{d\ln(\tilde{E}_0(\lambda_i))}{d\lambda}$	In case the radiance wavelength calibration is linearized. Following Beirle et al. (2013), see Section 5.2.3.2.
Stretch spectrum	$\frac{d\ln\left(\tilde{E}_0(\lambda_i)\right)}{d\lambda}(\lambda_i - \lambda_c)$	In case the radiance wavelength calibration is linearized. Following Beirle et al. (2013), see Section 5.2.3.2.

The O_4 absorption cross-section, as measured for example by Thalman and Volkamer (2013), includes the equilibrium constant between concentrations of O_2 and the O_2-O_2 collision pair. The absorption cross-section is therefore expressed in units of cm^5 $molecule^{-2}$, and the fit coefficient is the O_2 concentration squared and integrated along the slant path. The O_4 slant column is proportional to the fit coefficient and the proportionality factor is the unknown temperature-independent equilibrium constant (in units of cm^3 $molecule^{-1}$).

Water vapour is a line absorber and its line parameters are taken from the HITRAN database. The water vapour absorption cross-section that is used in the DOAS fit is an average absorption cross section calculated for a reference atmosphere (temperature and pressure profile) at high spectral resolution and sampling.

Pope and Fry (1997) report absorption coefficients of pure water at 295 K at a relatively coarse resolution of 5 to 7 nm. These values are smoothed and interpolated onto a finer spectral grid. No additional convolution with the S4 ISRF is performed. The fit coefficient should be interpreted as a slant path length in water. The absorption coefficient of liquid water will always be included in the fit, because this will improve the fit over ocean without introducing artefacts or deteriorating the fit over land (Alvarado et al., 2014, Alvarado, 2016).

Equation 5-14 is derived for elastically scattered radiance I_{elast}, while the measured spectrum has an elastically and a (much smaller) inelastically scattered component $I_{inelast}$. To account for inelastic scattering, Equation 5-14 is modified by adding to the right-hand side a term that is equal to the logarithm of the ratio of $I_{elast+inelast}$ and I_{elast} (derivation not shown). Of course, this term depends on the observation geometry and the atmospheric state (including profiles of atmospheric absorbers). However, most of the spectral structures due to inelastic scattering can be removed by modelling this term for a typical scenario without NO_2 absorption and including it in the fit (with a fit coefficient). The so-called Ring spectrum is calculated from a Fraunhofer atlas and two SCIATRAN radiance simulations at high spectral resolution, one including the effect of rotational Raman scattering in air and the other one excluding it. These spectra are calculated for a pure Rayleigh atmosphere in a typical scenario and thus do not include the variability of the Ring effect with surface albedo, observation geometry or clouds. They also do not include the effect of filling-in of NO_2. The Ring pseudo cross-section is then calculated from the ratio of the two spectra, each convoluted with the instrument slit function:

$$\tilde{\sigma}_{Ring}(\lambda_i) = \ln\left(\frac{\int S(\lambda_i,\lambda) I_{Ray+Ram}(\lambda) d\lambda}{\int S(\lambda_i,\lambda) I_{Ray}(\lambda) d\lambda}\right) \quad \text{5-17.}$$

Residual instrument stray light (i.e. stray light that is not corrected in the Level-1b processor) is an additive radiance offset. To account for small additive offsets $A(\lambda_i)$ in the measured radiance, a term has to be added to the right-hand side of Equation 5-14 that is equal to $A(\lambda_i)/\tilde{I}(\lambda_i)$ (derivation not shown). When we assume the additive offset to be constant with wavelength, as we do in absence of better information, we may retrieve the offset by including a cross-section in the fit given by the

$$\tilde{\sigma}_{add}(\lambda_i) = \frac{1}{\tilde{I}(\lambda_i)} \quad \text{5-18}$$

and the fit coefficient is the offset A. This makes solving the DOAS equation somewhat impractical to implement because the stray light cross-section needs to be determined again for every pixel. More importantly, when the spectral shape of the stray light is assumed constant, the stray light cross-section and other absorption cross-sections may become linearly dependent. Instead, we assume the stray light cross-section to be inversely proportional to the solar irradiance, which has proven to give good results, and write

$$\tilde{\sigma}_{stray}(\lambda_i) = \frac{1}{\tilde{E}_0(\lambda_i)} \quad \text{5-19.}$$

Now the stray light cross-section has to be determined only once per day when a new solar irradiance measurement becomes available. The fit coefficient for the stray light cross-section of Equation 5-19 can be interpreted as the radiance offset A_{stray} divided by the average sun-normalized radiance across the fit window. Finally, from experience we know that fitting stray light offsets may also help to capture Ring deficiencies.

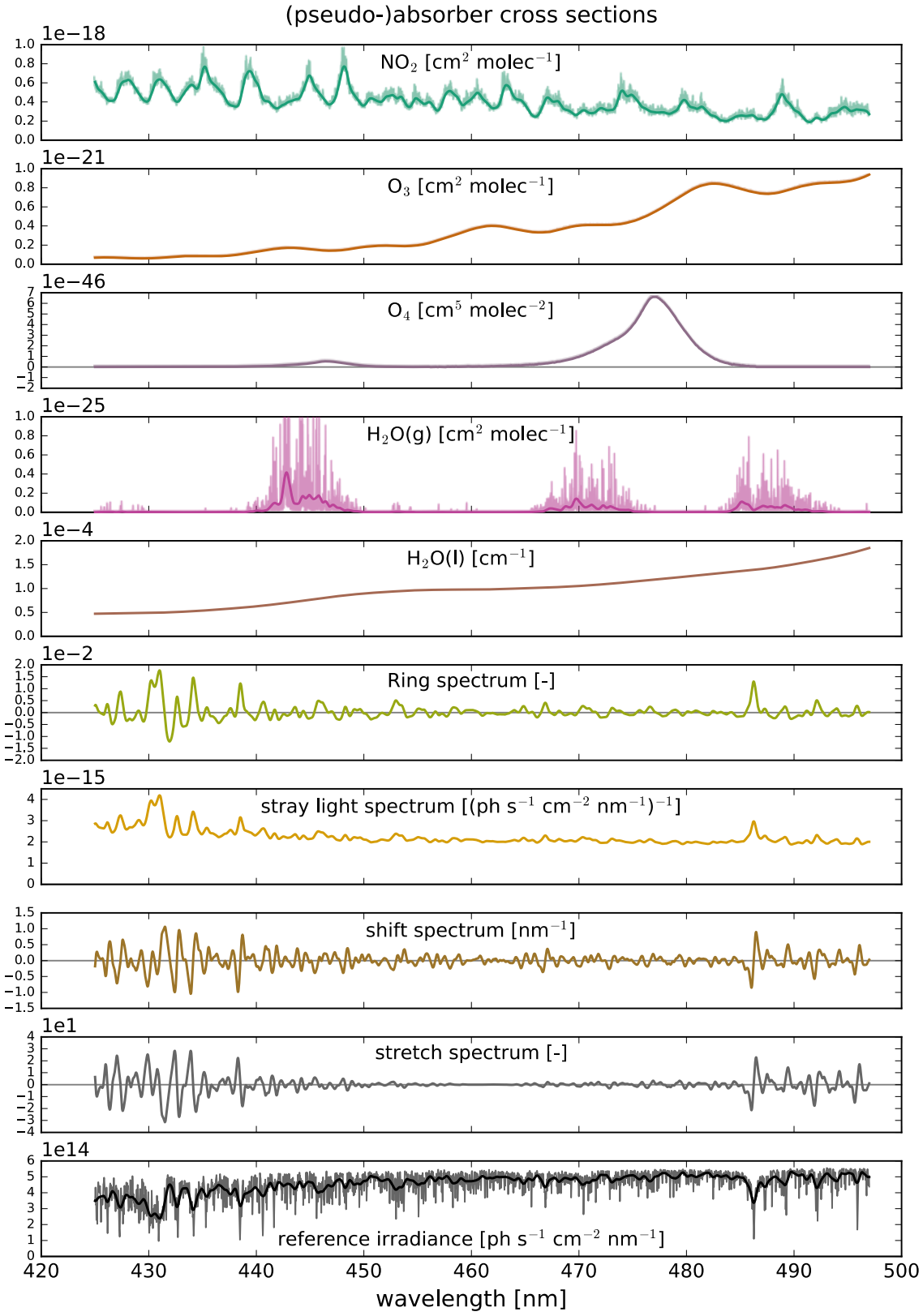

Figure 5.3. Absorption cross-sections of all absorbers and pseudo-absorbers as they are used in the DOAS fit in the baseline implementation. For details, see the main text. The last panel shows the irradiance spectrum for comparison.

5.2.3 Spectral calibration and interpolation, treatment of outliers

5.2.3.1 Irradiance wavelength calibration

As the solar spectrum is highly structured by Fraunhofer lines and we are dealing with weak absorption, even small differences in the wavelength registration of $\tilde{I}$ and $\tilde{E}_0$ lead to residuals that are of the same order of magnitude as the spectral structures from which we retrieve NO_2. Although a general wavelength calibration will be performed in the Level-1b processor, additional spectral calibration steps for the specific fit window are taken in the NO_2 Level-2 algorithm to further improve the accuracy of retrieved slant columns. More specifically, the radiance and irradiance need to be absolutely wavelength calibrated and brought onto the same grid, and spectral outliers may have to be removed.

The Level-1b product provides radiance and irradiance spectra on a nominal wavelength grid $\lambda_{i,nom}$ that is corrected for the Doppler shift in the satellite's reference frame and to some extent perhaps calibrated, but supposedly different from the true wavelength grid $\lambda_{i,true}$ because of remaining spectral calibration errors. The offset between the two wavelength grids may in turn depend on wavelength. Here we consider only linear variations and fit a constant wavelength shift (s) and a stretch / squeeze parameter (q). In the remainder of this document, we refer to parameter q as stretch. We take the following approach.

The irradiance measured daily for every detector row is wavelength calibrated by using a high-sampling solar irradiance reference spectrum. This reference spectrum $\tilde{E}_0^{ref}(\lambda_{true})$ is calculated from a high-resolution Fraunhofer atlas (Chance and Kurucz, 2010) by convolution with the corresponding irradiance spectral response function. We write for the true and nominal wavelengths of the i-th node of the irradiance wavelength grid

$$\lambda_{i,true}^{irrad} = \lambda_{i,nom}^{irrad} + \Delta\lambda_i^{irrad} = \lambda_{i,nom}^{irrad} + s + (q-1)\cdot(\lambda_{i,nom}^{irrad} - \lambda_c) \qquad 5\text{-}20,$$

where λ_c is some (arbitrary) reference wavelength, which is here taken to be the centre of the fit window. We follow the convention that parameter s is zero in absence of a wavelength shift and parameter q is one in absence of a stretch, which is in agreement with Beirle et al. (2013). Then, the following equation is solved

$$\ln\left(\tilde{E}_0^{meas}\left(\lambda_{i,nom}^{irrad}\right)\right) = \ln\left(\tilde{E}_0^{ref}\left(\lambda_{i,nom}^{irrad} + s + (q-1)\cdot\left(\lambda_{i,nom}^{irrad} - \lambda_c\right)\right)\right) + \sum_p c_p\left(\lambda_{i,nom}^{irrad}\right)^p + \epsilon \qquad 5\text{-}21.$$

The polynomial of, for example, degree four or five accounts for variation of the sun-earth distance, and radiometric calibration and degradation offsets. As the equation is non-linear, its least-squares solution for the shift and stretch parameters (s and q) and the polynomial coefficients is found iteratively (Levenberg-Marquardt scheme). Since the reference spectrum $\tilde{E}_0^{ref}(\lambda_{true})$ is available at a high sampling of 0.01 nm, interpolation errors will be small (cubic spline interpolation is used). Derivatives needed for the updates during iteration are calculated analytically from the spline. Once the fit has converged, the true wavelengths of the irradiance grid $\lambda_{i,true}^{irrad}$ are calculated (Equation 5-20) and the nodes are re-labelled. This is the wavelength grid on which the cross-sections are prepared and the DOAS fit is performed.

5.2.3.2 Radiance wavelength calibration and interpolation

The baseline implementation is to use the same non-linear fitting scheme applied for the calibration of the irradiance also for the radiance wavelength calibration. The radiance from the Level-1b product is reported on a nominal wavelength grid $\lambda_{i,nom}^{rad}$, while it is needed on the calibrated irradiance wavelength grid $\lambda_{i,true}^{irrad}$. We write for the difference between the two grids

$$\Delta\lambda_i = \lambda_{i,true}^{irrad} - \lambda_{i,nom}^{rad} = s + (q-1)\cdot(\lambda_{i,true}^{irrad} - \lambda_c) \quad \text{5-22.}$$

The DOAS equation (Equation 5-14) is solved iteratively in basically the same way as in the irradiance wavelength calibration step; we now have

$$\ln\left(\tilde{I}\left(\lambda_{i,true}^{irrad} - s - (q-1)\cdot\left(\lambda_{i,true}^{irrad} - \lambda_c\right)\right)\right) = \ln\left(\tilde{E}_0\left(\lambda_{i,true}^{irrad}\right)\right) + \sum_{p=0}^{4} c_p\left(\lambda_{i,true}^{irrad}\right)^p - \sum_j N_{s,j}\tilde{\sigma}_j\left(\lambda_{i,true}^{irrad}\right) + \epsilon \quad \text{5-23.}$$

Once the fit has converged, fitted slant columns and other fit coefficients are saved to output for further processing.

There is a small difference between the irradiance and radiance spectral calibration. In the irradiance wavelength calibration, the reference irradiance is spline interpolated to determine the true wavelength grid of the measured irradiance. The reference irradiance is available at high spectral sampling. In the radiance wavelength calibration (i.e. the DOAS fit), the measured radiance is spline interpolated onto the true wavelength grid of the measured irradiance and from the ratio of the interpolated radiance and the measured irradiance the slant columns are determined. The measured radiance is available only on the coarser instrument wavelength grid. Overall, we may expect additional interpolation noise introduced in the radiance wavelength calibration step compared to the irradiance spectral calibration.

Alternatively, we can use the approach of Beirle et al. (2013) for the wavelength calibration of the radiances. It consists of creating two pseudo-absorbers representing the linearized effects of a shift and a stretch of the radiance wavelength axis, which are then included in the DOAS fit. The approach has been shown to be very accurate for small values of shift and stretch (i.e. when the difference between the true and reported radiance wavelength axes are small) and increases the calculation speed significantly compared to a non-linear implementation. This approach to the radiance wavelength calibration affects the way the interpolation of the radiance spectrum onto the irradiance wavelength axis is performed.

In this approach, the radiance spectrum from the L1b product is first directly interpolated (cubic spline) onto the calibrated irradiance wavelength grid. However, the overall shift between the two grids $\Delta\lambda_i = \lambda_{i,true}^{irrad} - \lambda_{i,nom}^{rad} = \left(\lambda_{i,true}^{irrad} - \lambda_{i,true}^{rad}\right) + \left(\lambda_{i,true}^{rad} - \lambda_{i,nom}^{rad}\right)$ consists of a true shift (first term on right-hand side) as well as a radiance wavelength calibration error (second term on right-hand side). The interpolation thus overshoots by a small amount

$$\Delta\lambda_i^{rad} = \lambda_{i,true}^{rad} - \lambda_{i,nom}^{rad} = s + (q-1)\cdot(\lambda_{i,nom}^{rad} - \lambda_c) \quad \text{5-24}$$

that needs to be corrected in the DOAS fit.

Next, we linearize the logarithm of the measured radiance

$$\ln\left(\tilde{I}\left(\lambda_{i,true}^{irrad} - \Delta\lambda_i^{rad}\right)\right) \approx \ln\left(\tilde{I}\left(\lambda_{i,true}^{irrad}\right)\right) - \frac{d\ln\left(\tilde{I}\left(\lambda_{i,true}^{irrad}\right)\right)}{d\lambda}\cdot\Delta\lambda_i^{rad} \quad \text{5-25,}$$

and upon using the second equality of Equation 5-24 we find a shift and stretch spectrum

$$\tilde{\sigma}_{shift}(\lambda_i) = \frac{d\ln\left(\tilde{I}\left(\lambda_{i,true}^{irrad}\right)\right)}{d\lambda} \text{ and } \tilde{\sigma}_{stretch}(\lambda_i) = \frac{d\ln\left(\tilde{I}\left(\lambda_{i,true}^{irrad}\right)\right)}{d\lambda}(\lambda_i - \lambda_c) \quad \text{5-26}$$

that need to be added to the right-hand side of Equation 5-14. Thus, when solving the DOAS equation, the radiance spectrum from the Level-1b product may be directly interpolated onto the calibrated irradiance wavelength grid provided a shift and stretch spectrum with fit coefficients *s* and *(q-1)* are added to the right-hand side of the DOAS equation.

An additional approximation is made by replacing the radiance in Equation 5-26 by the irradiance, which is a valid approximation when the optical thickness of atmospheric absorbers is small and the spectral structure of the radiance is dominated by Fraunhofer lines, and we now arrive at the expressions given in Table 5.1. Although these approximations will typically increase the residuals compared to the non-linear calibration case, the errors incurred have been found to be small for NO_2. The advantage of calculating shift and stretch spectra from the irradiance measurement is an additional increase in computational speed. Shift and stretch spectra are derived by cubic spline interpolating the measured irradiance spectrum and calculating derivatives from the spline.

In order to minimise non-linear effects, it is possible to provide a more accurate and stable linearization point for the wavelength calibration by specifying an a priori wavelength shift and stretch, when such information is indeed available. In other words, the radiance is then in fact cubic spline interpolated from the re-labelled $\lambda_{i,prior}^{rad}$ axis to $\lambda_{i,true}^{irrad}$ rather than from $\lambda_{i,nom}^{rad}$, where $\lambda_{i,prior}^{rad} = \lambda_{i,nom}^{rad} + s^{prior} + \left(q^{prior} - 1\right) \cdot (\lambda_{i,nom}^{rad} - \lambda_c)$. An appropriate a priori shift and stretch are the fitted shift and stretch from the previous pixel in the same CCD row. As already explained, these values are not available in the operational processor because there all pixels are processed independently. Thus, a priori wavelength shift and stretch parameters are static with default values zero and one, respectively. We propose however that they are configurable parameters as information from L1b may still at some point suggest to set them to different values.

Furthermore, when the a priori shift or stretch parameters exceed certain threshold values, they are reset to their nearest boundaries before the DOAS equation is solved.

Finally, we mention that the spectral calibration steps described here are expected to also largely account for effects of partial illumination of the instrument slit. This will be explained in more detail in Section 5.7.2.

5.2.3.3 Treatment of spectral outliers

Particularly in the region of the South Atlantic Anomaly, spectral outliers that reduce the fit quality can occur. For polar orbiting satellites, an outlier-removal scheme is therefore implemented when solving the DOAS equation (Richter et al., 2011). Sentinel-4 does not cover the South Atlantic Anomaly and there may be less need for such a scheme but this remains to be seen. In the outlier-removal scheme, an analysis of the residual is performed to identify spectral outliers after the DOAS equation has been solved for the first time. A spectral point is labelled as an outlier if the difference between measured and fitted spectrum (i.e. the logarithm of the sun-normalized radiance) is larger than a threshold value times the root-mean-square deviation of the fit (Equation 5-15) excluding this point and all spectral points identified as outliers so far. The spectrum is searched repeatedly until all outliers have been identified or a maximum number of spectral outliers has been reached. If all outliers are identified, they are removed from the spectrum, the DOAS equation is solved a second time and the outcome of this calculation is the final reported retrieval solution.

5.3 Separation of stratospheric and tropospheric columns (STRAT)

5.3.1 Background

The slant column density retrieved by the DOAS fit contains all NO_2 absorption along the light paths, including both stratosphere and troposphere. In order to determine the tropospheric column, which is the most relevant result of the S4 NO_2 retrieval, a separation between the two components is needed. The baseline implementation uses CAMS model forecasts of stratospheric NO_2 profiles based on assimilation of NO_2 observations from polar orbiting satellites (S5P, S5) to determine stratospheric columns.

Applying the model forecast with data assimilation approach to S4 is challenging for the following three reasons. First, only a small part of the globe is observed by S4, which presents a problem if only S4 slant columns are assimilated. In one day, a large part of the air masses inside the domain will be transported outside the domain, while stratospheric model biases from the unconstrained part of the global model outside the S4 domain will be transported into the S4 domain and degrade the stratospheric estimates. Second, the number of unpolluted pixels within the S4 domain is limited because a large part of the S4 field of view is influenced by boundary layer pollution and in the morning and evening hours S4 measurements are only available for the sun-lit part of the domain viewed by the instrument. Third, the S4 instrument samples the diurnal variability in contrast to the sun-synchronous polar orbiting instruments. The diurnal variability in NO_2, e.g. the chemical conversion between nitrogen species in the stratosphere, needs to be accurately accounted for and this requires detailed stratospheric chemistry schemes.

A detailed flow diagram of the baseline STRAT module is given in Figure 5.4. The module itself contains only a few operations. First, stripe corrections provided by the BG module are applied to the fitted slant column densities from the DOAS module, if needed. The stratospheric vertical column from the model forecast is passed on by the AMF module, which also applies corrections for spatial and temporal model biases. Furthermore, the AMF module provides the stratospheric and tropospheric air mass factors. The stratospheric slant column is calculated and subtracted from the de-striped total slant column. Finally, the tropospheric slant column is converted to a vertical column. The remainder of this section will focus on the model forecasts providing the NO_2 profiles.

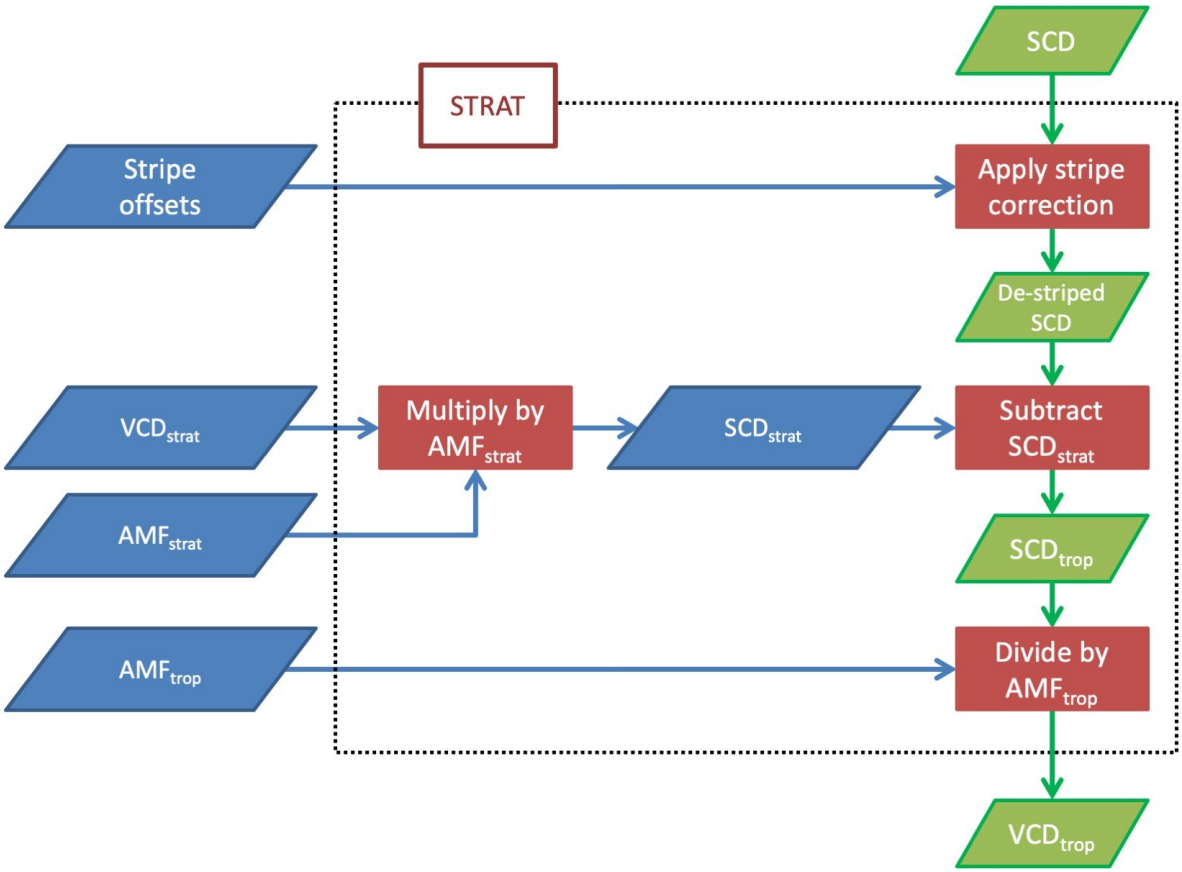

Figure 5.4. The structure of the STRAT algorithm module with its most important data fields. See also the caption of Figure 5.1.

5.3.2 Model forecast with data assimilation

The operational processor will use forecast profiles from the CAMS global analysis system. Advantages of the CAMS system over TM5 as used for TROPOMI are the higher spatial resolution, full stratospheric chemistry, the advanced assimilation setup and its operational implementation. The spatial resolution of the CAMS global model currently is 40 x 40 km, while the resolution of TM5 is not expected to improve beyond its current 1° by 1° anytime soon. The model has 137 vertical layers, which may increase further in the future. The time step of the CAMS output for S4 is 1 h.

5.4 Background corrections (BG)

5.4.1 Background

Background corrections are linked to the stratospheric corrections of the STRAT module. Two types of background corrections are foreseen for S4 NO_2: de-striping of fitted slant columns and corrections of stratospheric forecast columns for model biases. The latter may be related to inter-instrument biases between S4 and the polar-orbiting instrument from which observations are assimilated (S5P or S5) and to inaccurate and unconstrained modelling of the diurnal cycle.

The BG auxiliary processor determines bias correction patterns based on analyses of the differences between retrieved and modelled columns for the past day to days. The details of these analyses, such as the exact time window, depend on the nature of the biases and the final analysis steps can therefore only be consolidated once real data become available. It may even be possible that certain corrections can eventually be switched off. Below we will outline the general approach for determining stripe offsets and spatial and temporal biases in model forecasts as we currently see it.

The BG processor runs once a day during the night and interfaces with the core NO_2 processor through a so-called engineering product. A single BG product file thus contains correction patterns for the coming day, which are based on data up to and including the past day. The processing strategy is such that the BG processor first determines incremental correction patterns from data for the past day. The previous bias correction patterns read from the last BG file are then updated with these incremental bias correction patterns: a weighted average of the two patterns is calculated and the weights basically determine the time window.

The general structure of the BG auxiliary processor is given in Figure 5.5. Key inputs for the calculation of the incremental bias corrections are fitted slant columns, air mass factors and model vertical columns. Here it is important to note that these vertical column forecasts exclude any previous model bias corrections. All fields are available in the main L2 NO_2 product file. Furthermore, bias patterns are parameterized as a function of CCD row index, time, geolocation, etc, and these variables are collected from the L2 file. Pixels are selected when they are in non-polluted or highly cloudy regions, so that slant columns are dominated by stratospheric contributions. Additional parameters are needed for this filtering step and taken from the L2 product as well. Incremental bias correction patterns are subsequently calculated, previous patterns are updated, and the new bias correction patterns are stored in a BG engineering product file.

These stripe and model bias patterns are then used to calculate stripe offsets and model bias corrections for the S4 pixel under consideration. This is done in the BG algorithm module, which is illustrated in Figure 5.6.

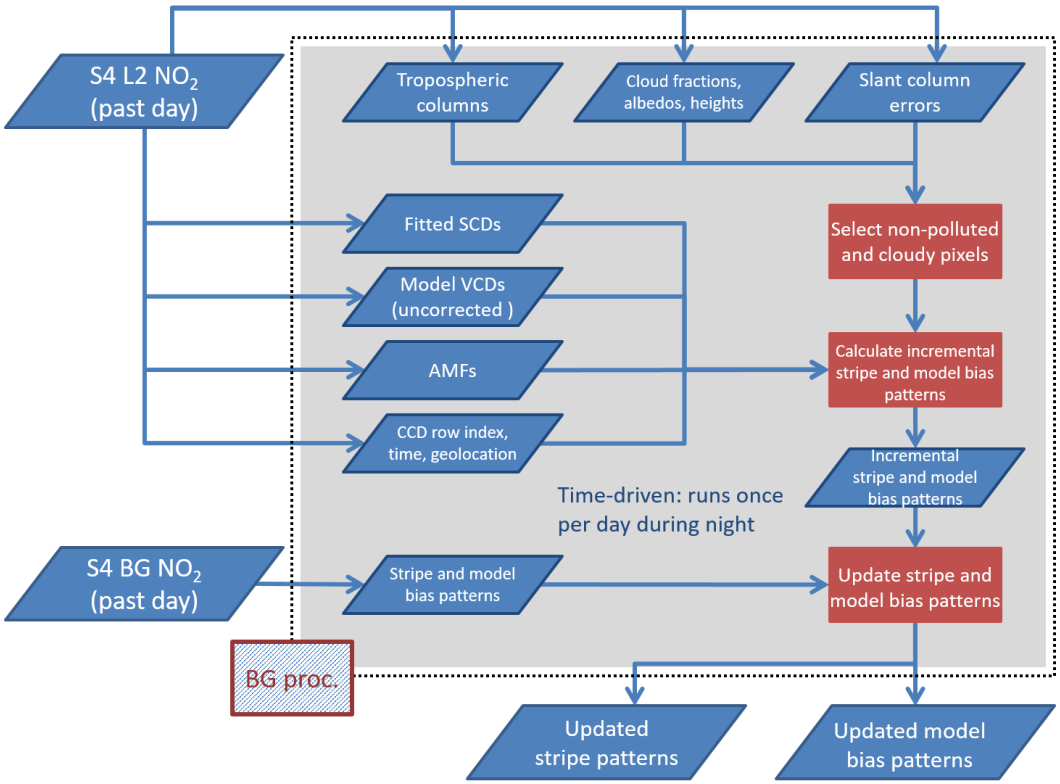

Figure 5.5. The structure of the BG auxiliary processor with its most important data fields. See also the caption of Figure 5.1.

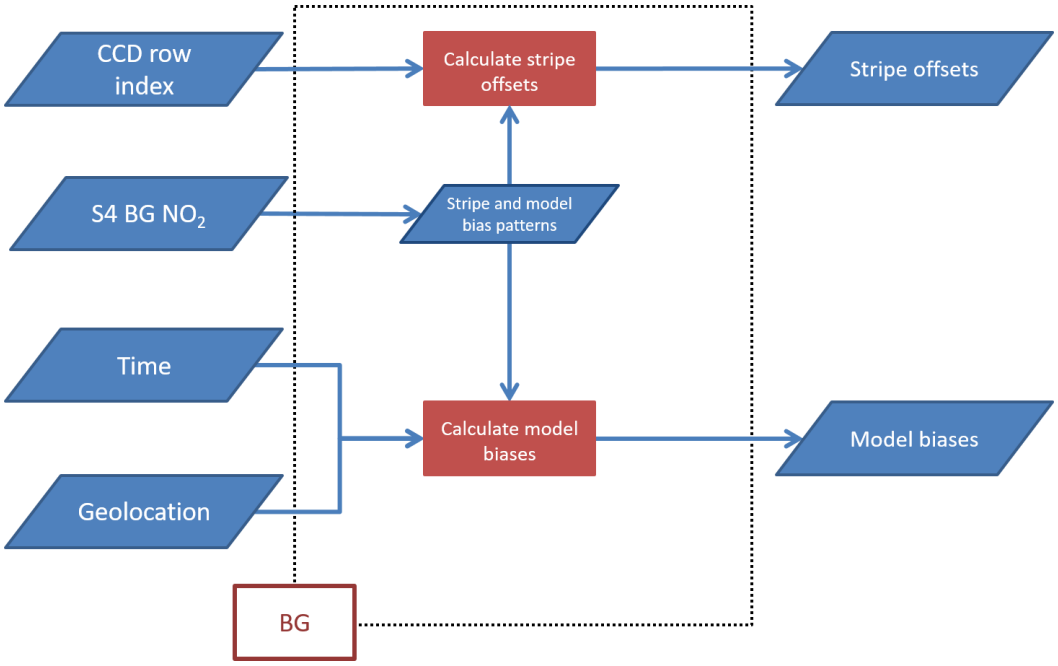

Figure 5.6. Calculation of stripe offset and model bias corrections in the BG algorithm module. See also the caption of Figure 5.1.

5.4.2 Pixel selection

Pixels are selected for the analysis of stripe and model bias patterns when the tropospheric contribution to the slant column is small and / or clouds shield the troposphere from the satellite. Selection rules are as follows:

1. For example: Retrieved tropospheric slant column is below threshold AND retrieved tropospheric vertical column is below threshold AND modelled tropospheric vertical column is below threshold.
2. Product of cloud fraction and cloud albedo is above threshold AND cloud pressure is below threshold.
3. Error on fitted slant column is below threshold.
4. Solar and viewing zenith angles are below threshold.

Pixels are then selected when (rule 1 OR rule 2) AND rule 3 AND rule 4.

The filtering procedure defines thresholds for these selection rules. Thresholds will be based on the expected distribution of NO_2 over Europe and on experiences from stratospheric correction approaches such as by Beirle et al. (2016).

5.4.3 Stripe offsets

Fitted slant columns may need to be corrected for so-called stripe offsets before they can be further processed. Small errors in sun-normalized radiance spectra that vary quasi-randomly between the different rows of the CCD but are relatively constant in time can result in systematic column density offsets that show up in maps as a characteristic striping pattern overlaid on top of the geophysical variation of NO_2 columns. Striping effects are characteristic for imaging spectrometers that use a two-dimensional detector instead of a linear detector with across-track scanning (for the latter, the same effect leads to constant across-track offsets, which are more difficult to detect). For polar-orbiting satellites, such as OMI and S5P, stripes run in the meridional direction, while the striping pattern for S4 would run in the zonal direction.

Several instrument effects could cause such a striping pattern. If the signal-to-noise ratio of the irradiance measurement is of the same order of magnitude as the signal-to-noise ratio of the radiance measurement, the noise error in the daily irradiance measurement constitutes a systematic error contribution to the corresponding sun-normalized radiance. Since an irradiance measurement is performed for every row of the detector, a striping pattern results that changes each time a new irradiance measurement is made. Such was the case in early stages of the OMI NO_2 retrievals. Measures were taken to improve the radiometric calibration of the measured irradiance spectrum after which striping patterns have become more persistent in time. Potential causes of persistent striping effects are non-uniformities in CCD pixel responses or significant dark currents that are not sufficiently well characterised during on-ground calibration. Changes in striping as well as transient stripes can result from radiation damage of the CCD, either temporarily or permanently.

Various de-striping procedures have been developed for OMI based on the general observation that the across-track direction corresponds to the zonal direction so that total vertical columns over clean regions should approximately be constant across the swath (ignoring the small differences in local time). Averaging applied to a set of uncorrected column values provides the presumably unperturbed background and across-track biases are basically calculated as the deviations from this average (Boersma et al., 2011). The underlying assumption is that the slant column offset is additive, independent of the observation geometry and scene (surface albedo, cloud cover, etc.), constant over some time (e.g. a week) and zero on average. This approach cannot be simply transferred to S4, as the across-track direction corresponds to the meridional direction and across-track variation over clean regions due to calibration errors is confounded with the (presumably smoother) variation due to the changing solar zenith angle and photochemistry. This implies that high-pass filtering needs to be applied in the meridional direction. In addition, large unpolluted regions that are in the field of view the entire day and for all relevant latitudes cannot be easily identified for S4.

Therefore, the following approach is taken for de-striping of S4 NO_2 columns. The baseline uses the CAMS model forecasts to provide the background values against which across-track biases are calculated. We assume additive slant column offsets that only depend on the across-track pixel index. Additive offset corrections are determined from fitted slant columns over clean pixels and perhaps also cloudy pixels with low but not very low cloud pressure. (Boundary layer NO_2 is shielded from the observation in pixels with high cloud fraction and low cloud pressure, although lightning NO_x and pollution transported upwards may still contribute to the tropospheric slant column.) The time period for this analysis, which is determined by the weights with which the update is calculated, will be optimized based on the temporal variability of actual striping patterns and may eventually cover observations from the past day, the past few days or even the last few weeks.

Denoting the across-track pixel index by y, which assumes 551 discrete values, we write

$$\begin{aligned} N_s^{fit}(t,\delta_{geo},\vartheta_{geo},y) \\ &= M(t,\delta_{geo},\vartheta_{geo})\left(N_v^{model}(t,\delta_{geo},\vartheta_{geo}) - c(t,\delta_{geo},\vartheta_{geo})\right) \\ &+ A(y) \\ &= M(t,\delta_{geo},\vartheta_{geo})N_v^{model}(t,\delta_{geo},\vartheta_{geo}) + A^*(t,\delta_{geo},\vartheta_{geo},y) \end{aligned} \qquad \text{5-27,}$$

where $c(t,\delta_{geo},\vartheta_{geo})$ is a presumably additive bias in the model forecast N_v^{model}, $A(y)$ is the striping offset, and $A^*(t,\delta_{geo},\vartheta_{geo},y) = -c(t,\delta_{geo},\vartheta_{geo})\cdot M(t,\delta_{geo},\vartheta_{geo}) + A(y)$ is the sum of the two. The model bias c, which excludes striping offsets, is assumed to be a smooth function of time and geolocation, because only pixels for which the total column is dominated by the stratospheric contribution are considered. Instead of explicitly parameterizing the model bias as a function of time and geolocation, filtering techniques may be applied to $A^*(t,\delta_{geo},\vartheta_{geo},y) = N_s^{fit}(t,\delta_{geo},\vartheta_{geo},y) - M(t,\delta_{geo},\vartheta_{geo})N_v^{model}(t,\delta_{geo},\vartheta_{geo})$ to extract the high-frequency stripe component $A(y)$ (high-pass filter). This needs to be further investigated.

As the simplest approach, calculating an average A^* per CCD row across many times and geolocations may already remove most of the model bias c. The incremental striping pattern could then be determined by subtracting a smoothed version of the averages

$$A(y) = \bar{A}^*(y) - \sum_{y-s}^{y+s}\frac{\bar{A}^*(y')}{2s+1} \qquad \text{5-28,}$$

where the width of the smoothing window $(2s+1)$ will have to be determined on real dS4 data. Subtracting a polynomial, of fitting Fourier terms may also be considered. Stripe offsets for rows at the edges of the CCD can have reduced trueness.

Finally, the previous striping pattern is updated with the incremental striping pattern. The striping pattern $A(y)$ resulting from this analysis (an offset value for each CCD row) is stored in the BG engineering product file and used for de-striping fitted slant columns during the coming day. The actual de-striping takes place in the STRAT module (Section 5.3).

We note here that the MTG-S platform will perform a yaw flip twice per year to avoid exposure of the cold side of the satellite, on which the radiation coolers are mounted, to direct solar irradiation. This will rotate the CCD detectors by 180° with respect to the Earth but it also changes the timing of the irradiance measurement (alternates between sunrise and sunset). Sudden changes in striping patterns following such a yaw flip may be a starting point for further investigations into the cause of striping patterns.

5.4.4 Model biases

Additional bias corrections may need to be applied to the forecast NO_2 distributions to bring the model fields in agreement with the S4 observations. De-striped S4 slant columns over clean and cloudy regions are compared with the corresponding uncorrected forecasts, the differences are analysed and bias correction patterns are derived for S4's entire geographic coverage area. Bias corrections probably need to be parameterized as a function of for example latitude, solar zenith angle, local time, etc., but the exact dependencies can only be investigated with actual S4 data. Note that even small model biases are important to remove because the resulting bias in the tropospheric vertical column is the bias in the stratospheric vertical column multiplied by the ratio M^{strat}/M^{trop}, which is typically larger than one (amplification of the model bias)

For now, we assume that biases depend on local solar time t_{sol} and latitude δ_{geo} and that they do so smoothly. The local solar time can be easily calculated from the UTC time and the longitude. After de-striping, Equation 5-27 becomes

$$N_s(t, \delta_{geo}, \vartheta_{geo}) = M(t, \delta_{geo}, \vartheta_{geo}) \left(N_v^{model}(t, \delta_{geo}, \vartheta_{geo}) - c(t_{sol}, \delta_{geo}) \right) \qquad 5\text{-}29,$$

where we assume that model biases are additive. Furthermore, we anticipate that the solar time and latitude dependencies are not necessarily orthogonal. We then calculate the difference $N_v^{model}(t, \delta_{geo}, \vartheta_{geo}) - N_s(t, \delta_{geo}, \vartheta_{geo})/M(t, \delta_{geo}, \vartheta_{geo})$ for the selected pixels and fit a low-order bivariate polynomial in solar time and latitude to this field. The low-order polynomial acts as a low-pass filter to avoid artefacts due to, for example, unfiltered pollution hotspots.

Model bias patterns can be stored in the BG engineering product in the form of the polynomial coefficients but it is more practical from a processing point of view to store actual bias corrections on a regular latitude-solar time grid with a sufficiently fine spacing (e.g. steps of 5° and 1 h). Thus, today's incremental bias field is calculated from the fitted polynomial on this grid. The bias terms from the previous BG file are updated with these incremental bias patterns and the result is written to the current BG file and used for model bias corrections on the coming day. The bias corrections are applied to the stratospheric profile forecasts from ECAused for the stratospheric correction.

The L1b product reports nominal pixel geolocations and terrain-corrected, PSF-weighted average geolocations. For the purposes of the de-biasing described in this section, the nominal pixel geolocations are sufficient.

Finally, we remark that it would be interesting for further study to inter-compare S4 columns, model columns and S5(P) columns for the time of overpass of the polar orbiting satellite from which the observations are assimilated. CAMS uses a 4D-Var scheme, which means that observations and model are compared at the same time (assimilation time equals observation time to within a small model time step) so that this comparison may give further insight particularly into the contribution of inter-instrument offsets.

5.5 Calculation of air mass factors (AMF)

5.5.1 Background

This module basically provides the calculations of photon path distributions that are needed to convert the number of absorbing molecules along photon paths to the sensor into the number of absorbing molecules in a vertical atmospheric column. At its heart are either look-up tables of so-called box air mass factors (BAMFs), which are pre-calculated with a radiative transfer model, or a radiative transfer model which can be run online. The slant column densities are assumed to be proportional to vertical column densities regardless of their magnitude and the proportionality factor is the (column) air mass factor. The air mass factor is calculated in turn from the box air mass factors.

Denoting the sun-normalized radiance by I_n, we generalize Equation 5-6 by removing the two assumptions made at that point in the text. First, the absorption cross-sections can depend on height (e.g. due to the temperature), as is the case in real atmospheres. Second, absorption by the trace gases is not necessarily weak, in which case the slant column densities no longer depend smoothly on wavelength. Because the absorption cross-sections now change along a photon path, we use for convenience the concept of slant optical thickness τ_s, which is derived from the optical thickness along photon paths to the sensor in much the same way as the slant column density (not further explained), and write

$$\ln\big(I_n(\lambda)\big) = \ln\big(I_n^{sca}(\lambda)\big) - \sum_j \tau_{s,j}(\lambda) \qquad \text{5-30.}$$

We can now introduce the altitude-resolved air mass factor (for the target species) by making the following linearization of Equation 5-30

$$\begin{aligned}\ln\big(I_n(\lambda)\big) = \ln\big(I_n^{sca}(\lambda)\big) - \tau_{s,1}^0(\lambda) \\ - \int m_1(z,\lambda)\Big(k_1(z,\lambda) - k_1^0(z,\lambda)\Big)\,dz - \tau_{s,2}(\lambda) - \cdots\end{aligned} \qquad \text{5-31,}$$

where the linearization point is denoted by the superscript 0, the absorption coefficient $k_1(z,\lambda) = n_1(z)\cdot\sigma_1(z,\lambda)$, the target absorber's number concentration at altitude z is $n_1(z)$, and finally the altitude-resolved air mass factor $m(z,\lambda)$ is given by

$$m(z,\lambda) = -\frac{\partial^2 \ln\big(I_n(\lambda)\big)}{\partial k(z,\lambda)\partial z} = -\frac{\partial^2 \ln\big(I_n(\lambda)\big)}{\sigma(z,\lambda)\partial n(z)\partial z} \qquad \text{5-32.}$$

The altitude-resolved air mass factor is the relative reduction in sun-normalized radiance for a small change of the absorption coefficient from k to $k+dk$ in a thin layer between z and $z+dz$. It depends on the observation geometry, and on the scattering, reflection and absorption properties of the atmosphere-surface system around which the linearization is made.

Following a similar logic as in Section 5.2.1, we assume that the slant absorption optical thickness of the target trace gas is small. The linearization point for the air mass factor in Equation 5-31 can then be taken to be at no absorption at all ($\tau_{s,1}^0(\lambda) = 0$) and we get

$$\ln\big(I_n(\lambda)\big) = \ln\big(I_n^{sca}(\lambda)\big) - \int m_1(z,\lambda) n_1(z) \sigma_1(z,\lambda) dz - \tau_{s,2}(\lambda) - \cdots \qquad 5\text{-}33.$$

In a quantitative sense, we can say that the assumption of weak absorption is valid when the error introduced by the linearization around $\tau_{s,1}^0(\lambda) = 0$ is small compared to the measurement noise for the range of slant absorption optical thicknesses encountered in the atmosphere and the observation conditions of the satellite instrument. When in addition the slant absorption optical thicknesses of the interfering species are also small, the air mass factor $m_1(z,\lambda)$ becomes at most smoothly wavelength dependent.

In Section 5.2.1 we have assumed an isothermal atmosphere so that the absorption cross-sections were independent of height. However, in real atmospheres, the temperature varies with height and so does the NO_2 absorption cross-section. Comparing Equation 5-33 with Equation 5-6, we see that we have to distinguish between the altitude-resolved absorption cross-section $\sigma(z,\lambda)$ and some altitude-independent absorption cross-section $\sigma(\lambda)$ that is used in the slant column fit. The altitude-independent absorption cross-section can, for example, be calculated as the NO_2 cross-section appropriately averaged over altitude for a given temperature profile and a priori NO_2 profile (not shown). Alternatively, one can simply use the absorption cross-section at a particular reference temperature, which is what we do here. Fitted slant column densities thus hold for the altitude-independent absorption cross-section $\sigma(\lambda)$ used in the DOAS fit. Equation 5-32 can now be rewritten in terms of slant column densities as

$$m(z,\lambda) = \frac{\sigma\big(T_{ref},\lambda\big)}{\sigma(T(z),\lambda)} \cdot \frac{\partial^2 N_s(\lambda)}{\partial n(z) \partial z} \qquad 5\text{-}34,$$

where the factor in front of the derivative corrects for the difference in absorption cross-section between the reference temperature and the actual temperature at altitude z. Since the derivative is calculated at no absorption by the target species, we can also write

$$m(z,\lambda) = \frac{\sigma\big(T_{ref},\lambda\big)}{\sigma(T(z),\lambda)} \cdot \frac{\partial N_s(\lambda)}{n(z) \partial z} \qquad 5\text{-}35.$$

It can now be seen that the slant column density is indeed proportional to the vertical column density. The proportionality factor is called the column air mass factor or simply air mass factor $M(\lambda)$. Rewriting Equation 5-35 we get

$$M(\lambda) = \frac{N_s(\lambda)}{N_v} = \frac{\int m(z,\lambda) n(z) \dfrac{\sigma(T(z),\lambda)}{\sigma\big(T_{ref},\lambda\big)} dz}{\int n(z) dz} \qquad 5\text{-}36.$$

The column air mass factor does depend on the NO_2 profile, or more precisely, on the profile shape. To complete we write the DOAS equation as

$$\ln\big(I_n(\lambda)\big) = \ln\big(I_n^{sca}(\lambda)\big) - M_1(\lambda) \cdot N_{v,1} \cdot \sigma_1\big(T_{ref},\lambda\big) - N_{s,2} \cdot \sigma_2\big(T_{ref},\lambda\big) - \cdots \qquad 5\text{-}37.$$

In Section 5.2.1 we used measured spectra rather than monochromatic ones and we replaced the smooth background reflectance by a fitted polynomial. Doing so here does not change the equations derived above, provided that the air mass factor and absorption cross-section scaling factor are constant across the integration range of the instrument spectral response function and the absorption cross-sections themselves are appropriately convolved with the response functions as described earlier. Finally, although we have so far allowed the air mass factor to depend smoothly on wavelength, in practical DOAS applications the air mass factor is usually assumed to be wavelength independent, which is also what we do here (but see next section).

In terms of finite differences, the altitude-resolved air mass factor in Equation 5-35 becomes

$$m_l = \frac{1}{c_l^T} \cdot \frac{\Delta N_s}{N_{v,l}} \quad \text{5-38,}$$

where the subscript l is the index of the atmospheric layer, air mass factors and slant columns are taken to be constant with wavelength now, a temperature correction factor c_l^T has been introduced and $N_{v,l}$ denotes the partial vertical column of layer l. The partial vertical column of layer l ($N_{v,l}$) should not to be confused with the total vertical column of species i ($N_{v,i}$): the difference will be clear from the context. The terms altitude-resolved air mass factor and box air mass factor are used interchangeably in this document, although the latter is perhaps more appropriate for the altitude-resolved air mass factor in terms of finite differences. Thus, the box air mass factor is the contribution of the partial vertical column $N_{v,l}$ of layer l to the slant column density. The temperature correction factor will be discussed in Section 5.5.11. In terms of finite differences, Equation 5-36 reads

$$M = \frac{\sum_l m_l \cdot N_{v,l} \cdot c_l^T}{\sum_l N_{v,l}} \quad \text{5-39.}$$

For the S4 NO_2 retrieval algorithm, a priori profiles are provided by a model with a large number of vertical layers. We now assume that the altitude-resolved air mass factor within such a model layer is constant so that there is no need to calculate a layer-integrated air mass factor (see in this respect for example the discussion of weighting function DOAS in Rozanov and Rozanov (2010)). We can then let the vertical discretization of the atmosphere in Equations 5-38 and 5-39 coincide with the model layers of the a priori profile. For the box air mass factor of model layer l we simply use the altitude-resolved air mass factor at the midpoint of the layer. The same holds for the temperature correction for model layer l, which is calculated from the temperature at the layer's midpoint.

Separate air mass factors for the troposphere and stratosphere can be calculated by only summing over atmospheric layers below or above the tropopause, respectively. For completeness, we write this out once as

$$M = \frac{\sum_{l=l_{toa}}^{l_{boa}} m_l^* \cdot N_{v,l}}{\sum_{l=l_{toa}}^{l_{boa}} N_{v,l}} \text{ and } N_v = {}^{N_s}/_{M} \quad \text{5-40,}$$

$$M^{strat} = \frac{\sum_{l=l_{toa}}^{l_{tp}-1} m_l^* \cdot N_{v,l}}{\sum_{l=l_{toa}}^{l_{tp}-1} N_{v,l}} \text{ and } N_v^{strat} = {}^{N_s^{strat}}/_{M^{strat}} \quad \text{5-41,}$$

and

$$M^{trop} = \frac{\sum_{l=l_{tp}}^{l_{boa}} m_l^* \cdot N_{v,l}}{\sum_{l=l_{tp}}^{l_{boa}} N_{v,l}} \text{ and } N_v^{trop} = {}^{N_s^{trop}}\Big/_{M^{trop}} \quad \text{5-42.}$$

The temperature correction factor has been included in the box air mass factor, which is indicated by the asterisk.

Calculation of box air mass factors for the particular observation geometry and state of the atmosphere-surface system is described in detail in the following sections. A flow diagram of the AMF module is given in Figure 5.7. The module's main output fields are stratospheric and tropospheric air mass factors, bias-corrected stratospheric vertical column forecasts and averaging kernels. Stratospheric air mass factors are needed by the STRAT module for the separation of slant columns into a stratospheric and a tropospheric part. The final conversion of tropospheric slant columns to tropospheric vertical columns also takes place in the STRAT module, for which tropospheric air mass factors are needed. Model bias corrections are applied to the stratospheric part of the NO_2 profile forecasts in the AMF module. The stratospheric partial column is then passed on to the STRAT module. This ensures that the profile shapes used for the air mass factor calculations and the stratospheric vertical columns used in the stratospheric correction step are consistent. Column air mass factors are calculated from box air mass factors that are in turn read from look-up tables. These look-up tables store box air mass factors as a function of the observation geometry, surface pressure and surface reflectance or cloud pressure and cloud albedo. The relevant parameters are read from the S4 L2 Cloud and S4 GSR products but a submodule of the AMF module re-calculates the relevant cloud parameters for the NO_2 fit window from values reported in the Cloud product.

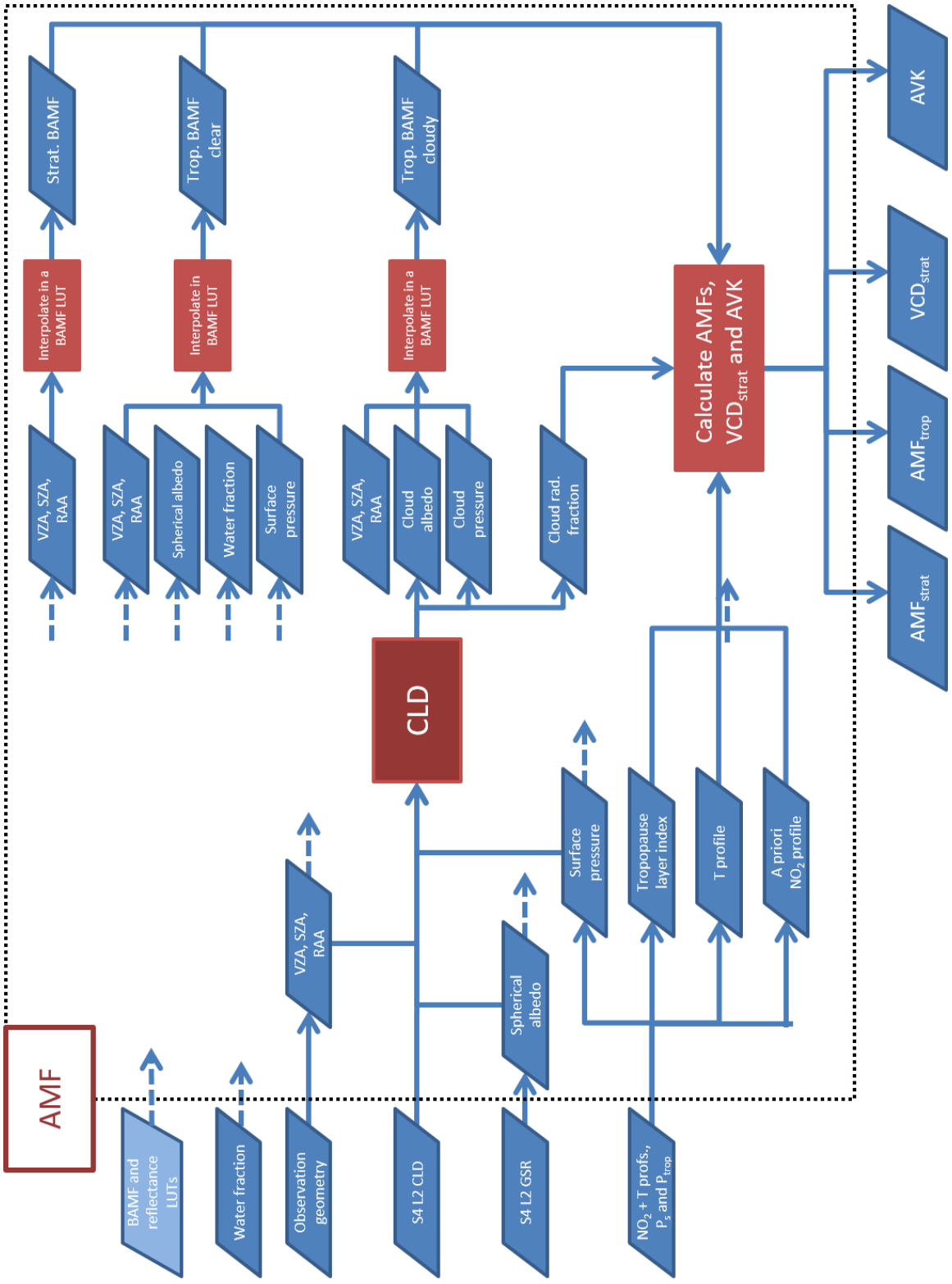

Figure 5.7. The structure of the AMF algorithm module with its most important data fields. See also the caption of Figure 5.1. The CLD submodule calculates the relevant cloud parameters for the NO_2 fit window. This submodule is detailed out in Figure 5.9.

5.5.2 Air mass factor for the fit window

Based on the previous discussion, we slightly reformulate Equation 5-37 for measured spectra as

$$\ln\left(\frac{\tilde{I}(\lambda_i)}{\tilde{E}_0(\lambda_i)}\right) = \sum_{p=0}^{4} c_p \lambda_i^p - M_1(\lambda_i) \cdot N_{v,1} \cdot \tilde{\sigma}_1(T_{ref}, \lambda_i) - \sum_{j=2}^{\cdots} N_{s,j}(\lambda_i) \cdot \tilde{\sigma}_j(T_{ref}, \lambda_i) \qquad 5\text{-}43.$$

We repeat the assumption that the slant absorption thicknesses of all species are small such that the air mass factors or slant columns are at most smoothly wavelength dependent. In addition, we recall that the air mass factor includes the scaling factor between the actual cross-section at altitude z and the reference absorption cross-section used in the slant column fit.

In the DOAS fit, all slant columns are assumed to be constant with wavelength across the fit window so that they can be fitted. We now reformulate Equation 5-14 as

$$\ln\left(\frac{\tilde{I}(\lambda_i)}{\tilde{E}_0(\lambda_i)}\right) = \sum_{p=0}^{4} c_p \lambda_i^p - M_1 \cdot N_{v,1} \cdot \tilde{\sigma}_1(T_{ref}, \lambda_i) - \sum_{j=2}^{\cdots} N_{s,j} \cdot \tilde{\sigma}_j(T_{ref}, \lambda_i) + \epsilon_\lambda(\lambda_i) \qquad 5\text{-}44,$$

where the wavelength dependence has been dropped. The error (ϵ_λ) introduced by the assumption of wavelength independent slant columns is explicitly indicated; all other errors are ignored. It should be noted that polynomial coefficients in the two equations above can be (slightly) different.

The air mass factors / slant columns for the fit window are the air mass factors / slant columns that minimize the error ϵ_λ. As the DOAS equation is solved in a non-weighted least-squares fit, this error should be minimised in a least-squares sense as well. We explore this a bit more, because it is instructive. For convenience of notation, we replace every slant column by the product of air mass factor and corresponding vertical column. The cost function reads

$$\chi^2 = \sum_i \left(\epsilon_\lambda(\lambda_i)\right)^2 = \sum_i \left[\sum_j \left(M_j - M_j(\lambda_i)\right) \cdot N_{v,j} \cdot \tilde{\sigma}_j(T_{ref}, \lambda_i) + \sum_{p=0}^{4} c_p \lambda_i^p\right]^2 \qquad 5\text{-}45,$$

where again the polynomial coefficients are different. The cost function should be minimised as a function of the air mass factors M_j and the polynomial coefficients c_p. Differentiating χ^2 with respect to these parameters and setting the derivatives to zero gives a linear system of equations, which can be readily inverted in standard ways.

For the moment, we assume that the difference polynomial in Equation 5-45 is close to zero, which is reasonable. The derivative with respect to the air mass factor of species k is then given by

$$\frac{\partial \chi^2}{\partial M_k} = \sum_i 2 \cdot \left[\sum_j \left(M_j - M_j(\lambda_i)\right) \cdot N_{v,j} \cdot \tilde{\sigma}_j(T_{ref}, \lambda_i)\right] \cdot N_{v,k} \cdot \tilde{\sigma}_k(T_{ref}, \lambda_i) \qquad 5\text{-}46.$$

Setting this derivative to zero we find after some rearrangement of terms that the following equation should hold for every k

$$\sum_j M_j \cdot N_{v,j} \sum_i \tilde{\sigma}_j(T_{ref}, \lambda_i) \cdot \tilde{\sigma}_k(T_{ref}, \lambda_i) = \sum_j N_{v,j} \sum_i M_j(\lambda_i) \cdot \tilde{\sigma}_j(T_{ref}, \lambda_i) \cdot \tilde{\sigma}_k(T_{ref}, \lambda_i) \qquad 5\text{-}47.$$

This shows that the air mass factor for the fit window of one trace gas in principle depends on the total amount of the other trace gases. This dependence disappears when the absorption cross-sections are orthogonal. In that case, the summation over i on the left-hand side is zero for species other than k (by assumption: it is the dot product) and the summation over i on the right-hand side is approximately zero for species other than k (the air mass factor is spectrally smooth). In this case, we get for the air mass factor of the fit window

$$M_k = \frac{\sum_i M_k(\lambda_i) \cdot \left(\tilde{\sigma}_k\left(T_{ref}, \lambda_i\right)\right)^2}{\sum_i \left(\tilde{\sigma}_k\left(T_{ref}, \lambda_i\right)\right)^2} \qquad \text{5-48.}$$

When the absorption cross-sections are orthogonal, the air mass factor for the fit window is a weighted average of the spectral air mass factor where the spectral weight is the square of the absorption cross-section.

For practical applications, the discussion above has the following implications. One way to proceed would be to calculate and store altitude-resolved air mass factors at several wavelengths across the fit window so that for each pixel the appropriate air mass factor for the fit window can be determined according to Equation 5-48. As the air mass factors are spectrally smooth, only a few wavelengths are needed (subsequent interpolation gives air mass factors at all other wavelengths λ_i), but the look-up tables would still increase significantly in size. A more convenient approach would perhaps be to calculate air mass factors at some optimal wavelength, where optimal is defined as follows. For a representative ensemble of geophysical scenarios, air mass factors for the fit window are calculated in the exact way (Equation 5-46) and compared with spectral air mass factors. The optimal wavelength λ_{ref} is that wavelength for which the difference between the two air mass factors is smallest over the entire ensemble (e.g. [RD07]). From experience, we know that the NO_2 fit window's central wavelength is an optimal wavelength for the calculation of the box air mass factor. Finally, we mention that more sophisticated approaches exist that account for the wavelength dependence of the air mass factor by constructing additional pseudo-absorbers (Puķīte et al., 2010).

5.5.3 Radiative transfer modelling

Apart from a minus sign, the altitude-resolved air mass factor of a trace gas (Equation 5-32) equals the functional derivative of the logarithm of the intensity with respect to the trace gas's absorption coefficient (e.g. Rozanov and Rozanov, 2010). Altitude-resolved air mass factors are calculated with the radiative transfer model SCIATRAN (Rozanov et al., 2014). They are derived from weighting functions of the intensity with respect to the number density profile. Weighting functions are in turn determined using the forward–adjoint technique (Rozanov and Rozanov, 2007). To solve for the intensity and its derivatives, the vertically inhomogeneous atmosphere is discretized in homogeneous layers. Weighting functions give the variation of the intensity dI due to a perturbation of the number density dn_k in layer k having geometric thickness Δz_k, which results in a change of the vertical column by an amount $dn_k \cdot \Delta z_k$. Basically, the box air mass factor at a particular altitude level z_k is then calculated as (a few technical details are omitted)

$$m(z_k, \lambda) = -\frac{W_{n_k}(\lambda)}{I(\lambda) \cdot \Delta z_k \cdot \sigma_k(\lambda)} \qquad \text{5-49,}$$

where $W_{n_k} = \partial I / \partial n_k$ is the weighting function of the number density, σ_k is the absorption cross-section in layer k, and z_k is taken at the geometric midpoint of the layer. Details can be found in the references mentioned above.

The most important settings for the radiative transfer calculations are as follows.

- Box air mass factors are calculated at 461 nm, which is the middle of the fit window. As the tropospheric AMF of NO_2 changes nearly linearly across the fitting window and the amplitude of the NO_2 absorption cross-section is quite constant (Figure 5.3), using the middle of this range is a good choice.
- The sphericity of the atmosphere is accounted for as follows. The calculation of the single-scattering source function and the subsequent integration of the single-scattering and multiple-scattering source functions along the line-of-sight are all performed in a spherical-shell geometry. The multiple-scattering source function is approximated by the multiple-scattering source function in the pseudo-spherical approximation for the appropriate local solar zenith angle. The Earth's radius is set to 6371 km.
- Atmospheric refraction is taken into account for the incoming direct beam at altitudes below 35 km and local solar zenith angles above 70° and for the entire line-of-sight.
- Polarization effects of atmospheric scattering are taken into account, but inelastic scattering effects are not included in the box air mass factor calculations (although rotational Raman scattering is treated through the Ring cross-section in the DOAS fit).
- The pressure and temperature profile correspond to the US Standard Atmosphere. The dependence on the pressure profile through Rayleigh scattering is however very small. The sea level pressure (altitude of 0 km) is 1013 hPa. Box air mass factors are calculated for several other surface altitudes as well.
- The a priori NO_2 profile corresponds to the US Standard Atmosphere. Although the linearization point in Equations 5-33 and 5-37 is at zero absorption, the altitude-resolved air mass factor is calculated with SCIATRAN at this non-zero a priori profile. When the assumption of weak absorption and thus the linearization are valid, derivatives for the two linearization points should however be the same.
- The interfering absorbers currently included in the radiative transfer calculations are O_3 and O_4. The a priori O_3 profile is also taken from the US Standard Atmosphere. The dependence on the O_3 profile is small because ozone can be considered a weak absorber in the NO_2 fit window.
- Clouds are modelled as Lambertian surfaces at a certain height with a certain albedo.
- Aerosols can in principle be included in the calculation of box air mass factors, but this is currently not done. In SCIATRAN, it is possible to independently specify profiles of the aerosol absorption and scattering coefficients as a function of wavelength. The wavelength dependent aerosol scattering matrix can be prescribed in several discrete altitude ranges.
- Treatment of surface reflectance depends on whether airmass factors are read from a LUT (baseline) or calculated online (future development).

  - In the case of LUT, Lambertian surface reflectance is assumed and tabulated.

  - If AMFs are calculated online, the same directional surface reflectance models as assumed in the S4 L2 SUR retrieval algorithm can be used for the calculation of box air mass factors. Thus, the Ross-Li model describes the reflectance of land surfaces, while Fresnel reflection with a model for surface roughness describes the reflectance of water surfaces.

  For land surfaces described by the Ross-Li model, the incident radiation is completely depolarized upon reflection, i.e. only the *(1,1)*-element of the reflection matrix is non-zero. For water surfaces, the BRF term describing Fresnel reflection by the wind-roughened water surface (see below) accounts for polarization. i.e. the full Müller matrix representation is constructed and used in the radiative transfer calculations.

5.5.4 Directional surface reflectance

5.5.4.1 Surface BRF

Directional surface reflectance is described by the BRF models used in the S4 L2 SUR algorithm and we will briefly discuss this point now. The S4 L2 SUR algorithm and product and the derived S4 L2 GSR support product are described in detail in [RD06]. We will start with a brief explanation of the difference between the Bidirectional Reflectance Distribution Function (BRDF) and the Bidirectional Reflectance Factor (BRF).

The boundary condition for the radiation field at the bottom of the atmosphere can be written as

$$\mathbf{I}^{+}(\mu,\varphi;\lambda) = \frac{1}{\pi}\int_0^{2\pi}\int_0^{1} \boldsymbol{\rho_s}(\mu,\varphi;\mu',\varphi';\lambda)\cdot\mathbf{I}^{-}(-\mu',\varphi';\lambda)\mu' d\mu' d\varphi' \qquad \text{5-50.}$$

Here, $\mathbf{I}$ is the Stokes vector of the incoming or reflected light and $\boldsymbol{\rho_s}$ is in principle a 4 x 4 matrix describing the reflection properties of the ground surface. The SUR documentation refers to matrix $\boldsymbol{\rho_s}$ as the Bidirectional Reflectance Factor and to matrix $\boldsymbol{\rho_s}/\pi$ as the Bidirectional Reflectance Distribution Function. This is the convention that we will also adopt in this document. (But note that matrix $\boldsymbol{\rho_s}$ can go by different names: in the SCIATRAN technical literature, it is in fact this matrix that is called the Bidirectional Reflectance Distribution Function, see equation 93 in Rozanov et al., 2014.) In a general sense, a surface's BRF is defined as the BRDF of that surface divided by the (1,1)-element of the BRDF of an ideal Lambertian surface (e.g. Schaepman-Strub et al., 2006). With this definition, the BRF is a convenient quantity because it is independent of the normalization constant before the integral in Equation 5-50. In case of a Lambertian surface, the (1,1)-element of the BRF matrix $\boldsymbol{\rho_s}$ is independent of the angles of reflection and of the angles of incidence (e.g. Thomas and Stamnes, 2002) while all other elements of the matrix are zero (reflected light is depolarized). Furthermore, the (1,1)-element of BRF matrix $\boldsymbol{\rho_s}$ in Equation 5-50 for a Lambertian surface is precisely that surface's albedo (ratio of reflected to incident flux). The surface is ideal when all incident light is reflected, hence when its albedo is one. Finally, often the term BRF is used to refer only to the (1,1)-element of the BRF matrix, but this will be clear from the context – we will use the symbol ρ_s in that case. Indeed, the SUR algorithm provides just the (1,1)-element in a parameterized form.

The SUR core algorithm performs a simultaneous retrieval of directional surface reflectance and aerosol optical thickness based on a multi-pixel inversion with a priori constraints on the temporal and spatial variability of surface and aerosol properties. In principle, directional surface reflectance and aerosol optical thickness are retrieved for every hour of the day. Results are reported on a static L1c pixel grid, which may differ from the variable L1b pixel grid. The L1c grid is basically the L1b pixel grid when the satellite is at its nominal position of 0º longitude and 0º latitude and the platform has its nominal orientation. The S4 L2 SUR processor runs once a day during the night when all measurements of the past day have been collected. Thus, a new product file is available at the start of every day and contains retrieval parameters based on measurements up to and including the past day. For a successful retrieval, a sufficient number of pixels in a tile of pixels have to be cloud-free, which is often not the case. Therefore, the GSR support product is derived from the S4 L2 SUR core product. The S4 L2 GSR product provides a gap-filled daily map of BRF model coefficients. Pixels in the L1c grid for which there are no updated values of BRF model coefficients are filled with values from the previous day. It is expected that the average lifetime of a GSR L1c pixel value is … days. The GSR product is the data product from which we read BRF coefficients.

5.5.4.2 Land BRF model

The BRF for land surfaces is described as a linear combination of three so-called scattering kernels: the isotropic, volumetric and geometric-optical kernel. For the volumetric kernel f_{vol} the Ross-thick model with hotspot correction is used and for the geometric-optical kernel f_{geo} the Li-sparse model. The BRF has three free parameters k, k_{vol} and k_{geo} and is written in [RD06] as

$$\rho_s(\mu, \varphi; \mu', \varphi'; \lambda) = k(\lambda) \cdot \left(1 + k_{vol} \cdot f_{vol}(\mu, \mu', \varphi - \varphi') + k_{geo} \cdot f_{geo}(\mu, \mu', \varphi - \varphi')\right) \quad \text{5-51,}$$

where only coefficient k is wavelength dependent. Exact expressions for the volumetric and geometric-optical kernels as implemented by the SUR algorithm can be found in section 5.4.2 of [RD06]. The same equations are also implemented in SCIATRAN for the box air mass factor calculations. Note that the volumetric and geometric-optical kernels are normalized such that when the sun and the observer are at zenith we have $f_{geo}(\mu = 1, \mu' = 1, \varphi - \varphi') = 0$ and $f_{vol}(\mu = 1, \mu' = 1, \varphi - \varphi') = {}^{\pi}/_{4} \cdot (F_{HotS} - 1)$, which is zero when there is no hotspot correction ($F_{HotS} = 1$). The GSR product provides the three coefficients k, k_{vol} and k_{geo} on the L1c grid per day. Coefficient k is given at a number of discrete wavelengths, one of them being 457 nm. We will simply read and use this value for the look-up in the table of box air mass factors calculated at 461 nm (see also section 7 of [RD06]).

For large zenith angles, the Ross-Li kernels have reduced accuracy (e.g. Litvinov et al., 2011). We use the BRF (ρ_s) as such up to zenith angles of 85° (obviously on the reference ellipsoid); above this value, the BRF is extrapolated using its value at 85°. Note that this threshold is also the cut-off zenith angle for calculation of box air mass factors and tropospheric columns.

5.5.4.3 Water BRF model

The BRF model for water surfaces is based on Fresnel reflection and accounts for sea surface roughness. It also has three free parameters, which are the root-mean-squared slope of the surface facets σ, the fraction δ_{Fr} of the pixel that is not covered by foam and contributes to Fresnel reflection, and an additional Lambertian reflectance term a_0. The BRF is written as

$$\rho_s(\mu, \varphi; \mu', \varphi'; \lambda) = \delta_{Fr} \cdot \frac{\pi}{\mu'} \cdot F_{Fr,11}(\theta_r; m) \cdot P(\tan \vartheta_n\,; 0, \sigma) \cdot f_{shad}(\mu, \mu'; \sigma) + a_0(\lambda) \quad \text{5-52.}$$

We can understand the different components as follows, see also Figure 5.8 for an illustration of the geometry. The roughened water surface is considered a collection of randomly oriented surface facets, whose orientations are characterised by the angle ϑ_n between the facet's normal $\hat{n}$ and local zenith $\hat{z}$. The slope of the surface facet, $\tan\vartheta_n$, is described by a Gaussian probability distribution P with zero mean and standard deviation σ. This distribution is, for reasons of computational efficiency, by assumption azimuthally symmetric, i.e. it is independent of the wind direction. The elements of the Fresnel reflection matrix $\mathbf{F}_{Fr}$ depend on the angle of specular reflection θ_r and on the refractive index m. (Recall that ρ_s is shorthand for the (1,1)-element of the BRF matrix, hence only the (1,1)-element of the Fresnel reflection matrix appears in Equation 5-52.) Then, given the observation geometry, the specific angle ϑ_n of the surface facet for which specular reflection occurs can be calculated, hence the probability of specular reflection P. The corresponding angle of specular reflection θ_r is determined by the observation geometry as well, hence also $F_{Fr,11}$ is known. The main point here is that θ_r and $\tan\vartheta_n$ in Equation 5-52 are known functions of $(\mu, \varphi; \mu', \varphi')$. Finally, f_{shad} is an empirical factor correcting for shadowing effects and depends on the zenith angles and the standard deviation of the wave slope distribution. Exact expressions for $F_{Fr,11}$, P and f_{shad} and values for the refractive index used can be found in section 5.4.2 of [RD06]. Given parameters σ and δ_{Fr} the remaining elements of the BRF matrix can be calculated, which are needed for the polarized radiative transfer calculations. The GSR product provides the three coefficients σ, δ_F and a_0 on the L1c grid per day. Only parameter a_0 is wavelength dependent. Again, we will simply read the value at the SUR reference wavelength of 457 nm and use this value for the box air mass factors calculated at 461 nm.

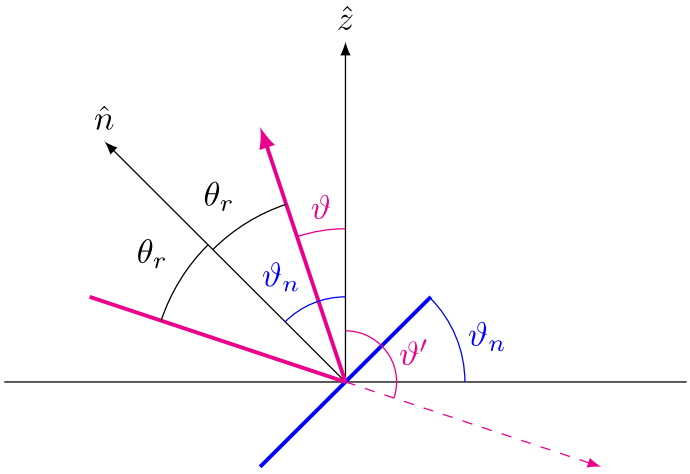

Figure 5.8. Illustration of the geometry for Fresnel reflection by the wind-roughened water surface. The light path is the thick purple line, the incident light vector the purple dashed line, and the tilted surface facet is the thick blue line. Zenith angles of the incident light vector (ϑ'), reflected light vector (ϑ) and the facet's normal vector (ϑ_n) are indicated in the figure, as well as the angle of reflection (θ_r). The geometry illustrated here is for a relative azimuth angle $\varphi - \varphi'$ of 180°, but can be easily generalised to specular reflection out of the principal plane.

5.5.4.4 Implementation in the NO_2 processor

Probably the most accurate way to proceed is to calculate air mass factors for exactly these BRF models while also including aerosol parameters from the SUR product. However, since aerosol parameter values available for the retrieval of NO_2 for a particular target pixel are at least a day old (recall that the S4 NO_2 product is delivered in near real-time), it needs to be investigated whether the aerosol parameters from the SUR product will actually improve the accuracy of the NO_2 retrieval. The fact that the SUR / GSR product is not delivered in near real-time is less problematic for the directional surface reflectance than for the aerosol optical thickness, because the temporal variability of the surface reflectance is relatively small on the time scale of a few days whereas for the aerosol optical thickness values retrieved from the same measurement are clearly preferred. As mentioned above, the use of aerosols in the AMF calculation has to be combined with cloud parameters using the same assumptions on the aerosols.

As the baseline, surface reflection is modelled as Lambertian-equivalent reflectivity derived from the dynamic map of BRF model coefficients. There are several ways to derive a Lambertian-equivalent reflectivity (explained in detail in Section 5.5.4.5). For example, when the atmosphere contains a lot of aerosols, we may calculate the spherical albedo and assign this value to the albedo of the assumed Lambertian ground surface. However, in this approach directional effects may be underestimated as the downwelling radiation at the surface is assumed more diffuse than it is in reality. Another possibility would be to derive a Lambertian-equivalent reflectivity from the top-of-atmosphere radiance calculated for a Rayleigh atmosphere and the BRF coefficients and observation geometry of the pixel under consideration.

The main reason for not using the directional surface reflectance models is the size of look-up tables. A look-up table incorporating the full BRF has two additional dimensions and requires a fine spacing of the three dimensions corresponding to the observation geometry in order to accurately describe the angular variation of the surface reflectance (e.g. in the hot spot over land or at specular reflection over water). Accurate treatment of surface BRF is therefore only possible if hardware permits online calculations of box air mass factors so that look-up tables can be avoided at all.

Before BRF parameters from the GSR product can be used in the calculation of air mass factors, a few pre-processing steps need to be performed. First, wavelength dependent BRF parameters have to be spectrally interpolated from the SUR wavelengths to the wavelength of the air mass factor. As already mentioned we assume that it is sufficient to simply use parameter values for the SUR wavelength closest to the centre of the fit window (nearest-neighbour interpolation). Second, BRF parameters have to be spatially interpolated from the L1c grid to the actual L1b pixel grid. Again, we assume that a nearest-neighbour interpolation as described in section 6.3.9 of the SUR / GSR ATBD ([RD06]) is sufficient for our purposes. Third, mixed land-water pixels (coast, inland water, etc.) have to be treated. The SUR algorithm retrieves parameters for both land and water BRF models (i.e. water model is also applied to land pixels and land model is also applied to water pixels). We will simply use the BRF model of the dominant surface type (i.e. when land fraction is larger than 0.5, declare pixel to be fully land, and vice versa).

5.5.4.5 Lambertian-equivalent reflectivities

Values of individual BRF coefficients are not easy to interpret intuitively. Therefore, we now explain how three different Lambertian-equivalent reflectivities can be derived from the directional surface reflectance models that will help interpretation of the BRF coefficients. The basic idea is that the ground surface with the directionally dependent reflectance is replaced by an isotropically reflecting (Lambertian) surface with some appropriate albedo: this albedo value is then called the Lambertian-equivalent reflectivity. The question is what this appropriate Lambertian albedo value is. We start by considering two limit cases, one for isotropic illumination and one for collimated incidence.

We have the true downward radiance field at the ground surface $I^-(-\mu', \varphi')$, the true downward flux at the surface F^- and the true BRF $\rho_s(\mu, \varphi; \mu', \varphi')$. Furthermore, from the BRF the so-called spherical albedo can be calculated by integration of the BRF over all angles, defined as

$$A_{spher}(\lambda) = \frac{1}{\pi^2}\int_0^{2\pi}\int_0^1\int_0^{2\pi}\int_0^1 \rho_s(\mu, \varphi; \mu', \varphi'; \lambda)\mu' d\mu' d\varphi' \mu d\mu d\varphi \qquad 5\text{-}53.$$

The spherical albedo is also called the bi-hemispherical reflectance for isotropic illumination (BHR_{iso}) or the white-sky albedo.

It can now be shown that the reflected flux $\hat{F}^+$ is the same in the following two situations:

- the surface with the true BRF and an isotropic downwelling radiance field $I^-_{iso} = {F^-}/{\pi}$,
- a Lambertian surface with an albedo equal to the spherical albedo and the true non-isotropic downwelling radiance field $I^-(-\mu', \varphi')$.

When the atmosphere is scattering optically thick, the downward radiance field at the surface is nearly isotropic. In this case, we replace the true ground surface by a Lambertian surface with an albedo equal to the true surface's spherical albedo. Then, the reflected flux calculated for the Lambertian surface ($\hat{F}^+$) approximates the true reflected flux (F^+). Of course, the true reflected radiance field will show some directional dependence that is lost by the Lambertian approximation, but this directional dependence will be small as the incident radiance field itself was already close to isotropic.

It can also be shown that the radiance reflected into the viewing direction $\hat{I}^+(\mu, \varphi)$ is the same in the following two situations:

- the surface with the true BRF and collimated incident radiance $I^-_{col}(-\mu', \varphi') = {F^-}/{\mu_0}\,\delta(\mu' - \mu_0)\delta(\varphi' - \varphi_0)$,
- a Lambertian surface with an albedo equal to the BRF for the direct observation geometry $\rho_s(\mu, \varphi; \mu_0, \varphi_0)$ and the true non-isotropic downward radiance field $I^-(-\mu', \varphi')$.

When the atmosphere is scattering optically thin (i.e. it is transparent), the downward radiance field at the surface will be nearly collimated. In this case, we replace the true surface by a Lambertian surface with an albedo equal to the true surface's BRF for the direct observation geometry. Then, the radiance reflected into the viewing direction calculated for the Lambertian surface ($\hat{I}^+(\mu, \varphi)$) approximates the true radiance reflected into the viewing direction ($I^+(\mu, \varphi)$). Of course, the true reflected radiance field will have components in other directions than the viewing direction that can still contribute to the radiance measured at the sensor, but these components will be small as the atmosphere is close to being transparent.

The Lambertian-equivalent reflectivities for isotropic and collimated incidence present two limit cases. We report the BRF and the spherical albedo in the output product because they provide an intuitive interpretation of the BRF coefficients, but we point out, once again, that the actual downward radiance field at the surface in the NO_2 fit window is neither isotropic nor collimated.

A third Lambertian-equivalent reflectivity can perhaps be considered an intermediate case. It is derived in two steps. First, the top-of-atmosphere radiance is calculated for a Rayleigh atmosphere and the specific BRF coefficients, observation geometry and surface pressure of the pixel under consideration. Second, the Lambertian albedo that would have resulted in the same top-of-atmosphere radiance is calculated, again for a Rayleigh atmosphere and the specific observation geometry and surface pressure of the satellite pixel. This Lambertian albedo is the BRF's third Lambertian-equivalent reflectivity. Look-up tables are needed in each of the two steps. For the first step, look-up tables store the sun-normalized radiance over land and over water surfaces at the wavelength of the box air mass factor. The independent axes of these look-up tables are the three observation angles, the three BRF coefficients and the surface pressure. Pressure and temperature profiles are the same US Standard Atmosphere profiles used in the box air mass factor calculations. Since a slice of the look-up table corresponds to Lambertian surface reflection, this table can also be used in the second step for the inverse look-up of the Lambertian albedo given the top-of-atmosphere radiance calculated in the first step.

In symbols we thus have the following three Lambertian-equivalent reflectivities:

- $A_{Lamb} = A_{spher}$,
- $A_{Lamb} = \rho_s(\mu, \varphi; \mu_0, \varphi_0)$ and
- $A_{Lamb} = A_{Lamb}^{I_{toa}}$.

It is not clear at this point whether box air mass factors calculated for a Rayleigh atmosphere bounded by a surface with directional reflectance using GSR's BRF coefficients or bounded by a Lambertian ground surface with an albedo equal to one of the LER values just discussed represent box air mass factors in the true atmosphere best. Of course, what is driving this question is an accurate modelling of photon paths reaching the sensor, rather than an accurate modelling of the top-of-atmosphere radiance. We note that whatever the assumptions concerning the atmosphere-surface system made in the box air mass factor calculations, the same assumptions should also be made in the cloud correction described in Section 5.5.9.

Finally, we mention that the concept of a LER value derived from top-of-atmosphere radiances is also used in the context of satellite LER climatologies (e.g. Kleipool et al., 2008; Tilstra et al., 2017), but there are clear differences. Here, a LER value is derived from measured radiances, rather than from radiances calculated in turn for a BRF model from an external source. In the calculation of the LER value the assumption of a Rayleigh atmosphere is again made, while however the measurement may be of a scene containing clouds and aerosols. A subsequent histogram analysis of all LER values is then performed to select the measurement that is most likely free of clouds and aerosols, and the corresponding LER value is the Lambertian albedo reported in the climatology.

Vasilkov et al. (2017) have made a first comparison of NO_2 tropospheric air mass factors assuming LER values derived from top-of-atmosphere radiances calculated using MODIS BRF coefficients with box air mass factors assuming LER values read from the OMI LER climatology (Kleipool et al., 2008). The different LER values were also used for the retrieval of cloud parameters needed in turn for the air mass factor cloud correction. Differences up to 50% were found, with largest differences for smaller cloud fractions and pollution close to the ground.

5.5.5 Treatment of aerosols

For the first version of the S4 NO_2 processor, box air mass factors excluding the effects of aerosols are used. As an alternative algorithm implementation, we will investigate whether any available a priori information on aerosols improves the retrieval and, if so, how aerosol parameters should be treated in the NO_2 processor. The main source of aerosol information would be the CAMS aerosol forecasts. Since aerosol parameters from the S4 L2 SUR product are not delivered in near real-time, we doubt whether parameters from this product will be useful for the S4 NO_2 retrieval. When look-up tables are used, aerosol information can only be taken into account in a crude way. For example, box air mass factors are pre-calculated for a few (e.g. three to five) canonical aerosol scenarios and in retrieval, box air mass factors are read for the aerosol scenario being closest to the aerosol forecast ('closest' according to some metric). Alternatively, when box air mass factors are calculated online, the forecast aerosol extinction coefficient and single scattering albedo profiles can be included in the radiative transfer calculations.

As shown in Boersma et al. (2011), the cloud correction these authors use compensates under certain conditions at least partially for aerosol effects on the NO_2 columns. In their approach, absorption by O_4 is used to derive a cloud fraction for a Lambertian surface with fixed albedo. It has to be investigated, however, whether similar compensating effects are also expected for the cloud parameters from the S4 Cloud product. The OCRA cloud fraction (see below) is determined from an analysis of the colour of the scene. There are reports that OCRA responds differently to clouds and aerosols than cloud retrievals with a similar retrieval concept as one used by Boersma et al (2011) (see). More generally speaking, the treatment of aerosols in the calculation of box air mass factors and the cloud correction of box air mass factors should be considered together as they are dependent.

5.5.6 Look-up tables of box air mass factors

Box air mass factors are pre-calculated and stored in look-up tables as a function of the observation geometry, and the pressure and reflection properties of the atmosphere's lower bounding surface. The atmosphere's lower bounding surface can be either the ground surface or a cloud. Their reflection properties are in principle described by the models assumed in the S4 L2 SUR and S4 L2 Cloud algorithms and the model coefficients provided in the corresponding data products. The S4 BRF models have been discussed in the Section 5.5.4. The S4 L2 Cloud algorithm and product are briefly discussed in Section 5.5.9 and described in detail in [RD04]. At this point it is important to note that clouds are modelled as Lambertian surfaces of which the height and albedo are retrieved.

We mention that an additional look-up table is needed storing the sun-normalized radiance at the wavelength of the box air mass factor. These are used for the cloud correction described in Section 5.5.9. For now, it is only important to remark that this look-up table in principle has the same axes and nodes as the corresponding look-up tables of box air mass factors, simply because this is convenient. The exact grid spacing of the look-up tables is less critical than for the box air mass factor look-up tables and their size will also be much smaller (pressure axis absent).

A first version of the box air mass factor look-up table for S4 has been calculated assuming isotropic surface reflection. Table 5.2 gives the axes and the nodes of this look-up table. If the look-up table is to be used in combination with the BRF coefficients from the GSR product, probably the best way to proceed is to calculate the spherical albedo (Equation 5-53) and use this as a Lambertian-equivalent reflectivity to interpolate along the Lambertian albedo axis

Table 5.2. *Axes and nodes of the box air mass factor look-up table that is part of version 1.0 of the S4 L2PP and L2OP processors.* Isotropic surface reflection has been assumed in the calculations.

Dimension	Nodes	Number of nodes
Solar zenith angle (ϑ_0) [deg]	89.1, 88.3, 87.1, 85.7, 83.7, 81.4, 78.5, 75.5, 72.5, 69.5, 65.6, 61.6, 56.6, 51.3, 45.6, 39.2, 31.8, 22.3, 0.0	19
Viewing zenith angle (ϑ) [deg]	72.5, 66.4, 60.0, 53.1, 45.6, 36.9, 25.8, 0.0	8
Relative azimuth angle (φ-φ_0) [deg]	0, 30, 60, 90, 120, 150, 180	7
Lambertian surface / cloud albedo (A_s) [-]	0.0001, 0.02, 0.04, 0.06, 0.085, 0.11, 0.14, 0.18, 0.23, 0.29, 0.36, 0.43, 0.51, 0.6, 0.7, 0.8, 0.9, 1.0	18
Surface / cloud altitude a.s.l. (z_s) [km]	0.0, 0.1, 0.25, 0.5, 1.0, 2.0, 3.0, 4.0, 5.0, 10.0	10
Altitude levels a.s.l. (z_l) [km]	201 levels between 0.0 km and 95 km; finer spacing closer to surface; about 12 levels in lowest kilometre and about 33 levels in lowest three kilometres.	201
Surface / cloud pressures (p_s) [hPa]	From US Standard Atmosphere: 1013.0, … hPa	
Pressure levels (p_l) [hPa]	From US Standard Atmosphere: 1013 hPa - …	

5.5.7 A priori NO_2 and temperature profiles, surface pressures and other model data

NO_2 profiles

As explained above, column air mass factors depend on the NO_2 profile shape. Particularly in the troposphere the variability can be large and since the S4 pixel size is small, there is a need for spatially resolved information on the vertical distribution of NO_2. Therefore, a regional model with similar spatial resolution and temporal sampling as Sentinel-4 and with sufficient vertical levels particularly close to the surface is needed to provide profile forecasts for the lowest part of the atmosphere. A regional model typically calculates profiles for the lowest 3-5 km (above ground level) and a global model is therefore needed to complete the profiles in the free troposphere. For consistency, that global model should be the same model that is used for the separation of stratospheric and tropospheric NO_2 and the global model should provide the chemical boundary conditions for the regional model.

The baseline for the operational algorithm is to use profile forecasts from the CAMS regional model ensemble, extended by data from the CAMS global model. Profiles are provided by the ECA processor. At the time of writing, ensemble profiles are reported at eight levels with a top at 5 km, at 0.1° by 0.1° horizontal resolution, and with a time step of 1 h. Model levels are at the ground (0 m), 50 m, 250 m, 500 m, 1000 m, 2000 m, 3000 m and 5000 m above ground level. There is almost complete coverage of the S4 domain (including Iceland and Turkey). Chemical boundary conditions at the top and to the sides of the domain of each regional model are in principle provided by CAMS Global. From the perspective of the S4 NO_2 algorithm, a time step of 30 min would be preferred in order to better capture the photochemical partitioning of NO_x into NO and NO_2 (after all, S4 scans continuously.

Temperature profiles

Furthermore, temperature profiles are needed for the temperature correction of box air mass factors (Section 5.5.11). The CAMS global model solves and produces full meteorology, and uses for that basically the same modelling and assimilation system as the system operated by ECMWF for Numerical Weather Prediction. Temperature profiles could then be obtained either from CAMS Global or directly from ECMWF.

Surface pressures

Surface pressures are needed to calculate air mass factors for clear pixels. As with the temperature profiles, surface pressures could either be obtained from CAMS Global or from ECMWF. Surface pressure fields with a similar horizontal resolution as the S4 pixel are clearly preferred. The S4 pixel size is 8 x 8 km at the reference location at 45° N and 0° longitude; pixel sizes are typically smaller towards the south of this location and larger into the other directions. The S4 pixel size is comparable to the current resolution of the NWP data (about 9 km) and probably comparable to the resolution of CAMS Global by the time S4 is launched. Surface pressure fields from these two models would thus account for most of the elevation variability at S4's spatial sampling distance.

Other model data

The tropopause pressure is needed to separate NO_2 profiles into a tropospheric and stratospheric part. The tropospheric vertical column reported as the main retrieval result should be interpreted as the partial vertical column up to this pressure level. Again, the tropopause pressure could be obtained either from ECMWF or from CAMS Global. In practice, it is provided as tropopause layer by the ECA pre-processor.

5.5.8 Pre-processing of model data

ECA pre-processor

A separate S4 auxiliary processor prepares the model data for the L2 algorithms. This processor is called ECA (acronym for ECMWF-CAMS) and the pre-processing is described in detail in [RD10]. The main pre-processing steps are:

1. Interpolation / extrapolation to the time of the observation
2. Interpolation to the geolocation of the observation
3. Elevation corrections to the surface pressure
4. Merging of regional and global profiles
5. Resampling of vertical grid
6. Unit conversions
7. Derivation of tropopause layer index

The NO_2 processor reads all relevant data fields for the respective L1b pixel from the engineering product produced by the ECA processor. Trace gas profiles are given as layer partial columns in units of mol m^{-2}. Profile variables follow a hybrid sigma-pressure vertical coordinate system. The associated set of a and b coefficients is specific for S4.

5.5.9 Cloud parameters for the NO_2 fit window

Clouds are modelled as Lambertian surfaces at a certain height and with a certain albedo that cover the ground pixel with a certain fraction. These three cloud parameters are in principle provided by the S4 L2 Cloud core product ([RD05]). The forward model of the Cloud algorithm is based on the independent-pixel approximation, which considers the top-of-atmosphere radiance as the sum of independent contributions from horizontally homogeneous sub-columns. In this case, the sub-columns are the clear and cloudy part of the pixel (R_{clr} and R_{cld}, respectively). For partly cloudy pixels, the reflectance is written according to the independent-pixel approximation as

$$R(\lambda) = (1 - f_{cld})R_{clr}(\lambda) + f_{cld}R_{cld}(\lambda) \quad \text{5-54,}$$

where f_{cld} is in principle a geometric cloud fraction but in practice a cloud fraction that typically depends on the particular forward model used to describe R_{cld} and on the wavelength range from which it is retrieved. To calculate air mass factors in partly cloudy atmospheres we need however cloud parameters that best describe the effect of clouds on the radiation field in the wavelength range of the NO_2 fit window. We also need the so-called cloud radiance fraction f_{cld}^{rad}, which is the fraction of the total amount of radiation reaching the sensor that originates from the cloudy part of the pixel. The cloud radiance fraction can be expressed as

$$f_{cld}^{rad} = \frac{f_{cld}R_{cld}(\lambda)}{R(\lambda)} \quad \text{5-55,}$$

where for our purposes the fraction should again be representative of wavelengths in the NO_2 fit window.

The S4 L2 Cloud algorithm consists of two subsequent algorithm steps. The Optical Cloud Recognition Algorithm (OCRA) algorithm derives a cloud fraction based on an analysis of the colour of the scene using integrated radiances in two broad wavelength bands in the UVis channel at …. The OCRA cloud fraction f_{cld}^{OCRA} is an input for the Retrieval of Cloud Information using Neural Networks (ROCINN) algorithm, which retrieves cloud optical thickness / cloud albedo and cloud pressure from the oxygen A band in the NIR channel. We only use the version of ROCINN that models clouds as Lambertian surfaces (version 'CRB') to limit the size of box air mass factor look-up tables, even though clouds may sometimes be optically thin and have significant transmission. As the ground pixels seen in the UVis and NIR channels are slightly shifted (spatial mis-registration), the OCRA cloud fraction, which is by definition derived on the UVis pixel grid, is first interpolated to the NIR pixel grid by the Cloud processor. From an inversion of O_2 A band spectra, the Lambertian cloud albedo A_c^{ROC} and pressure p_c^{ROC} are derived by solving

$$\tilde{R}(\lambda_i^{O2A}) = (1 - f_{cld}^{OCRA})\tilde{R}_{clr}(\lambda_i^{O2A}; \rho_s^{NIR}, p_s) + f_{cld}^{OCRA}\tilde{R}_{cld}(\lambda_i^{O2A}; A_c^{ROC}, p_c^{ROC}) + \epsilon \quad \text{5-56.}$$

Here we have made explicit that the assumed surface BRF model parameter values ρ_s hold for the wavelengths of the fit window in the near-infrared wavelength range. The cloud albedo and cloud pressure as retrieved on the NIR pixel grid are then interpolated to the UVis pixel grid. In the S4 NO_2 retrieval algorithm, the three cloud parameters (OCRA cloud fraction, ROCINN cloud albedo and ROCINN cloud pressure) will be read from the S4 L2 Cloud product for the UVis pixel grid and we will assume that co-registration of the UVis and NIR channels has been accurately dealt with by the Cloud processor.

A flow diagram of the CLD submodule is given in Figure 5.9. In the baseline implementation, we directly use the ROCINN Lambertian cloud albedo and ROCINN cloud pressure to calculate box air mass factors for the cloudy part of the pixel. For calculation of the cloud radiance fraction we create look-up tables of sun-normalized radiances at the wavelength of the air mass factor (λ_0^{NO2}). Sun-normalized radiances are a function of the observation geometry and the pressure and reflection properties of the atmosphere's lower bounding surface. Reflection properties of the ground surface are described in the same way as in look-up tables for the box air mass factors discussed earlier. Sun-normalized radiances for the clear and cloudy part of the pixel are read from the look-up tables and the cloud radiance fraction for the NO_2 fit window is calculated from the following equations

$$R^{sim}(\lambda_o^{NO2}) = \left(1 - f_{cld}^{OCRA}\right)R_{clr}^{sim}\left(\lambda_0^{NO2}; \rho_s^{VIS}, p_s\right) + f_{cld}^{OCRA}R_{cld}^{sim}\left(\lambda_0^{NO2}; A_c^{ROC}, p_c^{ROC}\right) \quad 5\text{-}57$$

and

$$f_{cld}^{rad} = \frac{f_{cld}^{OCRA}R_{cld}^{sim}\left(\lambda_0^{NO2}; A_c^{ROC}, p_c^{ROC}\right)}{R^{sim}(\lambda_0^{NO2})} \quad 5\text{-}58.$$

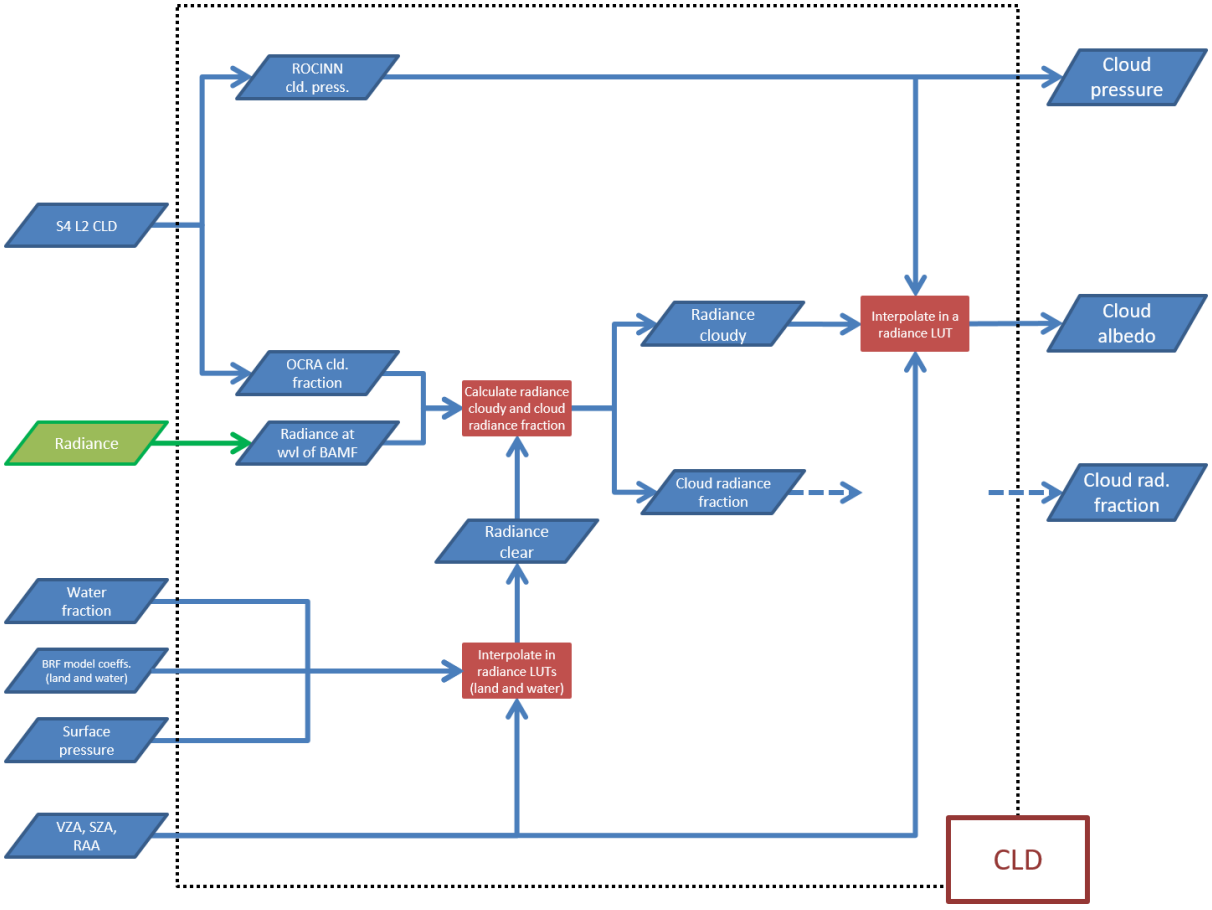

Figure 5.9. The structure of the CLD submodule with its most important data fields. This submodule is part of the AMF module shown in Figure 5.7.

5.5.10 Column air mass factor for a clear, cloudy and partly cloudy atmosphere

Slant columns are fitted for all S4 pixels and pixels with high cloud fraction are not filtered out from processing. From the independent-pixel approximation and the definition of the box air mass factor it follows that the box air mass factor of a partly cloudy pixel is given by

$$m(z,\lambda) = (1 - f_{cld}^{rad})\, m_{clr}(z,\lambda) + f_{cld}^{rad} m_{cld}(z,\lambda) \quad \text{5-59,}$$

where the weight is the cloud radiance fraction f_{cld}^{rad} discussed in the previous section. If we assume the profile shapes $n(z)/\int n(z)dz$ in the clear and cloudy sub-column to be the same, the column air mass factor for a partly cloudy pixel can be calculated using the same weight factors as

$$M = (1 - f_{cld}^{rad})\, M_{clr} + f_{cld}^{rad} M_{cld} \quad \text{5-60,}$$

see also Martin et al., 2002. The weighting of air mass factors for clear and cloudy atmospheres as in Equation 5-60 has been used in many previous tropospheric satellite NO_2 retrievals.

The column air mass factor for the partly cloudy atmosphere (M) of the L1b pixel under consideration is now determined by taking the following steps.

- The observation geometry and the water fraction are read from the L1b product.
- BRF coefficients for the L1b pixel are obtained from GSR's daily map of BRF coefficients by nearest-neighbour interpolation in the corresponding L1c grid. Wavelength dependent coefficients are read for the wavelength closest to the wavelength of the box air mass factors (i.e GSR wavelength of 457 nm). If the water fraction is larger than 0.5, BRF coefficients are taken for the water BRF model, otherwise for the land BRF model.
- The CLD module provides ROCINN Lambertian cloud albedo (baseline) or the Lambertian cloud albedo recalculated for the NO_2 fit window (future development) as well as the ROCINN cloud pressure and the cloud radiance fraction in the NO_2 fit window.
- NO_2 profiles, temperature profiles, surface pressures and tropopause layer index are provided for the L1b pixel by the ECA engineering product. Model bias corrections from the BG module are applied to the stratospheric part of the NO_2 profiles.
- Linear interpolation in the look-up tables is used to calculate profiles of box air mass factors for the clear and cloudy part (m_{clr} and m_{cld}). Interpolation axes are the solar zenith angle, viewing zenith angle, relative azimuth angle, surface pressure and the spherical albedo (clear) or Lambertian cloud albedo (cloudy). In case of online RTM calculations, box air mass factors are calculated directly.
- Profiles of box air mass factors are linearly interpolated onto the pressure mid points of the model layers. Vertical interpolations in BAMF look-up tables are preferably performed on the pressure axes rather than on the corresponding altitude axes.
- Temperature correction factors are calculated and applied to the box air mass factors, see Section 5.5.11.
- Column air mass factors for the clear and cloudy atmospheric column (M_{clr} and M_{cld}) are calculated from box air mass factors by a simple summation over layers according to Equations 5-40-5-42, where the vertical discretization of the atmosphere coincides with model layers of the a priori profiles provided by the ECA processor.
- Finally, the clear and cloudy column air mass factors are weighted with the cloud radiance fraction as described above.

We remark that values falling outside of the range of the look-up table are currently clipped to their nearest boundary grid node (linear extrapolation is possible but switched off).

For small OCRA cloud fractions and / or small ROCINN Lambertian cloud albedos, the uncertainty in the retrieved ROCINN cloud pressure and cloud albedo may be so large that any cloud correction does not improve the accuracy of the NO_2 retrieval. Therefore, the cloud correction is only applied when the product of OCRA cloud fraction and ROCINN cloud albedo is above a certain threshold (e.g. 0.08),

$$\text{cloud correction if: } f_{cld}^{OCRA} \cdot A_c^{ROC} > \text{threshold} \quad \text{5-61,}$$

while below this threshold we simply assume the pixel to be clear. Alternatively, a threshold may be set directly on the cloud radiance fraction.

5.5.11 Temperature correction

Fitting of the background polynomial basically removes the broadband absorption from the cross-sections. Absorption cross-sections can thus be split into a smooth part and a differential part

$$\sigma_j(\lambda) = \sigma_j^{smooth}(\lambda) + \sigma_j^{diff}(\lambda) = \sum_p c_p \lambda^p + \sigma_j^{diff}(\lambda) \quad \text{5-62,}$$

where the separation depends on the degree of the polynomial. The NO_2 absorption cross-section has a clear temperature dependence, which mainly results in a scaling of these differential absorption structures. The choice of the cross-section $\sigma(T_{ref},\lambda)$ used in the DOAS fit therefore affects the retrieved slant column. The SCD will be true, only if the temperature agrees with the effective temperature of the atmospheric NO_2. For example for ozone retrievals in the UV, the effective temperature can be determined from the DOAS fit itself. However, this is not possible for NO_2, because the temperature derivative and absorption cross-section are highly linear dependent. Therefore, a correction is applied in the AMF step, which uses model temperature profiles to correct the reference temperature of the NO_2 absorption cross-section used in the DOAS step for the actual temperature profile (Boersma et al., 2004).

For atmospheric conditions, the scaling is nearly linear and the correction factor can be assumed proportional to the temperature difference. We write for the box air mass factors including the temperature correction (indicated by the asterisk)

$$m_l^* = c_l^T \cdot m_l \quad \text{5-63,}$$

where the m_l is, as before, the box air mass factor calculated by SCIATRAN (compare with Equation 5-38 or see for example the discussion of weighting function DOAS in Rozanov and Rozanov, 2010) and the temperature correction factor is

$$c_l^T = \frac{\sigma(T_l,\lambda)}{\sigma(T_{ref},\lambda)} \quad \text{5-64.}$$

The temperature correction factor is parameterized as

$$c_l^T = 1 - a \cdot (T_l - T_{ref}) \quad \text{5-65.}$$

In this form, a has a positive value and its minus sign explicitly indicates that the absorption cross-section's differential structure gets weaker with increasing temperature. The factor a is, for example, determined by a least-squares fit to laboratory cross-sections at different temperatures (after convolution with the instrument response functions and subtraction of the smooth part) according to

$$a = \left(1 - \frac{\tilde{\sigma}^{diff}(T,\lambda_i)}{\tilde{\sigma}^{diff}(T_{ref},\lambda_i)}\right) \cdot \frac{1}{(T - T_{ref})} \quad \text{5-66.}$$

Thus, the temperature correction factor depends on the resolution of the instrument, the fit window but also the degree of the polynomial. Temperature-corrected box air mass factors depend on the temperature profile in addition to NO_2 profiles.

Figure 5.10 shows two examples of temperature correction factors as they are used at IUP Bremen in air mass factor calculations for OMI. The determination of these correction factors is in principle the same as for the S4 NO_2 algorithm. The figure illustrates that the temperature variability of the absorption strength of NO_2 is substantial. Partial slant columns in the lowest part of the atmosphere (where temperatures are higher than the reference temperature) would be underestimated by more than 20% if the temperature variability were not taken into account.

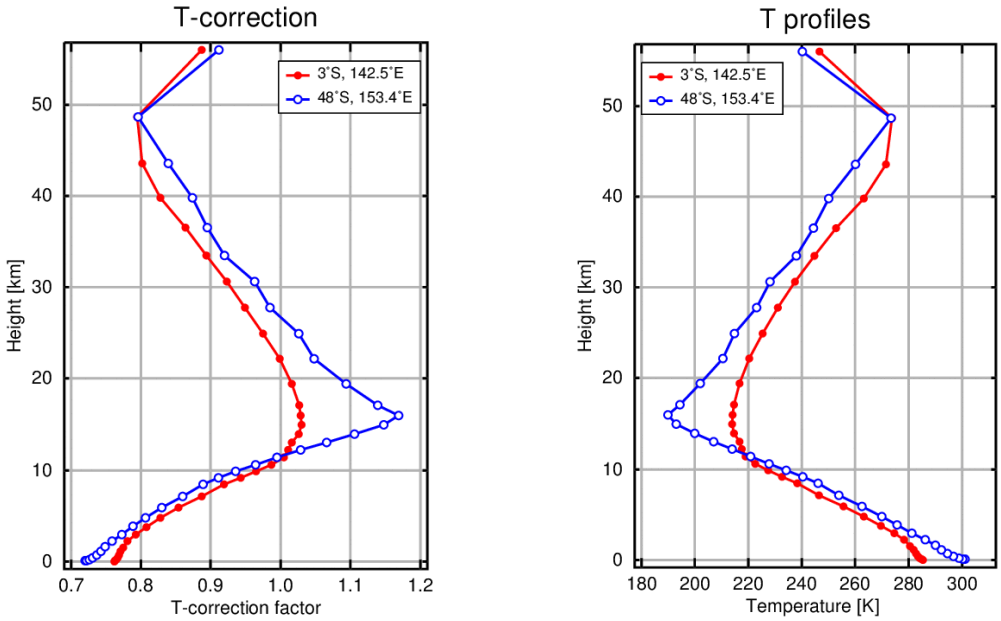

Figure 5.10. Two example profiles of temperature correction factors as they are used at IUP Bremen in air mass factor calculations for OMI. The determination of these correction factors is in principle the same as for the S4 NO_2 retrieval algorithm. The temperature profiles are taken from TM4 for two locations in China and Southeast Asia on February 2, 2005 (early afternoon). The systematic correction is largest near the surface (more than 20%).

5.6 Characterisation and error analysis

5.6.1 Averaging kernels and air mass factors

Whereas a weighting function, such as the altitude-resolved air mass factor, describes the sensitivity of the measurement to the true state, the averaging kernel (e.g. Rodgers, 2000) gives the sensitivity to the true state of the retrieval. For column retrievals, the averaging kernel can be written as

$$A(z) = \frac{\partial^2 \hat{N}_v}{\partial n(z) \partial z} \qquad 5\text{-}67,$$

where the ^-accent explicitly indicates that the vertical column is a retrieved quantity here. This derivative is in principle evaluated at the retrieved state. Within the context of DOAS retrievals, the forward model can also be linearized around zero absorption (Section 5.5.1). The averaging kernel becomes

$$A(z) = \frac{\partial \hat{N}_v}{n(z) \partial z} \qquad 5\text{-}68.$$

We can further expand this expression as

$$A(z) = \frac{\partial \widehat{N}_v}{\partial \ln\left(\tilde{I}_n(\lambda_i)\right)} \cdot \frac{\partial \ln\left(\tilde{I}_n(\lambda_i)\right)}{n(z)\partial z} = \frac{\partial \widehat{N}_v}{-\tilde{\sigma}\left(T_{ref}, \lambda_i\right) \partial N_s} \cdot \frac{\partial \ln\left(\tilde{I}_n(\lambda_i)\right)}{n(z)\partial z} \qquad \text{5-69.}$$

The derivative $\partial \widehat{N}_v / \partial N_s$ in the first factor is equal to the inverse of the total air mass factor, while the altitude-resolved air mass factor can be recognized in the second factor. We thus have

$$A(z) = \frac{1}{-\tilde{\sigma}\left(T_{ref}, \lambda_i\right) \cdot M} \cdot -\tilde{\sigma}(T(z), \lambda_i) \cdot m(z) = \frac{c^T(z) \cdot m(z)}{M} = \frac{m^*(z)}{M} \qquad \text{5-70,}$$

where the temperature correction factor (c^T) is included in the air mass factor. A detailed derivation can be found in Eskes and Boersma (2003).

Fitted slant columns may first need to be de-striped before the air mass factor can be applied. In that case the derivative $\partial \widehat{N}_v / \partial N_s$ in Equation 5-69 should be replaced by $\partial \widehat{N}_v / \partial N_s^{fit}$. However, de-striping is an additive offset correction and the correction term is given by external input (it basically is a forward model parameter) so that the two derivatives are the same. Furthermore, it is useful to distinguish between the averaging kernel for the total column and the averaging kernel for the tropospheric column. Following a similar reasoning as for the stripe correction, the stratospheric correction is additive ($N_s^{trop} = N_s - N_s^{strat}$) and the stratospheric contribution is given by external input so that $dN_s = dN_s^{trop}$. The averaging kernel for the tropospheric column is then given by Equation 5-70 as well, provided that the tropospheric air mass factor is used and only tropospheric levels are considered (not further derived).

In terms of finite differences, we now have for the total column averaging kernel

$$A_l = \frac{c_l^T \cdot m_l}{M} = \frac{m_l^*}{M} \quad l = l_{toa}, \dots, l_{boa} \qquad \text{5-71,}$$

and for the tropospheric column averaging kernel

$$A_l^{trop} = \begin{cases} 0 & l = l_{toa}, \dots, l_{tp} - 1 \\ \dfrac{c_l^T \cdot m_l}{M^{trop}} = \dfrac{m_l^*}{M^{trop}} & l = l_{tp}, \dots, l_{boa} \end{cases} \qquad \text{5-72.}$$

The averaging kernel for the total column ($\mathbf{A}$) and the air mass factors M, M^{trop} and M^{strat} are reported in the L2 product. From this, the averaging kernel for the tropospheric column ($\mathbf{A}^{trop}$) can be derived.

We remark that the total vertical column resulting from the DOAS fit (N_s/M) is in general different from the sum of stratospheric (N_v^{strat}) and tropospheric (N_v^{trop}) vertical columns:

$$N_s/M \neq N_v^{trop} + N_v^{strat} \qquad \text{5-73.}$$

Whenever the two estimates of the total column may be confused, we will explicitly distinguish between the summed total vertical column and the DOAS total vertical column defined as

$$N_v^{sum} = N_v^{trop} + N_v^{strat} \quad \text{summed total vertical column} \qquad \text{5-74}$$

and

$$N_v^{DOAS} = N_v = {}^{N_s}/_{M} \quad \text{DOAS total vertical column} \qquad \text{5-75,}$$

respectively. The most accurate estimate of the total vertical column is the summed total vertical column. For the specific purpose of an assimilation of total columns, the quantity of interest is however the DOAS total column.

5.6.2 Error propagation for the vertical columns

An estimate of the total error in the tropospheric NO_2 column is in principle determined based on linearized error propagation closely following every step of the retrieval chain from radiance spectrum to tropospheric column. In general, the tropospheric NO_2 column is a function f of a set of input parameters $\mathbf{x}$, and the σ-error is then given by

$$\sigma^2 = \mathbf{K}\,\mathbf{S_x}\,\mathbf{K}^T \qquad \text{5-76,}$$

where $\mathbf{S_x}$ is the error covariance matrix of the input parameters and $\mathbf{K}$ is a row vector containing the derivatives

$$K_j = \frac{\partial f}{\partial x_j} \qquad \text{5-77.}$$

The derivatives can be calculated relatively straightforward. As an example, if we write for the forward model

$$\hat{N}_v^{trop} = \frac{N_s^{fit} - A^{stripe} - N_s^{strat}}{M^{trop}} \qquad \text{5-78,}$$

ignore for now the error in the stripe correction and assume uncorrelated errors in the other three inputs (see also the discussion below), the error in the tropospheric column is given by

$$\left(\sigma_{\hat{N}_v^{trop}}\right)^2 = \left(\frac{\sigma_{N_s^{fit}}}{M^{trop}}\right)^2 + \left(\frac{\sigma_{N_s^{strat}}}{M^{trop}}\right)^2 + \left(\frac{\left(N_s^{fit} - A^{stripe} - N_s^{strat}\right)\cdot \sigma_{M^{trop}}}{(M^{trop})^2}\right)^2 \qquad \text{5-79}$$

(e.g. Boersma et al., 2004). The ^-accent explicitly indicates that the vertical column is a retrieved quantity, which depends on the assumptions made in the forward model and the estimates for the forward model parameters. The uncertainty of the tropospheric airmass factor can in turn be determined by error propagation from the individual contributions

$$(\sigma_{M^{trop}})^2 = \left(\frac{\partial M}{\partial A_s}\cdot \sigma_{A_s}\right)^2 + \left(\frac{\partial M}{\partial f_{cld}^{rad}}\cdot \sigma_{f_{cld}^{rad}}\right)^2 + \left(\frac{\partial M}{\partial p_{cld}}\cdot \sigma_{p_{cld}}\right)^2 + \left(\frac{\partial M}{\partial s}\cdot \sigma_s\right)^2 \qquad \text{5-80}$$

Where σ_{A_s} is the uncertainty of the surface reflectance, here assumed to be the spherical albedo, $\sigma_{f_{cld}}^{rad}$ is the uncertainty in the radiative cloud fraction. $\sigma_{p_{cld}}$is the uncertainty in cloud pressure and σ_S is the uncertainty in vertical profile. The uncertainty in the temperature correction ignored in this formulation.

The sensitivities of the AMF to surface reflectance and cloud pressure can be determined from the BAMF LUT itself by computing numerical derivatives of the BAMFs for the current input parameters and applying equation 5-60. Uncertainties for the parameters themselves can either be estimated from literature or for S4 operations be taken from the respective lv2 product used.

The sensitivity to cloud fraction can be directly computed from equation 5-60. The uncertainty of the cloud fraction itself can again either be taken from literature or from the respective lv2 product.

The sensitivity to profile shape is not simple to evaluate, as it is not clear at all how accurate the a priori profiles provided by the CAMS model are, how this uncertainty is distributed with altitude and what the vertical correlations are. Therefore, a simplified approach is taken where the CAMS profile is shifted up and down by a certain amount keeping the upper and lower points in the tropospheric profile fixed. Tropospheric AMFs are computed for both profiles and the half of the difference is used as a rough estimate for the AMF uncertainty from the profile.

While the derivatives with respect to surface reflectance and cloud fraction are smooth and “well behaved”, the derivatives with respect to cloud top height and atmospheric profile can have sharp changes, in particular if the cloud top height is close to the upper edge of a well-

mixed layer. In this situation, even a small change in profile or cloud height can lead to a large change in air mass factor.

Equations 5-79 and 5-80describe the uncertainty calculations performed in the baseline implementation of the S4 NO_2 processor. In the following, a more elaborate uncertainty discussion is provided, which may become a future development.

The trueness of the tropospheric column error estimate primarily depends on the trueness of the estimate of the covariance matrix, i.e. the trueness of the estimates of the σ-errors in input parameters but also of their correlations. Construction of the input parameter error covariance matrix $\mathbf{S}_x$ is the most challenging part.

Below we will describe in some detail an error analysis for S4 NO_2. We identify the most significant error sources and describe how they propagate into the total error budget. The algebra is relatively straightforward, although admittedly a bit tedious. The main purpose of the following section, however, is to explore how an error analysis for S4 NO_2 could be shaped when we (i) refrain from the assumption of uncorrelated error sources, (ii) use the model profiles for the error propagation, and (iii) explicitly incorporate error estimates in input parameters as (they should be) provided by the auxiliary data products. *At this point, we only discuss the error propagation for a clear pixel.* The error propagation for partly cloudy pixels has an additional layer of complexity that may be addressed at a later stage when this approach turns out to be feasible. As will be further explained below, the error estimate for the tropospheric column resulting from this analysis should be interpreted as *random* on the level of a single pixel and its value reported in the L2 product as an estimate of the standard deviation of the underlying distribution (σ-error). *As such, the definition of the '[…]_precision' quantities in the L2 product actually conforms to the definition of the so-called single-pixel 'standard uncertainty' adopted in ESA's Climate Change Initiative program (Merchant et al., 2017).*

A distinction is usually made between random and systematic errors. Before continuing we want to make a few remarks on this distinction that are relevant for understanding the remainder of this section. First, whether an error can be considered random or systematic often depends on the level of aggregation. For example, the noise error in the daily irradiance results in a systematic error for all slant columns retrieved on a particular day, but when comparing slant columns from many different days, the noise error in the daily irradiance constitutes a random slant column error. (Fortunately, the irradiance noise error is expected to be very small compared to the other errors.) Second, in absence of detailed knowledge of a systematic error's dependencies, a systematic error can often be treated as a quasi-random error (i.e. as a random variable). This applies in particular when discussing errors on the aggregation level of a single pixel, as is the focus here. For example, when the S4 instrument is partly polarisation sensitive, a quasi-random error is created because the polarisation state of the incoming light, which is unknown, is different for every pixel. Treating a systematic error as a quasi-random error means that the unknown bias offset A for an individual pixel is described as the standard deviation σ of a probability distribution. The width of this distribution represents a priori knowledge of the possible range of the offset. Third, an example of a quasi-random error is the error in a bias correction itself. For example, the spatiotemporal model biases discussed in Section 5.4.4 may depend on parameters such as local time, solar zenith angle, latitude, CCD row, orbit phase and more. The BG module tries to parameterize the main dependencies and calculates an average bias correction pattern $\bar{A}$, which is basically the mean of the aforementioned probability distribution. Since not all dependencies will have been accurately parameterized, under-corrections and over-corrections occur on the level of a single pixel when applying this correction pattern. Residual biases after correction can be considered a quasi-random error. Fourth, when averaging pixels into composites, truly random errors average out, while quasi-random and systematic errors may not. (This is not further discussed in this document, but see the discussion in for example the S4 SO2 [RD07] and HCHO [RD08] ATBDs.)

The error in the slant column from the DOAS fit is the result of contributions from the radiance noise error and from systematic effects such as systematic instrument errors, inaccurate reference spectra, and atmospheric scattering or surface reflection effects not properly accounted for in the DOAS equation. These systematic errors affect the retrieved NO_2 slant column only to the extent that their effect on the measured spectrum $\ln\left(\tilde{I}(\lambda_i)/\tilde{E}_0(\lambda_i)\right)$ is parallel to the NO_2 absorption cross-section $\tilde{\sigma}(\lambda_i)$; systematic errors however increase fit residuals to the extent that the spectral structures are orthogonal. Analyses of slant column errors show that the noise error provides the dominant contribution (Zara et al., in preparation). Assuming then uncorrelated random errors with a constant magnitude across the fit window, the error in the slant column can be estimated from the residual's root-mean-square deviation Δ^2_{RMS} as outlined towards the end of Section 5.2.1: $\frac{m}{m-n}\Delta^2_{RMS}$ is taken as the σ-error for each spectral point of the measurement $\ln\left(\tilde{I}(\lambda_i)/\tilde{E}_0(\lambda_i)\right)$ and propagated into a slant column σ-error (Equation 5-16).

In the next step of the retrieval chain, tropospheric slant columns are calculated. Treating the stratospheric and stripe correction as a single step, tropospheric columns are given by

$$N_s^{trop} = N_s^{fit} - A^{stripe} - \sum_{l=l_{toa}}^{l_{tp}-1} m_l \cdot c_l^T \cdot N_{v,l}^* \qquad 5\text{-}81,$$

where the summation is over atmospheric layers from the top-of-atmosphere (l_{toa}) to the tropopause (l_{tp}) and $N_{v,l}^*$ is the bias-corrected profile of partial columns from the model. The error in the tropospheric slant column is thus the result of contributions from the error in the fitted slant column as discussed above, and from inaccurate stripe corrections, stratospheric box air mass factors, temperature corrections and stratospheric NO_2 profiles.

Stripe correction patterns are determined by suitably averaging many fitted slant columns from the past period. The error in the stripe correction for the current slant column is composed of errors inherent in this analysis and it is due to the temporal variability of stripe offsets between the time period of the stripe analysis and the current measurement. The latter effect may be the more important one. The temporal dependence of stripe offsets is, however, a priori unknown and this error source can therefore be considered quasi-random. In addition, we assume that any correlations between the error in stripe corrections and the error in model bias corrections are negligible because of the (very) different averaging strategies used for determining these bias corrections (Section 5.4.3). Next, the error in stratospheric box air mass factors can generally be ignored. Furthermore, the error in the temperature correction c_l^T is mainly related to the uncertainty in the temperature profile: the error caused by any deviations from the linear temperature dependence is expected to be negligible. The uncertainty in the temperature profile is described by an error covariance matrix and this covariance matrix has non-zero off-diagonal elements because errors are correlated across model layers. Finally, we also quantify the error in the bias-corrected stratospheric profile $N_{v,l}^*$ as a σ-error, which is again correlated across model layers.

Thus, the total σ-error in the tropospheric slant column is

$$\begin{aligned}\left(\sigma_{N_s^{trop}}\right)^2 &= \left(\sigma_{N_s^{fit}}\right)^2 + \left(\sigma_{A^{stripe}}\right)^2 \\ &+ \sum_{i=l_{toa}}^{l_{tp}-1}\sum_{j=l_{toa}}^{l_{tp}-1} m_i \cdot a \cdot N_{v,i}^* \cdot (\mathbf{S_T})_{i,j} \cdot m_j \cdot a \cdot N_{v,j}^* \\ &+ \sum_{i=l_{toa}}^{l_{tp}-1}\sum_{j=l_{toa}}^{l_{tp}-1} m_i \cdot c_i^T \cdot \left(\mathbf{S}_{\mathbf{N_v^*}}\right)_{i,j} \cdot m_j \cdot c_j^T\end{aligned} \qquad \text{5-82.}$$

In this equation, $\mathbf{S_T}$ is the error covariance matrix of the temperature profile and $\mathbf{S}_{\mathbf{N_v^*}}$ is the error covariance matrix of bias-corrected model profile. The factor a is the scaling coefficient from the temperature correction (Equation 5-65).

As a starting point for construction of the covariance matrices $\mathbf{S}_{\mathbf{N_v^*}}$ and $\mathbf{S_T}$, parameterizations of covariance matrices provided by CAMS could be used. In addition, for the lowest levels, which are provided by the regional model ensemble, the variability of the ensemble around the median can be assessed to provide additional information. The ECA pre-processing then not only provides for every S4 pixel the combined model profiles from the global and regional model, but also the corresponding covariance matrices $\mathbf{S}_{\mathbf{N_v}}$. Diagonal elements of the covariance matrix for the NO_2 profile may perhaps need to be scaled to account for the model bias correction step, which would then provide the covariance matrix $\mathbf{S}_{\mathbf{N_v^*}}$.

In the final step, tropospheric vertical columns are calculated according to

$$\widehat{N}_v^{trop} = \frac{N_s^{trop}}{M^{trop}} = N_s^{trop} \cdot \frac{\sum_{l=l_{tp}}^{l_{boa}} N_{v,l}^*}{\sum_{l=l_{tp}}^{l_{boa}} m_l \cdot c_l^T \cdot N_{v,l}^*} \qquad \text{5-83.}$$

The error in the tropospheric vertical column is thus the result of contributions from the error in the tropospheric slant column as discussed above, and from inaccurate tropospheric model profiles, temperature corrections and tropospheric box air mass factors. To simplify the derivations and the discussion of the various error contributions, we now temporarily make the unrealistic assumption that correlations between stratospheric $\{l_{toa}, \ldots, l_{tp}-1\}$ and tropospheric model levels $\{l_{tp}, \ldots, l_{boa}\}$ are zero. In that case, the error in the tropospheric slant column is uncorrelated to any of the other three error contributions.

After some rearrangement of terms, we can now write for the error in the tropospheric vertical column

$$\left(\sigma_{\widehat{N}_v^{trop}}\right)^2 = \left(\frac{\sigma_{N_s^{trop}}}{M^{trop}}\right)^2 + \left(\frac{N_s^{trop}}{M^{trop} \cdot \sum_{l=l_{tp}}^{l_{boa}} N_{v,l}^*}\right)^2 \cdot \sum_{i=l_{tp}}^{l_{boa}} \sum_{j=l_{tp}}^{l_{boa}} \left(\frac{m_i \cdot c_i^T}{M^{trop}} - 1\right) \left(\mathbf{S}_{\mathbf{N}_\mathbf{v}^*}\right)_{i,j} \left(\frac{m_j \cdot c_j^T}{M^{trop}} - 1\right) + \left(\frac{N_s^{trop}}{M^{trop} \cdot \sum_{l=l_{tp}}^{l_{boa}} N_{v,l}^*}\right)^2 \cdot \sum_{i=l_{tp}}^{l_{boa}} \sum_{j=l_{tp}}^{l_{boa}} \frac{m_i \cdot a \cdot N_{v,i}^*}{M^{trop}} \cdot \left(\mathbf{S}_\mathbf{T}\right)_{i,j} \cdot \frac{m_j \cdot a \cdot N_{v,j}^*}{M^{trop}} + \left(\frac{N_s^{trop}}{M^{trop} \cdot \sum_{l=l_{tp}}^{l_{boa}} N_{v,l}^*}\right)^2 \cdot \sum_{i=l_{tp}}^{l_{boa}} \sum_{j=l_{tp}}^{l_{boa}} \frac{c_i^T \cdot N_{v,i}^*}{M^{trop}} \cdot \left(\mathbf{S}_\mathbf{m}\right)_{i,j} \cdot \frac{c_j^T \cdot N_{v,j}^*}{M^{trop}} \quad \text{5-84.}$$

(stratosphere and troposphere uncorrelated)

Matrix $\mathbf{S_m}$ is the error covariance matrix of the box air mass factor.

We now allow errors in model data to be correlated across all levels and we can generalize Equation 5-79 and the previous equations as

$$\left(\sigma_{\widehat{N}_v^{trop}}\right)^2 = \left(\frac{\sigma_{N_s^{fit}}}{M^{trop}}\right)^2 + \left(\frac{\sigma_{A^{stripe}}}{M^{trop}}\right)^2 + \left(\frac{\partial \widehat{N}_v^{trop}}{\partial \mathbf{N_v}}\right) \mathbf{S}_{\mathbf{N}_\mathbf{v}^*} \left(\frac{\partial \widehat{N}_v^{trop}}{\partial \mathbf{N_v}}\right)^T + \left(\frac{\partial \widehat{N}_v^{trop}}{\partial \mathbf{T}}\right) \mathbf{S_T} \left(\frac{\partial \widehat{N}_v^{trop}}{\partial \mathbf{T}}\right)^T + \left(\frac{\partial \widehat{N}_v^{trop}}{\partial \mathbf{m}}\right) \mathbf{S_m} \left(\frac{\partial \widehat{N}_v^{trop}}{\partial \mathbf{m}}\right)^T \quad \text{5-85.}$$

The derivatives in this equation are given by the row vectors

$$\frac{\partial \widehat{N}_v^{trop}}{\partial \mathbf{N_v}} = \left[-\frac{m_l \cdot c_l^T}{M^{trop}}, -\frac{\widehat{N}_v^{trop}}{N_v^{*,trop}} \cdot \left(\frac{m_l \cdot c_l^T}{M^{trop}} - 1\right)\right]$$

$$\frac{\partial \widehat{N}_v^{trop}}{\partial \mathbf{T}} = \left[\frac{m_l \cdot a \cdot N_{v,l}^*}{M^{trop}}, \frac{\widehat{N}_v^{trop}}{N_v^{*,trop}} \cdot \left(\frac{m_l \cdot a \cdot N_{v,l}^*}{M^{trop}}\right)\right] \quad \text{5-86,}$$

$$\frac{\partial \widehat{N}_v^{trop}}{\partial \mathbf{m}} = \left[-\frac{c_l^T \cdot N_{v,l}^*}{M^{trop}}, -\frac{\widehat{N}_v^{trop}}{N_v^{*,trop}} \cdot \left(\frac{c_l^T \cdot N_{v,l}^*}{M^{trop}}\right)\right]$$

where the first expression in each vector runs over stratospheric levels $l \in \{l_{toa}, \ldots, l_{tp} - 1\}$ and the second expression runs over tropospheric levels $l \in \{l_{tp}, \ldots, l_{boa}\}$. Furthermore, $N_v^{*,trop}$ is the tropospheric vertical column calculated from the bias-corrected model profile and the derivatives are in principle evaluated at the retrieval solution $\widehat{N}_v^{trop}$ (but see also next section).

As a last step, we need to determine the error covariance matrix $\mathbf{S_m}$ of the box air mass factor. We have assumed above that the error in the box air mass factor for stratospheric levels is negligible. The error covariance matrix $\mathbf{S_m}$ has non-zero entries only for tropospheric levels. Furthermore, as already mentioned, we currently only do a full error propagation for clear pixels. Then, the error in the clear-sky box air mass factor is primarily the result of contributions from errors in the surface pressure, errors in surface reflectance parameters, look-up table interpolation errors and forward model errors made in the calculation of box air mass factors. The latter category is related in particular to the assumed absence of aerosols and residual clouds.

We assume that the error in the surface pressure can be ignored. As a starting point for the error in the surface reflectance parameters, the variances and covariances provided by the GSR product may be used. Forward model errors including interpolation errors are for now grouped into a single quasi-random error contribution that may perhaps be quantified as a constant relative error p in the air mass factor (of for example 1-2%).

We can now write for the covariance matrix $\mathbf{S_m}$

$$\mathbf{S_m} = \begin{bmatrix} 0 & 0 \\ 0 & \mathbf{S_m^{trop}} \end{bmatrix} \quad \text{5-87}$$

and for its tropospheric part

$$\mathbf{S_m^{trop}} = \left(\frac{\partial \mathbf{m}}{\partial \boldsymbol{\rho}}\right) \mathbf{S_\rho} \left(\frac{\partial \mathbf{m}}{\partial \boldsymbol{\rho}}\right)^T + \left(\mathrm{diag}(p\mathbf{m})\right)^2 \quad \text{5-88,}$$

or element-wise

$$\left(\mathbf{S_m^{trop}}\right)_{h,k} = \sum_{i=l_{tp}}^{l_{boa}} \sum_{j=l_{tp}}^{l_{boa}} \frac{\partial m_h}{\partial \rho_i} \left(\mathbf{S_\rho}\right)_{i,j} \frac{\partial m_j}{\partial \rho_k} + \left(p^2 \cdot m_h^2\right)\delta_{hk} \quad \text{5-89.}$$
$$\text{for } h,k \text{ in } \{l_{tp}, \ldots, l_{boa}\}$$

The matrix $\mathbf{S_\rho}$ is 3x3 covariance matrix of the GSR parameters ρ = (k, k_1, k_2) over land and ρ = (σ^2, δ_{Fr}, a_0) over water. The matrix $\partial\mathbf{m}/\partial\boldsymbol{\rho}$ is the l *x 3* matrix of derivatives of tropospheric box air mass factors to each of the BRF coefficients. These derivatives are determined by numerical differentiation in the look-up table of box air mass factors.

Finally, we also give the expressions for the propagated error in the DOAS total vertical column $N_v^{DOAS} = \widehat{N}_v = \left(N_s^{fit} - A^{stripe}\right)/M$:

$$\left(\sigma_{N_v^{DOAS}}\right)^2 = \left(\sigma_{\widehat{N}_v}\right)^2 = \quad \text{5-90,}$$
$$\left(\frac{\sigma_{N_s^{fit}}}{M}\right)^2 + \left(\frac{\sigma_{A^{stripe}}}{M}\right)^2 + \left(\frac{\partial \widehat{N}_v}{\partial \mathbf{N_v}}\right) \mathbf{S_{N_v^*}} \left(\frac{\partial \widehat{N}_v}{\partial \mathbf{N_v}}\right)^T + \left(\frac{\partial \widehat{N}_v}{\partial \mathbf{T}}\right) \mathbf{S_T} \left(\frac{\partial \widehat{N}_v}{\partial \mathbf{T}}\right)^T$$
$$+ \left(\frac{\partial \widehat{N}_v}{\partial \mathbf{m}}\right) \mathbf{S_m} \left(\frac{\partial \widehat{N}_v}{\partial \mathbf{m}}\right)^T$$

where the derivatives are given by

$$\frac{\partial \widehat{N}_v}{\partial \mathbf{N_v}} = \left[-\frac{\widehat{N}_v}{N_v^*} \cdot \left(\frac{m_l \cdot c_l^T}{M} - 1\right)\right]$$
$$\frac{\partial \widehat{N}_v}{\partial \mathbf{T}} = \left[\frac{\widehat{N}_v}{N_v^*} \left(\frac{m_l \cdot a \cdot N_{v,l}^*}{M}\right)\right] \quad \text{5-91}$$
$$\frac{\partial \widehat{N}_v}{\partial \mathbf{m}} = \left[-\frac{\widehat{N}_v}{N_v^*} \left(\frac{c_l^T \cdot N_{v,l}^*}{M}\right)\right]$$

and the index runs over all vertical levels $l \in \{l_{toa}, \ldots, l_{boa}\}$.

In conclusion, here we have described the framework of an error analysis for the tropospheric and DOAS total NO_2 column. The mathematical operations are relatively straightforward although somewhat tedious. An advantage however is that we use the a priori profiles in the error analysis. The accuracy of the error analysis depends on the accuracy of the estimates of the error sources. These estimates will change in the course of the development of the retrievals and also after launch. It needs to be further investigated whether the approach described above will provide more accurate error estimates than current simplified approaches. In principle, not only tropospheric columns but also their errors would need to be validated.

5.6.3 Averaging kernels and smoothing errors

In the previous section, we have derived expressions for the total uncertainty in the tropospheric vertical column and in the DOAS total vertical column by identifying the various error sources and mapping the corresponding uncertainties to an uncertainty in the retrieved quantity. The error propagation can also be framed in terms of the more formal error analysis described for example in Rodgers (2000). There, a distinction is made between so-called smoothing errors, model parameter errors, forward model errors and measurement noise errors. The uncertainty estimates of the previous section derived for the specific case of the NO_2 retrieval comprise all four error categories. For certain applications of the NO_2 product, however, an uncertainty estimate excluding the smoothing error is needed.

Focussing on the tropospheric column, we show that the smoothing error can be recognized in the third error term in Equation 5-85, $\left(\partial \widehat{N}_v^{trop}/\partial \mathbf{N_v^{trop}}\right)\mathbf{S}_{\mathbf{N_v^{*,trop}}}\left(\partial \widehat{N}_v^{trop}/\partial \mathbf{N_v^{trop}}\right)^T$. Note that we are now only considering tropospheric levels. We first re-write this error term as a random variable as

$$\epsilon_{\widehat{N}_v^{trop}} = N_v^{trop} - \widehat{N}_v^{trop} = -\frac{\widehat{N}_v^{trop}}{N_v^{*,trop}} \cdot \left(\frac{\mathbf{m}^{*,\mathrm{trop}}}{M^{trop}} - \mathbf{I}\right) \cdot \left(\mathbf{N_v^{trop}} - \mathbf{N_v^{*,trop}}\right) \quad \text{5-92}$$

where the a priori profile $\mathbf{N_v^{*,trop}}$ is our best estimate of the true profile $\mathbf{N_v^{trop}}$. It is perhaps useful at this point to state the two assumptions left implicit in the previous section: We assume that the estimator is unbiased so that it equals the geophysical ensemble mean $\mathbf{N_v^{*,trop}} = \mathcal{E}\{\mathbf{N_v^{trop}}\} = \overline{\mathbf{N}}_\mathbf{v}^{\mathrm{trop}}$, and that the error covariance matrix $\mathbf{S}_{\mathbf{N_v^{*,trop}}}$ accurately describes the covariance within this ensemble $\mathbf{S}_{\mathbf{N_v^{*,trop}}} = \mathcal{E}\left\{\left(\mathbf{N_v^{trop}} - \overline{\mathbf{N}}_\mathbf{v}^{\mathrm{trop}}\right)\left(\mathbf{N_v^{trop}} - \overline{\mathbf{N}}_\mathbf{v}^{\mathrm{trop}}\right)^{\boldsymbol{T}}\right\} = \mathbf{S}_{\mathbf{N_v^{trop}}}$.

More importantly, the derivative $\partial \widehat{N}_v^{trop}/\partial \mathbf{N_v^{trop}}$ has been evaluated at the retrieval solution, but within the context of DOAS retrievals, the linearisation point could as well be taken at the a priori profile ($\widehat{N}_v^{trop} \approx N_v^{*,trop} \approx \overline{N}_v^{trop}$) so that the first factor cancels out. ***This cannot be right… I don't yet understand this!*** Applying in addition the definition of the air mass factor, we can simplify Equation 5-92 to

$$\epsilon_{\widehat{N}_v^{trop}} = N_v^{trop} - \widehat{N}_v^{trop} = -\left(\frac{\mathbf{m}^{*,\mathrm{trop}}}{M^{trop}} - \mathbf{I}\right) \cdot \mathbf{N_v^{trop}} \quad \text{5-93}$$

Finally, using the expression for the averaging kernel derived in Section 5.6.1, we can now recognize the smoothing error as

$$\epsilon_{\widehat{N}_v^{trop}}^{smoothing} = \widehat{N}_v^{trop} - N_v^{trop} = \left(\frac{\mathbf{m}^{*,\mathrm{trop}}}{M^{trop}} - \mathbf{I}\right) \cdot \mathbf{N_v^{trop}} = \left(\mathbf{A}^{\mathrm{trop}} - \mathbf{I}\right) \cdot \mathbf{N_v^{trop}} \quad \text{5-94}$$

Here, we have followed the exact definition of the smoothing error given in Rodgers (2000), which explains the introduction of the minus sign. The variance of this error then is

$$\left(\sigma_{\widehat{N}_v^{trop}}^{smoothing}\right)^2 = \left(\frac{\mathbf{m}^{*,\mathrm{trop}}}{M^{trop}} - \mathbf{I}\right) \cdot \mathbf{S}_{\mathbf{N}_\mathbf{v}^{*,\mathrm{trop}}} \cdot \left(\frac{\mathbf{m}^{*,\mathrm{trop}}}{M^{trop}} - \mathbf{I}\right)^T = (\mathbf{A}^{\mathrm{trop}} - \mathbf{I}) \cdot \mathbf{S}_{\mathbf{N}_\mathbf{v}^{*,\mathrm{trop}}} \cdot (\mathbf{A}^{\mathrm{trop}} - \mathbf{I})^T \quad \text{5-95}$$

For completeness, we also give the expression for the smoothing error in the total column,

$$\epsilon_{N_v^{DOAS}}^{smoothing} = \epsilon_{\widehat{N}_v}^{smoothing} = \widehat{N}_v - N_v = (\mathbf{A} - \mathbf{I}) \cdot \mathbf{N}_\mathrm{v} \quad \text{5-96}$$

and its variance

$$\left(\sigma_{N_v^{DOAS}}^{smoothing}\right)^2 = \left(\sigma_{\widehat{N}_v}^{smoothing}\right)^2 = \left(\frac{\mathbf{m}^*}{M} - \mathbf{I}\right) \cdot \mathbf{S}_{\mathbf{N}_\mathbf{v}^*} \cdot \left(\frac{\mathbf{m}^*}{M} - \mathbf{I}\right)^T = (\mathbf{A} - \mathbf{I}) \cdot \mathbf{S}_{\mathbf{N}_\mathbf{v}^*} \cdot (\mathbf{A} - \mathbf{I})^T \quad \text{5-97}$$

For both the tropospheric vertical column and the DOAS total vertical column, the total uncertainty described in the previous section and the uncertainty excluding the smoothing error will be reported in the output product. The uncertainty excluding the smoothing error is calculated by setting $\mathbf{S}_{\mathbf{N}_\mathbf{v}^*}^{\mathrm{trop}}$ or $\mathbf{S}_{\mathbf{N}_\mathbf{v}^*}$ to zero. We remark that the a priori profile is used for both the air mass factor calculation and the stratospheric correction. Since tropospheric and stratospheric levels are in principle correlated, the smoothing error in the tropospheric vertical column and the error in the stratospheric correction may be correlated as well. In general, the error terms thus do not add quadratically,

$$\left(\sigma_{\widehat{N}_v^{trop}}\right)^2 \neq \left(\sigma_{\widehat{N}_v^{trop}}^{smoothing}\right)^2 + \left(\sigma_{\widehat{N}_v^{trop}}^{other}\right)^2 \quad \text{5-98}$$

but covariance terms should be taken into account, as can also be seen in Equation 5-85.

5.7 Corrections for instrument or model errors

5.7.1 De-striping of slant columns

Treatment of systematic calibration errors in sun-normalized radiances that vary quasi-randomly in the across-track direction but are relatively constant in time has been discussed in Section 5.4.

5.7.2 Scene heterogeneity

When discussing treatment of the finite spectral resolution of the instrument in Section 5.2.1, we have assumed that the instrument spectral response functions for the radiance and irradiance measurements are the same. In principle, the two response functions may be different because optical paths are slightly different, but this is not expected. The radiance response function may however change over time due to temperature effects and inhomogeneous illumination of the slit. The temperature of the optical bench is controlled to avoid strong changes of the radiance ISRF during the day and inhomogeneous illumination conditions are probably more important, if present. The change of the actual radiance ISRF compared to the nominal ISRF as it is determined during on-ground calibration is hard to predict. The location, width, shape and symmetry of the response function may all change, depending on the across-slit radiance distribution during integration and on the spectrometer characteristics. In a general sense, one would expect the ISRF to become narrower (see also [RD05]). Based on experience with current sensors and on the sensitivity study for S4 from Noël et al. (2012), we expect that the effects of inhomogeneous illumination will mostly be captured by fitting a shift and stretch in the radiance wavelength calibration. This is the baseline approach of the S4 NO_2 algorithm to dealing with scene heterogeneity.

Nevertheless, we will briefly revisit the assumption of equal radiance and irradiance instrument response functions to see how the DOAS fit is affected when this assumption is not met. Starting again from Equation 5-11, this time allowing the two ISRFs to differ, and substituting Equation 5-8, this time allowing the slant column densities to depend smoothly on wavelength, we get for the measured sun-normalized radiance

$$\frac{\tilde{I}(\lambda_i)}{\tilde{E}_0(\lambda_i)} = \frac{\int S_{het}(\lambda_i,\lambda)E_0(\lambda)\sum_p c_p\lambda^p\left(1-\sum_j N_{s,j}(\lambda)\sigma_j(\lambda)\right)d\lambda}{\int S_{nom}(\lambda_i,\lambda)E_0(\lambda)d\lambda} \quad \text{5-99.}$$

Here, S_{het} and S_{nom} are the distorted ISRF and the nominal ISRF, respectively. Assuming that the polynomial and the slant column densities are constant across the wavelength range of the integration, we can write

$$\frac{\tilde{I}(\lambda_i)}{\tilde{E}_0(\lambda_i)} = \sum_p c_p\lambda_i^p\left(\frac{\int S_{het}(\lambda_i,\lambda)E_0(\lambda)d\lambda}{\int S_{nom}(\lambda_i,\lambda)E_0(\lambda)d\lambda} - \sum_j N_{s,j}(\lambda_i)\tilde{\sigma}_j(\lambda_i)\right) \quad \text{5-100,}$$

where the absorption cross-sections after convolution are given by

$$\tilde{\sigma}(\lambda_i) = \frac{\int S_{het}(\lambda_i,\lambda)E_0(\lambda)\sigma(\lambda)d\lambda}{\int S_{nom}(\lambda_i,\lambda)E_0(\lambda)d\lambda} \quad \text{5-101.}$$

Finally, we write

$$\frac{\int S_{het}(\lambda_i,\lambda)E_0(\lambda)d\lambda}{\int S_{nom}(\lambda_i,\lambda)E_0(\lambda)d\lambda} = 1 + \left(\frac{\int S_{het}(\lambda_i,\lambda)E_0(\lambda)d\lambda}{\int S_{nom}(\lambda_i,\lambda)E_0(\lambda)d\lambda}\right)_{diff} \quad \text{5-102.}$$

In absence of Fraunhofer structures, the second term is zero, while in the presence of (strong) Fraunhofer lines and for differing radiance and irradiance spectral response functions, as in the case of inhomogeneous slit illumination, the second term is non-zero and varies with wavelength. This term can be considered a pseudo-absorber. Thus, when the radiance and irradiance response functions differ, two effects occur that are related to the solar spectrum (Equation 5-102) and the absorption cross-sections (Equation 5-101).

In the baseline implementation, no correction is included for heterogeneous scenes, but the corresponding warning flag from the cloud product is forwarded in the product, and the qa_value reduced in case it is raised.

5.7.3 Thermal variation of ISRFs in orbit

Knowledge of the shape of the ISRF may to some degree be inaccurate even under homogeneous illumination conditions. These inaccuracies can result from effects such as inaccurate on-ground characterisation, changes in ISRFs from ground to orbit, instrument degradation, or perhaps systematic errors introduced by spectral and spatial interpolation of the calibrated ISRFs to the target CCD pixel. As briefly mentioned above, in-flight variation due to temperature effects assuming that knowledge of the temperature of the optical bench and the ISRFs' temperature dependence is not taken into account may also contribute.

A small sensitivity test for S4 instrument settings on the impact of temperature effects is reported in Section 7.3.1. This test indicates that ignoring the ISRF's temperature dependence will introduce a non-negligible but small error. The largest errors are observed when the ISRFs for the radiance and irradiance measurements are indeed at different temperatures. We estimate that the systematic error in the fitted NO_2 slant column will be at most 2% for a tropospheric pollution scenario in case of a 1ºC temperature difference. It should be noted however that the thermal stability of the optical bench is expected to be on the order of 0.1ºC.

5.7.4 Spectral mis-registration of radiance and irradiance

One of the strengths of fitting reflectance, which is a ratio of two measurements performed by the same instrument, is the fact that it leads to a large degree of cancellation of instrumental effects and also efficiently removes the spectral structure of the solar irradiance from the signal. Ideally, the instrument performs in exactly the same way for both measurements, leading to perfect cancellation of Fraunhofer lines, multiplicative calibration errors, and radiometric degradation.

In reality, several differences between the two measurements exist, which limits the accuracy of the cancellation. These differences include the slightly different optical paths in the instrument (e.g. a solar diffuser is part of the optical path for the irradiance measurement and a polarisation scrambler is part of the optical path for the radiance measurement), slightly different instrument spectral response functions between irradiance and radiance measurement (e.g. due to different temperatures of the optical bench or inhomogeneous slit illuminations during the radiance measurement), and a difference in wavelength mapping on the CCD (i.e. the same wavelength is mapped to different physical CCD columns in the radiance and irradiance measurement). The latter is linked to mechanical stress in the optical bench resulting from temperature changes during the measurement cycle. This spectral mis-registration for S4 has been estimated to be about 15% of the spectral sampling interval in the UVis channel (i.e. 15% of 0.5 nm / 3). Within a 24-h measurement cycle, the wavelength assignment of a particular CCD column is relatively stable: the position of spectral channels of the radiance measurement in the UVis is expected to not vary more than 5% of the spectral sampling interval between two consecutive irradiance measurements. Note that the wavelength registration of the CCD columns depends in turn on the CCD row (spectral smile).

The shift in spectral registration of the CCD columns between the radiance and irradiance measurement has three effects: (i) spectral interpolation is needed to map irradiance and radiance onto the same wavelength grid as is necessary for computation of the reflectance (Section 5.2.3) and this creates pseudo-noise, (ii) calibration errors will not cancel out perfectly as they typically also vary across CCD pixels (e.g. pixel response non-uniformities), and (iii) interpolation of calibration functions on different wavelength grids will introduce pseudo-noise on the ratio of calibrated spectra. It should be pointed out however that even if the wavelength mapping for the radiance and irradiance measurements would be perfectly the same, the wavelength axes of the two are still misaligned due to the correction for the Doppler shift in the irradiance measurement causing all three effects just described.

As discussed in Section 5.2.3, the NO_2 algorithm uses the optimised solar irradiance wavelength grid as the grid for the DOAS fit and the radiances are first interpolated onto this grid. As the spectral sampling ratio of S4 is only three, any interpolation of the wavelength axis will introduce noise in the reflectance, further increasing the overall uncertainty. This effect can be reduced by introduction of an undersampling spectrum (Chance et al., 2005) or perhaps by using information on sub-pixel structures of the spectrum from the Fraunhofer atlas during the interpolation. Both approaches are possible future developments.

Experience with data from previous satellite missions shows that the effect of small differences in spectral mapping on NO_2 columns are small and the main problem is an increase of the fit residuals and thus the reported NO_2 slant column precision. Depending on the detailed spectral shape of calibration functions, an impact on NO_2 columns can however not be fully excluded.

5.7.5 Intra-band and inter-band spatial mis-registration

Possible intra-band spatial mis-registration will be predominantly in the N-S direction: mis-registration in the E-W direction can be compensated for by an appropriate timing of the read-outs of the UVis and NIR CCDs. The amplitude of the intra-band mis-registration in the UVis channel is currently estimated to be about 15% of the Spatial Sampling Distance (SSD). The mis-registration varies smoothly (low-order polynomial) across the NO_2 spectral domain. The UVis channel covers the wavelength range between about 310 and 500 nm, while the NO_2 fit window lies between about 425 and 500 nm. For a displacement varying linearly across the band, the mis-registration between the first and the last spectral channel of the NO_2 fit window would be about 6% of the SSD.

Inter-band misregistration (0.2 SSD between UVis and NIR): affects accuracy of support cloud product; interpolation between UVis and NIR bands using data from FCI…

5.7.6 Polarisation sensitivity

While solar radiation is in good approximation unpolarised, the radiance scattered by the atmosphere-surface system can have varying degrees of polarisation depending on scattering angle, surface reflectivity, aerosol loading, and cloudiness. As a result, the polarisation sensitivity of the instrument affects the measured intensity and can lead to a selection of specific light paths through the atmosphere (for example, polarised Rayleigh-scattered light may be seen with higher sensitivity). This presents a problem in case the polarisation state of the light entering the instrument is unknown. Even for unpolarised light optical components in the instrument may introduce polarisation effects when they have different efficiencies for the two linear polarisation directions comprising the unpolarised radiation field (for example reflection by mirrors), although the instrument is supposedly accurately radiometrically calibrated for unpolarised light on ground.

In some instruments, such as GOME, SCIAMACHY and GOME-2, the polarisation state of the incoming radiance was (is) measured by dedicated polarisation measuring devices (PMD) and the effect of the instrument's polarisation sensitivity on the measurement is corrected in the Level-1b processor. However, this led to problems because neither the polarisation measurement nor the calibration of the instrument's polarisation sensitivity were sufficiently accurate. For OMI, S5P and also S4, a different approach is taken by using polarisation scramblers and assuming that the light entering the spectrometer is unpolarised. Also in this case, residual signatures of the instrument's polarisation sensitivity have to be expected that depend on the (unknown) polarisation state of the incoming radiance.

For DOAS retrievals, uncertainties in retrieved slant columns can be introduced if the wavelength dependence of the instrument's polarisation sensitivity is partly parallel to the absorption cross-section of the target trace gas. For NO_2 from GOME and SCIAMACHY, this was the case at wavelengths larger than 460 nm, which basically limited the usable wavelength window to this upper limit. The wavelength dependence of the instrument's polarisation sensitivity as characterised during on ground calibration can in principle be used to generate additional pseudo-absorber cross-sections for the DOAS fit. This may help to reduce the impact of polarisation on the retrieval, but pseudo-absorber cross-sections need to be again sufficiently orthogonal to other cross-sections. For GOME and SCIAMACHY it was found that this approach could not fully compensate for the calibration issues. Reasons were the intrinsic spectral correlation between the correction function and the NO_2 cross-section as mentioned above as well as changes in the polarisation sensitivity of the instrument over time.

The UVN instrument is designed to be relatively polarisation insensitive and a polarisation scrambler is used to de-polarize the incoming light. For S4, the residual polarisation sensitivity is therefore expected to be small, and no polarisation correction is foreseen in the baseline implementation.

5.8 Future Developments

Many different future developments can be envisaged, which have the potential to reduce the uncertainties of the S4 NO_2 product or to improve computational performance. In the following, some of these possible developments are briefly described.

5.8.1 DOAS fitting

In the current implementation, the DOAS fit for the wavelength adjustment is non-linear. Alternatively, the linearised wavelength calibration following the approach of Beirle et al., 2013 could be used, which reduces computational costs.

As discussed previously, the DOAS fit currently does not use error weighting. This could be changed in future versions, depending on test results on real S4 data, potential leading to more stable fits and better uncertainty characterisation.

5.8.2 Scene heterogeneity

In order to further improve on the quality of the retrievals for inhomogeneous scenes, additional pseudo-absorbers could be included in the DOAS fit. For existing instruments, a simple correction spectrum simulating the effect of a change in ISRF width has been successfully used, resulting in reduced fitting residuals (Alvarado, 2016). A more empirical approach is based on a PCA analysis of the fitting residuals. Including two (OMI, TROPOMI) or 4 (GEMS) additional cross-sections in the fit largely reduces the fitting residuals for those instruments and improves the scatter of the NO_2 columns (see example in Figure 5.11). Whether this is also necessary and possible for S4 will have to be tested on real S4 data.

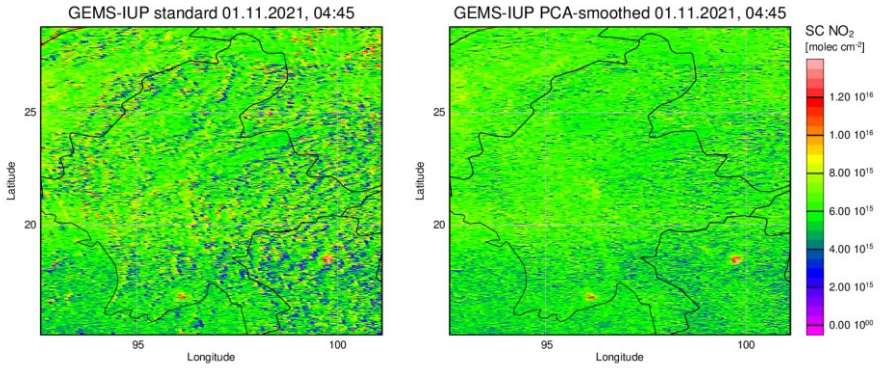

Figure 5.11: Example of the effect of including 4 PCA components for the correction of inhomogeneous scene effects in GEMS-IUP data. Shown is the standard evaluation without PCA components (left) and the improved one including all 4 PCA components (right). There is a marked reduction in the scatter of the NO_2 slant columns.

5.8.3 Spectral mis-registration

As discussed in Section 5.2.3, the NO_2 algorithm uses the optimised solar irradiance wavelength grid as the grid for the DOAS fit and the radiances are first interpolated onto this grid. As the spectral sampling ratio of S4 is only three, any interpolation of the wavelength axis will introduce spectral noise in the reflectance, increasing the overall uncertainty. This effect can be reduced by introduction of an undersampling spectrum as additional cross-section (Chance et al., 2005). Based on the results obtained during the S4 commissioning phase, it can be decided whether or not to include such an undersampling correction in the fit.

5.8.4 Polarisation sensitivity

S4 calibration results indicate a possible non-compliancy of the polarisation sensitivity of the instrument affecting the NO_2 retrieval spectral range. Simple tests performed on the expected maximum polarisation results as derived in [RD22] show that the size and correlation of the expected polarisation features with the NO_2 absorption cross-section is large enough to create uncertainties exceeding the expected noise. If these results are confirmed in real radiance data, one or more correction cross-sections will have to be included in the fit.

The polarisation state of the light reaching the sensor is described with respect to an atmospheric reference frame. Ignoring circular polarisation and choosing the atmospheric reference frame such that the polarized component is parallel, the incident Stokes vector is $\mathbf{I}^T = (I, Q, 0, 0) = (I, \mu I, 0, 0)$, where $\mu = Q/I$ is the degree of linear polarisation ($0 \leq \mu \leq 1$). The uncalibrated intensity measured by a polarisation-sensitive instrument is then given by

$$\tilde{I}_{uncal}(\lambda_i) = \int S(\lambda_i, \lambda)\{M_{1,1}(\lambda) \cdot I(\lambda) + M_{1,2}(\lambda) \cdot Q(\lambda) \cdot \cos 2\alpha(\lambda) + M_{1,3}(\lambda) \cdot -Q(\lambda) \cdot \sin 2\alpha(\lambda)\} d\lambda \approx M_{1,1}(\lambda) \int S(\lambda_i, \lambda) \left\{ I(\lambda) + \frac{M_{1,2}(\lambda)}{M_{1,1}(\lambda)} \cdot Q(\lambda) \cdot \cos 2\alpha(\lambda) + \frac{M_{1,3}(\lambda)}{M_{1,1}(\lambda)} \cdot -Q(\lambda) \cdot \sin 2\alpha(\lambda) \right\} d\lambda \quad \text{5-103,}$$

where $M_{i,j}$ are elements of the instrument's Müller matrix in the instrument's frame of reference and α is the angle of rotation between the atmospheric and instrument reference frames. For our particular choice of the atmospheric reference frame, α now becomes the angle of polarisation. Here we assume that the instrument's end-to-end Müller matrix and the Instrument Spectral Response Function are defined such that first multiplication with the Müller matrix is performed and then convolution with the response function. When we assume in addition that the instrument is radiometrically calibrated for unpolarised light (i.e. $\tilde{I}(\lambda_i) = \tilde{I}_{uncal}(\lambda_i)/M_{1,1}(\lambda)$), the second and third term of Equation 5-104 constitute a radiometric calibration error due to the instrument's polarisation sensitivity

For the particular case of the NO_2 retrieval, we furthermore assume that the degree and angle of linear polarisation of the radiance vary smoothly across the fit window. Then pseudo-absorber cross-sections may be constructed from an accurate calibration measurement of the instrument's Müller matrix elements $M_{1,2}(\lambda)$ and $M_{1,3}(\lambda)$ as

$$\tilde{\sigma}(\lambda_i) = \frac{\int S(\lambda_i, \lambda) \frac{M_{1,2}(\lambda)}{M_{1,1}(\lambda)} E_0(\lambda) d\lambda}{\int S(\lambda_i, \lambda) E_0(\lambda) d\lambda} \quad \text{5-104}$$

and

$$\tilde{\sigma}(\lambda_i) = \frac{\int S(\lambda_i, \lambda) \frac{M_{1,3}(\lambda)}{M_{1,1}(\lambda)} E_0(\lambda) d\lambda}{\int S(\lambda_i, \lambda) E_0(\lambda) d\lambda} \quad \text{5-105}$$

(derivation not shown). The degree and angle of linear polarisation are expected to be smoothly wavelength dependent because the absorbers in the NO_2 fit window are weak. Spectral features related to the instrument's polarisation sensitivity may, however, occur at the position of strong Fraunhofer lines. The benefit of this mitigation approach depends on the spectral structure of elements $M_{1,2}(\lambda)$ and $M_{1,3}(\lambda)$ and the accuracy of their calibration measurements.

5.8.5 AMF calculation

The baseline implementation derives airmass factors from precomputed LUTs. While this is computationally efficient, it limits the number of parameters which can be taken into account. In particular the effects of aerosol scattering and directional surface reflection are difficult to include in such LUTs. Therefore, it should be investigated if online AMF calculations are feasible within the constraints of the operational ground processor.

5.8.6 Directional effects of surface reflectance

Effects of the angular dependence of the surface reflectance and its change during the day will become an important issue for S4, because of the high spatial resolution, hourly sampling and the relatively large viewing and solar zenith angles. For example, smaller ground pixels become more homogeneous and directional effects are averaged out less. BRF models as they have been developed from observations by polar-orbiting instruments (e.g. MODIS, POLDER) may be inaccurate for the large viewing and solar zenith angles that are not covered by these instruments but systematically occur in S4 observations at mid and high latitudes. More generally, the BRF for natural surfaces typically varies more pronounced towards larger zenith angles (Thomas and Stamnes, 2002). For S4, viewing zenith angles are larger towards the northern edge of the geographical coverage area and solar zenith angles are larger at the beginning and end of the day. The standard approach of assuming Lambertian surface reflection in combination with climatologies of so-called Lambertian-equivalent reflectivities derived from the same sensor may therefore not suffice anymore, and more sophisticated surface reflection models are needed. This is of particular relevance if the diurnal variation of NO_2 at a given location is to be evaluated as then BRF effects directly interfere with the retrieved diurnal profile. As a side note, recent sensitivity studies for NO_2 indicate that directional effects are reduced in the presence of aerosols (Noguchi et al., 2014).

The baseline currently foreseen in the S4 NO_2 algorithm is to use LER surface reflectance as in the heritage algorithms. This can then be updated after launch by using the BRF model and the dynamic map of BRF model coefficients as provided by the S4 L2 Gapless Surface Reflectance support product for land surfaces. Different approaches can be used to incorporate BRF effects in the air mass factors:

1. On-line calculations of air mass factors. This approach would provide full flexibility also for including aerosol effects but relies on sufficient processing power which may not be available.
2. Use of approximations of BRF effects by a Lambertian-equivalent reflectivity as for example proposed in Vasilkov et al. (2017). This approach is fast and does not need very big look-up-tables but neglects some of the BRF effects.

5.8.7 Aerosols

As a baseline, aerosols will not be taken into account explicitly although there is some implicit correction through the treatment of clouds (Boersma et al., 2011). Aerosol information will be available from the S4 surface product, but application in the AMF calculations can only be tested once a larger set of real S4 retrievals is available.

Application of this information in the air mass factors would be relatively easy in the case of online air mass factor calculations but could at least in principle also be integrated into the look-up-table approach. However, the size of these tables would probably become prohibitive.

5.8.8 Cloud Radiance fraction

Cloud radiance fraction determined from simulated radiances at the wavelength of the air mass factor using the OCRA cloud fraction, ROCINN Lambertian cloud albedo and ROCINN cloud pressure. ROCINN Lambertian cloud albedo and ROCINN cloud pressure used for the AMF of the cloudy part of the pixel.

As an alternative implementation, the Lambertian cloud albedo for the NO_2 fit window (A_c^{CHOCHO}) can recalculated from measured sun-normalized radiances at the wavelength of the air mass factor while retaining the OCRA cloud fraction. This can be written as

$$\tilde{R}\left(\lambda_0^{CHOCHO}\right) = \left(1 - f_{cld}^{OCRA}\right) R_{clr}^{sim}\left(\lambda_0^{CHOCHO}; \rho_s^{VIS}, p_s\right) + f_{cld}^{OCRA} R_{cld}^{sim}\left(\lambda_0^{CHOCHO}; A_c^{CHOCHO}, p_c^{ROC}\right) \quad \text{5-106.}$$

To reduce the effect of noise errors, the measured sun-normalized radiance ($\tilde{R}$) at λ_0^{CHOCHO} is replaced by the measured sun-normalized radiance averaged ($\bar{R}$) across 10 spectral channels around λ_0^{CHOCHO}. The same look-up tables of sun-normalized radiances as in the baseline implementation are used. Since the OCRA cloud fraction is derived from UVis radiances, this approach seems the most reasonable. Fitting the cloud albedo again for the NO_2 fit window may also help to mitigate other forward model errors.

5.8.9 Stratospheric Correction

Stratospheric correction in the baseline algorithm is based on the CAMS global forecast. As an alternative implementation, a spatial filtering technique could be applied as implemented in the NASA NO_2 processor for OMI (Bucsela et al., 2013) and refined in Beirle et al. (2016). This is basically a more sophisticated version of the reference sector approach and a chemical transport model is not needed. In the method by Bucsela et al. (2013), a model is used to select clean pixels, cloudy pixels are added to improve statistics, quality checking and removal of outliers is performed, and clean and cloudy pixels are subsequently interpolated and smoothed to create a continuous stratospheric SCD field. Hence, unpolluted pixels are selected from the entire geographic coverage area and the problem that a clear unpolluted reference sector (i.e the North Atlantic area) is in S4's field of view only during the second half of the day is partly avoided.

6 Feasibility

6.1 Processing approach

6.1.1 Overview

Algorithm flow diagrams are given in Figure 5.1 (Overview) and in Figure 5.2 (DOAS), Figure 5.4 (STRAT), Figure 5.6 (BG), Figure 5.7 (AMF) and Figure 5.9 (CLD) for the different submodules. Interfaces between the modules and data input and output fields are clearly indicated in these diagrams. The separate BG auxiliary processor is illustrated in Figure 5.5. Processing by the BG processor is time-driven, while the main processing stream by the other modules is data-driven. The ECA processor is described in detail in [RD10].

6.1.2 Level-1b data requirements

Table 6.1 gives an overview of Level-1b input data, any pre-processing needs and the static backup options in case the dynamic data are not available. The use of static backup data is of course reflected in the product's quality assurance protocol. A discussion on auxiliary data that L2 processors expect to be provided by the L1B product is summarized in [RD19].

Table 6.1. Level-1b data used in the baseline implementation of the S4 NO_2 algorithm. Rows starting with a plus-sign (**+**) describe data fields that are not needed by the NO_2 processor itself but are only used to set processing errors and warnings and / or are copied to the L2 product to increase the usability. There are separate radiance products for the UVis and NIR bands. In the table below, all fields are read from the UVVIS radiance product, unless stated otherwise.

Level-1b data	Pre-process needs	Action when missing	Comments
Radiance spectrum	Number of valid spectral channels in the fit window should pass threshold test.	No retrieval	Vis band
Time offset	-	No retrieval	
Nominal latitude and longitude of pixel centre and corners	-	No retrieval: geolocation error.	Geodetic coordinates for pixels in UVis band. Nominal geolocation is the intersection of the line-of-sight with the reference ellipsoid.
+ Terrain-corrected, PSF-weighted latitude and longitude of pixel	-	-	Geodetic coordinates for pixels in UVis band. Elevation database is GMTED2010.
VZA, VAA, SZA, SAA	-	No retrieval: geolocation error.	For pixel centres in UVis band. Angles at the reference ellipsoid (geodetic reference frame).
Daily irradiance spectrum	Number of valid spectral channels in the fit window	Use most recent previous irradiance measurement	From separate irradiance product. In nominal near real-time processing, the irradiance product is available about 15 min after sensing.

	should pass threshold test.	that passed threshold test.	
+ Terrain-corrected, PSF-weighted mean and standard deviation of the pixel's elevation	-	-	For pixels in UVis band. Source is GMTED2010 consistent with S5P. Note that elevation is above geoid (not: reference ellipsoid).
Water fraction	-	No retrieval: geolocation error.	For pixels in UVis band. Derived from land-water mask in SDP toolkit.
+ Surface classifications (land and water categories)	-	-	For pixels in UVis band. Similar approach as for S5P: land-water mask and water classifications from SDP toolkit, but with a different land classification scheme (IGBP) and more recent land classification database (MCD12Q1), see [RD19].
+ Geolocation error and warning	-	-	Used in S4 NO_2 quality assessment.
+ Solar eclipse flag (binary)	-	No retrieval: geolocation error.	Air mass factors do not apply. Used in S4 NO_2 quality assessment.
+ Sun glint flag (binary)	-	No retrieval: geolocation error.	Flag raised if sun glint angle is smaller than … deg. Sun glint angle is defined as … . In principle, sun glint is captured by the water BRF model. Flag is used in S4 NO_2 quality assessment.
+ Snow / ice flag	-	An up-to-date snow / ice climatology.	Same approach as for S5P. Source is NISE. Note that NISE snow / ice information will be at least one day old (today's parameters based on observations up to previous day). Flag distinguishes between snow-free land, snow and permanent ice (Greenland, Antarctica) for land, and several sea ice percentages for open ocean.
+ All level-1b flags: pixel quality, measurement quality, xscan quality, spatial sample quality and spectral processing flags	-	No retrieval	Used for raising errors and warnings, filtering and the quality assurance protocol.

Yaw flip status	-	No retrieval	Needed for calculation and application of the stripe offset corrections.

As a baseline, any uncertainty estimates for radiance and irradiance spectra provided in Level-1b files are not used. However, they may be read and propagated at a later stage.

L1b provides two different sources for geolocation (a) raw geolocation coordinates for the center of a pixel in the fields "latitude" and "longitude" and (b) geolocation parameters coming from the Instrument Navigation and Registration (INR) processor indicated by the tag "_inr" appended to the variable names. The ABB and L2PP/L2OP will have the flexibility to select and use (a) or (b).

6.1.3 Auxiliary data requirements

Table 6.2 gives an overview of static auxiliary data, their source and pre-processing needs. Several static data sets are input to more than one S4 L2 processor and preferably a common approach is taken (see Section 6.1.6).

Table 6.2. Static auxiliary data used in the baseline implementation of the S4 NO_2 algorithm. *This table is in progress and variables may be added or removed in the course of L2 development.*

Auxiliary data	**Source**	**Pre-process needs**	**Comments**
Absorption cross-sections of absorbers; Ring cross-section	Literature and SCIATRAN (Ring)	Convolution with nominal S4 ISRFs (per row).	For details, see Table 5.1 and Section 5.2.2.
High-sampling solar irradiance reference spectrum	Chance and Kurucz (2010)	Convolution with nominal S4 ISRFs (per row).	
Nominal instrument spectral response functions (per row)	S4 calibration data	-	
Instrument's polarisation sensitivity (normalised Müller matrix elements $M_{1,2}(\lambda)/M_{1,1}(\lambda)$ and $M_{1,3}(\lambda)/M_{1,1}(\lambda)$)	S4 calibration data	Convolution with nominal S4 ISRFs (per row).	For details, see Section 5.7.6.
Several look-up tables	SCIATRAN	-	(1) BAMF over land, (2) BAMF over water, (3) radiance over land, (4) radiance over water.

Table 6.3 gives an overview of dynamic auxiliary data, their source, pre-processing needs and the static backup option in case the dynamic data are temporarily not available. The use of static backup data is of course reflected in the product's quality assurance protocol. Several dynamic data sets are input to more than one S4 L2 processor and preferably a common approach is taken (see Section 6.1.6).

Table 6.3. Dynamic auxiliary data used in the baseline implementation of the S4 NO_2 algorithm. Rows starting with a plus-sign (**+**) describe data fields that are not needed by the NO_2 processor itself but are only used to set processing errors and warnings and / or are copied to the L2 product to increase the usability.

Auxiliary data	**Source**	**Pre-process needs**	**Action when missing**	**Comments**
Surface reflection parameters (land and water)	S4 L2 Gapless Surface Reflectance support product (S4-L2-GSR)	Nearest-neighbour interpolation from static SUR / GSR L1c grid to variable L1b pixel grid (in UVis band) as described in the SUR / GSR ATBD ([RD06]). For mixed land-water pixels, the BRF model of the dominant surface type is taken.	No static backup needed. Map of BRF coefficients provided by GSR is gap-filled with older retrievals or climatological values.	BRF parameter values for the SUR wavelength closest to the wavelength of the air mass factor are used (e.g. SUR wavelength 457 nm). Note that SUR / GSR parameters will be at least one day old (today's product based on observation up to the previous day).
NO_2 and T profiles, surface pressure and tropopause layer index	In the operational processors, forecasts are taken from CAMS Global and CAMS Regional. Pre-processing of model data performed by separate	Parameters are provided by the ECA engineering product for the geolocation and time of the S4 observation. Additional pre-processing by the NO_2 processor is needed to split the	No static backup needed. In case, the current forecast is missing, the ECA product provides older forecasts or climatological profiles.	Data fields are read from the ECA product for pixels in the UVis band. For a detailed description of the necessary pre-processing steps performed by the ECA processor, see [RD10].

	ECA processor ([RD10]). Data fields are read by the NO_2 processor from the S4 ECA engineering product (S4-RI-ECA).	profile into a tropospheric and stratospheric part based on the tropopause layer index (l_{tp}) and to correct the stratospheric part for spatial and temporal model biases.		
Cloud parameters (fraction, height, Lambertian albedo)	S4 L2 Cloud product (S4-L2-CLD)	-	Stop processing after de-striping of fitted slant columns.	Cloud parameters for the UVis pixel grid are read.
+ Scene heterogeneity	S4 L2 Cloud product (S4-L2-CLD)	-	Assume homogeneous scene.	heterogeneous_scene_warning and small_pixel_standard_deviation are read for quality flagging
+ UV Aerosol Index	S4 L2 product (S4-L2-UAI)	-	-	
+ Boundary layer height	Forecasts provided by ECMWF. Pre-processing performed by separate ECA processor (S4-RI-ECA).	Same pre-processing as other model data.	No static backup needed. In case, the current forecast is missing, the ECA product provides older forecasts or climatological values.	Data fields are read from the ECA product for pixels in the UVis band. For a detailed description of the necessary pre-processing steps performed by the ECA processor, see [RD10].

6.1.4 Dependence on other Level-2 products

The two main Level-2 support products that contain input for the S4 NO_2 retrieval are the S4 L2 Cloud and the S4 L2 Gapless Surface Reflectance products. The scene heterogeneity flag from the S4 HSC algorithm provided in the Cloud product is used for quality assessment. Furthermore, pre-processed model data are read from the ECMWF-CAMS (ECA) engineering product ([RD10]). The main processor also needs the NO_2 Background engineering product. Finally, the UVAI from the corresponding L2 product is read by the NO_2 processor and passed on into the NO_2 output product. Table 6.4 summarizes these S4 L2 input products.

Table 6.4. Overview of Sentinel-4 Level-2 products that contain input for the S4 NO_2 processor. We have also explicitly indicated the main variables read from these products.

***Name* / variable**	**Product**	**Comments**
Cloud	S4-L2-CLD	
cloud_fraction_crb_uvvis		
cloud_pressure_crb_uvvis		
cloud_albedo_crb_uvvis		
Gapless Surface Reflectance	S4-L2-GSR	
gapless_bidirectional_reflectance_factor_land_parameter1		
gapless_bidirectional_reflectance_factor_land_parameter2		
gapless_bidirectional_reflectance_factor_land_parameter3		
gapless_bidirectional_reflectance_factor_ocean_parameter1		
gapless_bidirectional_reflectance_factor_ocean_parameter2		
gapless_bidirectional_reflectance_factor_ocean_parameter3		
Heterogeneous Scene Correction	S4-L2-CLD	Heterogeneity parameters stored in Cloud product
heterogeneous_scene_warning		
UV Aerosol Index	S4-L2-UAI	
aerosol_index_340_380		
Background correction for NO_2	S4-BG-NO2	
see Section 6.1.5		
Pre-processed ECMWF-CAMS model data	S4-RI-ECA	ECMWF / CAMS Global / CAMS Regional
constant_a_interface		
constant_b_interface		
constant_a_middle		
constant_b_middle		
temperature_uvvis		
surface_pressure_uvvis		

tropopause_layer_index_uvvis		
nitrogendioxide_partial_columns_uvvis		
boundary_layer_height_uvvis		
aerosol_volume_scattering_coefficient_at_440nm_uvvis		
aerosol_volume_absorption_coefficient_at_440nm_uvvis		
aerosol_optical_thickness_at_550nm_uvvis		

6.1.5 BG engineering product

The layout of the BG module is currently under discussion. A BG engineering product file is produced once per day during the night. It contains stripe patterns and model bias patterns to be used for corrections on the coming day. Table 6.5 describes the data fields in the BG engineering product. The total size of the daily BG engineering product is very small.

Table 6.5. Overview of data fields in the BG auxiliary product.

Variable name	Symb.	Source	Unit	Comment / description	Type	Dims.
stripe_offset	$A(y)$	Proc.	mol m^{-2}	Stripe offset for each across-track pixel.	f32	ground_pixel
model_bias	$c(t_{sol}, \delta_{geo})$	Proc.	mol m^{-2}	Bias in the modelled vertical column as a function of local solar time and latitude. Dimension spacing is for example, for example, 1 h and 5°.	f32	solar_time x latitude

It seems important to strictly follow the ground_pixel dimension from the L1b product to avoid potential confusion around the yaw flip.

6.1.6 Common processor elements

As the NO_2 retrieval is a standard DOAS retrieval, a large potential for common use of processor elements exists in particular between the NO_2, SO_2 and HCHO retrievals. Table 6.6 gives a detailed list of common processing steps for which a single software module could be developed.

Table 6.6. Common processing steps for the NO_2, HCHO, CHOCHO and SO_2 retrievals.

Processor element /algorithmic feature	NO_2	HCHO	CHOCHO	SO_2	Comments
S4 L1, L2 input /output routines	y	y	y	y	
S4 L2 products interface CLD, SUR, GSR	y	y	y	y	
S4 L2 product interface OTO	n	n	n	y	
S4 L2 product interface	y	y	y	y	only passed to L2 files

UAI					
S4 RI ECA processor interface	y	y	y	y	Separate processor to deliver all required model parameters at S4 pixel level to all DOAS trace gases processors
DOAS spectral fitting					
Reference database	y	y	y	y	Absorption and pseudo cross-sections, solar atlas, ISRF
ISRF convolution	y	y	y	y	Add options for different approaches e.g. solar-Io
Wavelength calibration / ISRF fitting	y/n	y/y	y/n	y/y	Not identical but similar in concept. No objections for NO2 and CHOCHO to also use ISRF fitting
Spike removal	y	y	y	y	
Offset correction	y	y	y	y	Linear correction (1/Io)
Solar reference spectrum	y	y	y	y	SO2 & HCHO: averaged earth-shine radiance as reference (optional).
Ring pseudo cross sections	y	y	y	y	There are differences in construction of Ring xsecs between DOAS retrievals.
Optical depth fitting	y	y	y	y	Identical or nearly identical
Linear Shift & stretch with apriori from previous obs.	n	n	n	n	Currently non-linear approach as baseline
HSC correction	n	n	n	n	If necessary and in case pseudo-cross sections are provided by HSC or constructed by the DOAS algorithms themselves.
Multiple windows	n	y	n	y	SO2: 3 independent windows HCHO: 2 linked windows
Stratospheric correction	y	n	n	n	
Background/destriping correction (engineering products)					
Fitted SCDs	y	y	y	y	SO2 : SCDs all windows+O3 SCDs
Cloud screening and hotspot masking	y	y	y	n	NO2 selects cloudy or unpolluted pixels for the BG correction, HCHO selects clear unpolluted pixels
AMFs+model VCDs	y	y	n	n	From historic L2 files.
Historic engineering files	y	y	y	y	NO2: last available day HCHO: last available day. CHOCHO: last available day. SO2: last available two weeks
Air mass factors					

LUT database	y	y	y	y	NO2 and CHOCHO: bAMFand radiance HCHO & SO2: bAMFs+radiance+Jacobians
AMF module, including interpolation and cloud correction	y	y	y	y	Identical or nearly identical
T correction	y	n	n	y	Similar in concept
Averaging kernel output	y	y	y	y	
CAMS trace gas profile	y	y	y	y	SO2: CAMS+3 predefined box profiles fall-back covered by ECA
Surface height from S4-L1B	y	y	y	y	
BRF	y	(y)	(y)	(y)	All trace gases: different treatment of ocean and land surfaces. NO2 and CHOCHO: full BRF HCHO & SO2: simplified treatment, e.g. WSA based on retrieved BRF parameters All trace gases: fall-back is LER climatology
Total ozone column	n	n	n	y	
Explicit aerosols correction	n	n	n	n	Possible future evolution
Calculation of cloud parameters for the fit window	y	n	y	n	Common approach to calculate appropriate cloud fraction and albedo for the fit window
Error analysis module					
Distinction between (quasi) random & systematic errors	n	y	n	y	
Uncorrelated sources of errors	y	y	y	y	possible future evolution
SCDE : instrument noise propagation	y	y	y	y	Direct output of DOAS module (fit RMS propagated to a SCD error).
SCD systematic error	y	y	y	y	SO2 and HCHO: trivial formulation. To be refined
Stratospheric correction error	n	n	n	n	
Background correction	y	y	y	y	
AMF error	y	y	y	y	NO2, SO2, HCHO, CHOCHO: uncorrelated error sources. Calculations based on simple Jacobians and fixed auxiliary

					data errors. SO2 profile errors described with a single parameter.

6.1.7 Pixel selection

Under normal conditions (no errors and warnings), the following pixels are selected for processing:

Slant column fit (DOAS)

Slant columns will in principle always be fitted. Ground pixels that are in a solar eclipse situation are excluded from processing, but this happens rarely. Furthermore, the viewing zenith angle should be smaller than 90° and the solar zenith angle smaller than 95° (angles at the reference ellipsoid).

Air mass factor calculation (AMF)

Calculation of tropospheric air mass factors and subsequent processing steps are cut off at solar zenith angles and viewing zenith angles larger than 85° (angles at the reference ellipsoid).

6.1.8 Configurable parameters

In this section, we give lists of parameters that should be configurable in order for algorithm maintainers to be able to fine-tune the algorithm (possibly after launch) and achieve the best possible algorithm accuracy. Table 6.7 describes parameters for the main NO_2 processor and Table 6.8 for the BG auxiliary processor.

Table 6.7. List of configurable parameters for the NO_2 processor.

Parameter	Symbol	Default value	Description
irradiance wavelength calibration			
irradiance_wavelength_calibration_-degree_polynomial	p	5	The degree of the polynomial for the irradiance wavelength calibration.
irradiance_wavelength_calibration_-max_n_iterations		4	The maximum number of iterations in the irradiance wavelength calibration.
irradiance_wavelength_calibration_-convergence_threshold		1E-3	The convergence threshold for the iterative fit of the irradiance wavelength calibration.
irradiance_wavelength_calibration_-spectral_window		[425, 497] nm	Spectral window for the irradiance wavelength calibration.
DOAS fit			

doas_fit_degree_polynomial	p	5	The degree of the polynomial for the DOAS fit.
doas_fit_max_n_iterations		4	The maximum number of iterations in the DOAS fit.
doas_fit_convergence_threshold		1E-3	The convergence threshold for the iterative DOAS fit.
doas_fit_spectral_window		[425, 497] nm	Spectral window for the DOAS fit.
doas_fit_max_n_spectral_outliers		20	The maximum number of spectral outliers (spikes) removed.
air mass factor			
amf_cloud_correction_-min_cloud_fraction_times_albedo_crb_uvvis		0.05	The cloud correction of air mass factors is applied when the product of cloud_fraction_crb_uvvis and cloud_albedo_crb_uvvis is above threshold.
amf_temperature_correction_-reference_temperature	T_{ref}	221 K	Reference temperature for the parameterized temperature correction of box air mass factors.
amf_temperature_correction_a_coefficient	a	0.00357	Coefficient a for the parameterized temperature correction of box air mass factors.
processing quality flags: errors			
flag_l1b_radiance_missing_threshold		200	Minimum number of valid spectral channels in the fit window for the radiance.
flag_l1b_input_spectrum_missing_threshold		200	Minimum number of valid spectral channels in the fit window for the sun-normalized radiance.
flag_l1b_sza_range_threshold		85°	Maximum solar zenith angle for the air mass factor calculation.
flag_l1b_vza_range_threshold		85°	Maximum viewing zenith angle for the air mass factor calculation.
flag_cloud_missing_threshold		0.5	Minimum QA value for the OCRA cloud

			fraction and ROCINN cloud pressure.
processing quality flags: warnings			
flag_irradiance_warning		200	Minimum number of valid spectral channels in the fit window for the irradiance.
flag_rms_deviation_warning		2E-3	Maximum root-mean-square deviation for the DOAS fit.
flag_wavelength_calibration_warning		[0.05, 0.01]	Maximum values for the wavelength [shift, stretch] from the DOAS fit.
flag_stripe_correction_warning		1E15 molec cm^{-2}	Maximum value for the stripe offset.
flag_high_sza_warning		80°	Maximum solar zenith angle.
flag_high_vza_warning		75°	Maximum viewing zenith angle.
flag_surface_roughness_warning		500 m	Maximum standard deviation of the surface elevation.
flag_uvai_warning		1	Maximum value for the UV Aerosol Index.
flag_model_aerosol_optical_thickness_warning		0.5	Maximum value for the forecast AOT at 550 nm.
flag_gapless_surface_reflectance_warning		0.5	Minimum QA value for the BRF parameters from the GSR product.
flag_model_forecast_warning		0.5	Minimum QA value for the model forecasts from the ECA product.
flag_model_bias_correction_warning		1E15 molec. cm^{-2}	Maximum absolute value for the model bias correction.
flag_stratospheric_correction_warning		[0, 8E15] molec. cm^{-2}	Range for the stratospheric correction.
flag_tropospheric_slant_column_noise_warning		1.0	Maximum value for the relative noise error in the tropospheric slant column.
flag_cloud_fraction_warning		0.5	Maximum value for cloud_fraction_crb_uvvis.

flag_amf_range_warning		0.5	Minimum value for tropospheric AMF

The radiative transfer calculations for the box air mass factor look-up table require numerous configuration settings as well. These setting become algorithm configuration parameters for the processor when box air mass factors are calculated online. One example of such a setting is the cut-off angle for the Ross-Li BRF model above which constant extrapolation is used.

Table 6.8. List of configurable parameters for the BG processor.

Parameter	**Symbol**	**Default value**	**Description**
pixel_selection_max_tropospheric_slant_column		6E15 molec. cm^{-2}	Pixels are selected when the tropospheric slant column (i.e. nitrogendioxide_tropospheric_column times nitrogendioxide_tropospheric_column_air_mass_factor) is below threshold.
pixel_selection_max_tropospheric_column_model		4E15 molec. cm^{-2}	Pixels are selected when the nitrogendioxide_tropospheric_column_model is below threshold.
pixel_selection_max_cloud_pressure_crb_uvvis		1100 hPa	Pixels are selected when the cloud_pressure_crb_uvvis is below threshold.
pixel_selection_min_cloud_fraction_times_albedo_crb_uvvis		0.0	Pixels are selected when the product of cloud_fraction_crb_uvvis and cloud_albedo_crb_uvvis is above threshold.
pixel_selection_max_root_mean_square_fit_residual		3e-3	Pixels are selected when the fitting rms is below threshold.
pixel_selection_max_solar_zenith_angle		90°	Pixels are selected when the solar zenith angle is below threshold.
pixel_selection_max_viewing_zenith_angle		80°	Pixels are selected when the viewing zenith angle is below threshold.
stripe_offset_degree_polynomial	p	2	Degree of the polynomial for determining the stripe offset.
sza_step_size		5°	SZA step in the BG file.
sza_limits		[0°, 85°]	SZA limits in the BG file.
latitude_step_size		5°	Latitude step size in BG file.
latitude_limits		[25°, 75°]	Latitude limits in BG file.
minimum_number_values		10	Minimum number of values found for a row to compute a destriping value. Default destriping value is 0.
offset_weight		0.5	Weighting of new and existing values. 1.0 corresponds to ignoring old values, 0.5 corresponds to equal weighting of old and new values

offset_add_model		True	Decides whether or not the tropospheric column from the model is subtracted from the measured slant columns before comparing with the stratospheric column from the model
destriping_mode		Medi an	Method used for computation of the mean row values

6.2 S4 NO_2 quality assurance

6.2.1 Overview

The quality of the Level-2 data in a granule file is assured as follows:

- A collection of processing flags (errors and warnings) is generated by the NO_2 processor and reported in the output product. This is described in the next section.
- Counters (histograms) for every processing flag over all pixels in the granule are collected as well and stored in the L2 file for quick granule-wise statistical analyses.
- From these processing flags, a so-called Quality Assurance (QA) value is calculated. The QA value is a number between zero (worst) and one (best) indicating the quality of the tropospheric vertical column (the main retrieval parameter). The QA value is calculated as described below (Section 6.2.4).
- In addition, we define a limited set of user flags indicating whether the major retrieval steps performed nominally. While the QA value is a summary indicator describing the quality of the final retrieval parameter (i.e. the tropospheric column), the user flags enable the average user to quickly assess the status of the main intermediate retrieval steps (i.e. the total column) and also the pixel's cloud conditions.

It is important to note that the quality assurance protocol focuses on the main result of the NO_2 product, which is the tropospheric column.

6.2.2 S4 NO_2 processing errors and warnings

In addition to the processing flags read from the Level-1b product or from auxiliary input products, there are also a number of processing flags set specifically by the NO_2 processor. Table 6.9 lists all binary processing errors and warnings used or generated by the S4 NO_2 processor and their corresponding Quality Assurance (QA) impact factors (see also next section).

A processing error or failure refers to the specific situation that a tropospheric vertical column cannot be retrieved. Intermediate results, such as for example fitted slant columns, may however still be obtained and reported in the Level-2 product in that case.

Table 6.9. Binary processing errors and warnings for the S4 NO_2 processor and their QA weight. A processing error or failure refers to the specific situation that a tropospheric vertical column cannot be retrieved. Processing flags are further subdivided into true processing errors ('[…]_error'), pixel selection ('[…]_filter'), missing input data ('[…]_missing') and true processing warnings ('[…]_warning'). Flags are raised whenever the error occurs or the warning is given. Rows starting with a plus-sign (**+**) describe flags copied from the L1b product. Some threshold values may be algorithm specific and should therefore be configurable.

Name	**QA weight**	**Comment / description**
Errors:		

+ l1b_geolocation_flag_error	100	Flag copied from L1b product.
+ l1b_solar_eclipse_flag_error	80	Flag copied from L1b product.
l1b_radiance_missing_flag_error	100	The number of valid spectral channels in the fit window for the radiance is too small to perform a meaningful retrieval. **Threshold**: 50% of channels.
l1b_input_spectrum_missing_error	100	The number of valid spectral channels in the fit window for the sun-normalized radiance is too small to perform a meaningful retrieval (union of bad-pixel masks for the radiance and irradiance). **Threshold**: 50% of channels.
l1b_sza_range_error	100	Solar zenith angle (at the reference ellipsoid) exceeds maximum allowed value. **Threshold**: 85º. *Processor stops after the DOAS fit.*
l1b_vza_range_error	100	Viewing zenith angle (at the reference ellipsoid) exceeds maximum allowed value. **Threshold**: 85º. *Processor stops after the DOAS fit.*
Io_error	100	Error detected during transfer of data between algorithm and framework
numerical_error	100	General fatal numerical error occurred during retrieval.
abort_error	100	Not processed because processor aborted prematurely (time-out or user abort).
cloud_filter	100	The QA value of the crb cloud product is too low. QA value **threshold**: 0.5. *Processor stops after the DOAS fit.*
slant_column_density_error	100	Slant column fit returned error, no values can be computed
airmass_factor_error	100	Airmass factor could not be computed
vertical_column_density_error	100	vertical column density could not be computed
geographic_region_filter	100	Pixel falls outside the specified regions of interest
Warnings:		
+ l1b_geolocation_warning	10	Flag copied from L1b product.
doas_rms_deviation_warning	30	The root-mean-square deviation of the DOAS fit exceeds threshold.

		The logarithm of the sun-normalized radiance is fitted (Equation 5-15). **Threshold**: $2x10^{-3}$
wavelength_calibration_warning	30	Wavelength shift OR stretch from DOAS fit exceed thresholds. Absolute **threshold** shift: 0.05 nm; absolute **threshold** stretch: 0.01
heterogeneous_scene_warning	30	Flag copied from Cloud product
stripe_correction_warning	30	Stripe correction to the fitted slant column larger than expected. **Threshold** on absolute value: 1E15 molec cm-2
+ sun_glint_warning	10	Flag copied from L1b product.
high_sza_warning	30	Solar zenith angle (at the reference ellipsoid) exceeds threshold value. **Threshold**: 80°
high_vza_waning	30	Viewing zenith angle (at the reference ellipsoid) exceeds threshold value. **Threshold**: 75°
surface_roughness_warning	10	Standard deviation of the surface elevation within pixel exceeds threshold value. Standard deviation read from L1b product. **Threshold** 500 m.
snow_ice_warning	30	The pixel is covered by snow or ice. The snow / ice flag from ECA is 1.
uvai_warning	10	Pixel probably contains elevated absorbing aerosols. UV Aerosol Index exceeds threshold value. **Threshold**: 1
model_aerosol_optical_thickness_warning	10	Pixel probably contains aerosols. Aerosol optical thickness at 550 nm from model forecast exceeds threshold value. **Threshold**: 0.5
gapless_surface_reflectance _warning	30	Parameters from the Gapless Surface Reflectance support product have reduced quality (e.g. when static backup is used). QA value **threshold**: 0.5
model_forecast_warning	30	Model forecast from the ECA product has reduced quality (e.g. when nominal base time unavailable and older forecast or static backup is used). Affected variables are NO_2 and T profiles, surface and tropopause layer index. QA value **threshold**: 0.5
model_bias_correction_warning	30	Model bias corrections to the model stratospheric vertical column larger than expected. **Threshold** on absolute value: 1E15 molec cm-2

cloud_warning	30	Cloud product has reduced quality. QA value **threshold**: 0.5
extrapolation_warning	30	Extrapolation in one of the look-up tables.
stratospheric_correction_warning	30	Model stratospheric vertical column outside expected range. Minimum **threshold**: 0 molec cm-2; maximum **threshold**: 8E15 molec cm-2
tropospheric_slant_column_ noise_warning	30	The relative noise error in the tropospheric slant column exceeds threshold. This relative noise error is calculated as the ratio of the slant column error from the DOAS fit (Equation 5-16) and the tropospheric slant column. **Threshold**: 1.0
cloud_fraction_warning	30	Pixel contains clouds, which reduces the sensitivity to tropospheric NO_2. This flag is raised when the OCRA cloud fraction (on UVis pixel grid) exceeds a threshold value. **Threshold**: 0.5
amf_range_warning	50	Tropospheric AMF too small for good retrieval. **Threshold:** 0.5

The background processor reports a warning if insufficient data is available to compute an up-to-date background correction. In that case, existing values will remain unchanged in the background product. As the background processor is initialised with 0-values, this implies that for the first day(s) of processing, effectively no background correction is applied.

Table 6.10. Errors and warnings of the NO_2 background processor

Name	**Comment / description**
Warnings:	
incomplete_input_data_set	Missing or insufficient amount of input data for the calculation of the background correction, old data is used.

6.2.3 S4 NO_2 user flags

The set of flags that we just discussed are technical processing flags used to calculate the QA value. These flags are also of interest to algorithm maintainers and perhaps to some expert users. For the average user, we derive from this set a limited set of user bit flags. As opposed to the processing flags, user flags are raised whenever a major algorithm step performed nominally. The main purpose of these user flags is to help users quickly assess whether the product file contains useful results for their specific application (Table 4.1). User flags are probably best stored separately in the main PRODUCT group as opposed to the processing flags (see Table 6.12). Table 6.11 lists all user flags.

Table 6.11. User binary flags for the S4 NO_2 processor providing general information on the retrieval to increase the usability of the data product. A user flags is raised whenever the major retrieval step performed nominally.

Name	Description	Condition
fitted_slant_column_nominal	Flag raised when a fitted slant column is reported without any major warnings.	*None of these processing flags is set:* geolocation_error solar_eclipse_filter radiance_missing input_spectrum_missing numerical_error abort_error geolocation_warning irradiance_missing rms_deviation_warning wavelength_shift_stretch_warning heterogeneous_scene_warning
destriped_slant_column _nominal	Flag raised when a de-striped slant column is reported without any major warnings.	fitted_slant_column_nominal *is raised AND none of these processing flags is set:* stripe_correction_warning
air_mass_factors_nominal	Flag raised when air mass factors are calculated without any major warnings.	destriped_slant_column _nominal *is raised AND none of these processing flags is set:* sza_range_filter vza_range_filter cloud_missing surface_roughness_warning mixed_surface_type_warning snow_ice_warning uvai_warning gapless_surface_reflectance _warning model_forecast_warning model_bias_correction_warning
stratospheric_slant_column _nominal	Flag raised when a stratospheric slant column is calculated without any major warnings.	air_mass_factor_nominal *is raised AND none of these processing flags is set:* stratospheric_correction_warning
tropospheric_column_nomin al	Flag raised when a tropospheric vertical column is reported without any major warnings. When the pixel is cloudy, the tropospheric column may however be low (no filtering on cloud fraction done here yet).	stratospheric_slant_column _nominal *is raised AND none of these processing flags is set:* tropospheric_sensitivity_warning
pixel_sufficiently_clear	Pixel probably contains no or very little clouds.	*Inverse of processing flag* cloud_fraction_warning

6.2.4 Quality Assurance value

The QA value is calculated from the processing flags as follows:

Starting with a value of 100, for each of the errors and warnings in Table 6.9, the QA weight q_i from the table is subtracted if the error or warning condition is fulfilled, else q_i is set to 0:

$$\mathrm{QA} = 100 - \sum q_i \qquad \text{6-1.}$$

If the QA value is smaller than 0 it is set to 0. The final QA value is then divided by 100 to limit the range to [0..1].

It should be noted that the values given in Table 6.9 are preliminary starting points, and both the thresholds and the weights $\boldsymbol{q_i}$ will be optimised first during commissioning and later during the whole lifetime of the instrument to provide the best information to users.

6.3 Estimated computational effort and timeliness

To estimate the computational effort we make the following assumptions:

- One S4 hourly scan comprises 551 across-track pixels N / S (30-65N) and 580 samples in E / W direction (10 W – 45 E), so around 320 000 observations per hour.
- The horizontal resolution of the TM5 CTM used for stratospheric correction is 1° x 1°.
- The horizontal resolution of the regional CTM used for calculating tropospheric AMFs is 7 x 7 km.
- The processing time will be equivalent to the time estimate for the S5P NO_2 verification algorithm.
- An overall factor of two is applied to account for the increase in disk i/o related to the specific topology of the L2 processors compared to the bread-board algorithm.

One scan of S4 Level-1b data is equivalent to approximately three OMI orbits. Consequently, the spectral fitting should take about 3 times as long as a single OMI orbit. In case the radiance wavelength calibration is linearized, one orbit takes 45 seconds (including disk i/o) if cross-sections are pre-convoluted. This would translate to 135 s or 2.5 min for one S4 scan. When the non-linear radiance wavelength calibration is applied, the computation time increases by a factor of 3-4.

Reading of stratospheric model data, interpolation to measurement locations, application of air mass factors and possibly offset corrections, and writing of output files takes about 60 s for one OMI orbit. As less model data needs to be read for S4 (Europe only and only half a day instead of a full day) it is expected that this step will take about 60 s for S4 as well.

Reading of tropospheric model data, interpolation to measurement locations, computation of air mass factors and averaging kernels, application of the cloud correction and writing of the output file takes 200 s per OMI orbit when using CAMS model data at 1° x 1°. The atmospheric model for tropospheric AMFs will have higher spatial resolution for S4 (factor 100) but is limited to the European region, which will to a large degree cancel the additional file reading time. Taking into account that the number of pixels is a factor of three larger for S4 than for OMI we estimate this step to take less than 600 s.

Calculations of the uncertainties from look-up tables is not yet implemented in the bread-board algorithm. We therefore make the very conservative assumption that it will take as long as the AMF part, adding another 600 s.

The background correction and de-striping module which needs to be called only once per day takes about 60 s for one day of OMI data and is expected to have similar performance for S4.

A rough estimate of the total NO_2 processing time for one hourly scan (excluding the daily background correction) is thus 2 * (135 + 60 + 600 + 600) s or about 47 min on a single core for the linearized wavelength calibration and 2 * (540 + 60 + 600 + 600) s or 60 min for the non-linear wavelength calibration (Intel i5 M580 at 2.67GHz, 4 GB RAM). This is less than the 58 core minutes allocated for a five-minute granule in the L2 Prototype Processor and the 26 core minutes allocated in the Operational Processor ([AD07]).

Reductions in computing time can be achieved by parallelisation of the DOAS fit along rows and distribution of the computation of stratospheric columns, AMFs, and AMF uncertainties over several cores.

Finally, the computation time per pixel is quite constant and we do not expect significant variability between pixels. The only exception here are observations with solar or viewing zenith angles above the cut-off angle for the air mass factors: for these pixels only slant columns are fitted and the air mass factor step is skipped. The cut-off angle is currently set at a relatively high value of 85°.

6.4 S4 NO_2 data product description

The content of the NO_2 data product is similar to that of previous sensors. It contains the main output (tropospheric vertical columns), uncertainties, and also averaging kernels in order to provide the user with the opportunity to compare to other data sets. In addition, a large number of intermediate results are saved for quality control and for convenience of the users.

The general structure of a Sentinel-4 Level-2 file will follow the structure adopted for Sentinel-5 Precursor ([RD17]) and we make an effort to make the S4 NO_2 product format consistent with the format of the S5P NO_2 product ([RD14]). Table 6.12 reports the output parameters generated by the algorithm. Additional parameters such as geolocation, quality control parameters and input data are also included in the L2 product. The product is specified in detail in the corresponding Product User Manual (PUM) ([RD01]).

An entire scan consists of 551 across-track pixels and about 580 integration times (scan lines), and we assume that model data will be available in 60 layers. The entries in Table 6.12 then take up 494 B for one pixel and 158 MB for an entire scan. For an estimate of the complete product file, we refer to the Product User Manual ([RD01]). All variables listed in Table 6.12 are written to the output file in nominal mode; additional parameters may be considered for a debug mode, but that is not further considered here.

Table 6.12. List of output parameters generated by the NO_2 algorithm that are to be included in the L2 product. Also listed are several other parameters that are passed on into the product to increase the usability. The ordered set of all possible dimensions is (time, ground_pixel, scanline, [level | corner | polynomial_exponents]). Here, the time dimension refers to the reference time, which is defined as … The ground_pixel and scanline dimensions refer to the across-track and along-track directions, respectively. Variable names printed in *italics* have no overlapping variable names in S5P, as far as we can see. The column 'M / O' indicates whether parameters are mandatory (i.e. written to the output product in nominal mode) or only optional (i.e. written to the output product in breakpoint or debug mode).

Variable name	Symb.	Source	Unit	Comment	Type	Dims.	M/O
DOAS fit:							
nitrogendioxide_slant_column	N_{s,NO_2}^{fit}	Proc.	mol m^{-2}		f32	g x s	M
nitrogendioxide_slant_column_precision		Proc.	mol m^{-2}		f32	g x s	M

ozone_slant_column	N_{s,O_3}	Proc.	mol m^{-2}		f32	g x s	M
ozone_slant_column_precision		Proc.	mol m^{-2}		f32	g x s	M
water_vapour_slant_column	$N_{s,H_2O_{va}}$	Proc.	mol m^{-2}		f32	g x s	M
water_vapour_slant_column_precision		Proc.	mol m^{-2}		f32	g x s	M
oxygen_dimer_slant_column	N_{s,O_4}	Proc.	mol^2 m^{-5}	Fit coefficient is oxygen concentration squared and integrated along slant path. The actual slant column of O_4 is proportional to the fit coefficient.	f32	g x s	M
oxygen_dimer_slant_column_precision		Proc.	mol m^{-2}		f32	g x s	M
water_liquid_slant_path	$L_{s,H_2O_{liq}}$	Proc.	m		f32	g x s	M
water_liquid_slant_path_precision		Proc.	m		f32	g x s	M
ring_scale_factor	C_{Ring}	Proc.	-		f32	g x s	M
ring_scale_factor_precision		Proc.	-		f32	g x s	M
stray_light_coefficients	C_{stray}	Proc.	mol s^{-1} m^{-2} nm^{-1}	The stray light coefficient is approximately equal to the stray light radiance offset A_{stray} divided by the average sun-normalized radiance (R_{sun}) across the fit window.	f32	g x s	M
stray_light_coefficients_precision		Proc.	mol m^{-2} s^{-1} nm^{-1}		f32	g x s	M
wavelength_shift_radiance	s	Proc.	nm		f32	g x s	M
wavelength_shift_radiance_precision		Proc.	nm		f32	g x s	M
wavelength_stretch_radiance	q	Proc.	-		f32	g x s	M
wavelength_stretch_radiance_precision		Proc.	-		f32	g x s	M
polynomial_coefficients	c_p	Proc.	nm^{-p}	Fourth-order polynomial: p = {0,1,2,3,4}.	f32	g x s x p	M
polynomial_coefficients_precision		Proc.	nm^{-p}		f32	g x s x p	M
root_mean_square_fit_residual	Δ_{RMS}	Proc.	-	The root-mean-square deviation of the fitted spectrum. The logarithm of the	f32	g x s	M

				sun-normalized radiance is fitted. Equation: $\Delta_{RMS} = \left(\frac{1}{m}\sum_{i=1}^{m}\left[y_{meas}(\lambda_i) - y_{fit}(\lambda_i)\right]^2\right)^{1/2}$			
number_of_spectral_points_in_retrieval	m	Proc.	-	Number of spectral points used for solving DOAS equation after bad-pixel masking and spike removal.	ui16	g x s	M
number_of_fit_coefficients_in_retrieval	n	Proc.	-	Number of spectral points and number of fit coefficients are used in the interpretation of the fit residual.	ui16	g x s	M
De-striping:							
nitrogendioxide_slant_column_corrected	N_{s,NO_2}	Proc.	mol m^{-2}		f32	g x s	M
nitrogendioxide_slant_column_corrected_precision		Proc.	mol m^{-2}		f32	g x s	M
Cloud and surface parameters:							
cloud_fraction_crb_intensity_weighted_nitrogendioxide_window	f_{cld}^{rad}	Proc.	-	Cloud radiance fraction used for weighting air mass factors for the clear and cloudy part of the pixel.	f32	g x s	M
cloud_albedo_crb_nitrogendioxide_window	A_c^{NO2}	Proc.	-	Lambertian cloud albedo retrieved at the wavelength of the air mass factor for a given OCRA cloud fraction and ROCINN cloud pressure. Lambertian surface cloud model (CRB).	f32	g x s	M
cloud_fraction_crb_uvvis	f_{cld}^{OCRA}	L2-CLD	-	OCRA cloud fraction for the ground pixel in the UVis bands.	f32	g x s	M
cloud_pressure_crb_uvvis	p_c^{ROC}	L2-CLD	Pa	ROCINN cloud pressure for the ground pixel in the UVis bands. Lambertian surface cloud model (CRB).	f32	g x s	M

cloud_albedo_crb_uvvis	A_c^{ROC}	L2-CLD	-	ROCINN Lambertian cloud albedo for the ground pixel in the UVis bands. Lambertian surface cloud model (CRB).	f32	g x s	M
gapless_bidirectional_reflectance_factor_parameter1	k or a_0	Proc.	- or -	BRF parameters as they are used in the calculation of box air mass factors. Pre-processing of GSR parameter values by the NO_2 processor includes spectral interpolation to the wavelength of the air mass factor, spatial interpolation to the L1b pixel grid in the UVis band, and treatment of mixed land-water pixels.	f32	g x s	M
gapless_bidirectional_reflectance_factor_parameter2	k_1 or σ	Proc.	- or -		f32	g x s	M
gapless_bidirectional_reflectance_factor_parameter3	k_2 or δ_{Fr}	Proc.	- or -		f32	g x s	M
bidirectional_reflectance_factor_model_land_flag		Proc.	-	Bit flag indicating whether BRF land (1) or BRF water (0) model has been used.	ui8	g x s	M
surface_pressure_uvvis	p_s	RI-ECA	Pa	A priori surface pressure from models, possibly elevation corrected.	f32	g x s	M
Stratospheric correction and AMF calculation:							
nitrogendioxide_stratospheric_column	$N_v^{*,strat}$	Proc.	mol m^{-2}	Summation of the bias-corrected model profile over stratospheric layers.	f32	g x s	M
nitrogendioxide_tropospheric_column	N_v^{trop}	Proc.	mol m^{-2}		f32	g x s	M
nitrogendioxide_tropospheric_column_precision	$\sigma_{N_v^{trop}}$	Proc.	mol m^{-2}		f32	g x s	M
nitrogendioxide_tropospheric_column_precision_kernel		Proc.	mol m^{-2}	Uncertainty excluding smoothing error	f32	g x s	M

nitrogendioxide_summed_total_column	N_v^{sum}	Proc.	mol m^{-2}	$N_v^{sum} = N_v^{*,strat} + N_v^{trop}$	f32	g x s	M
nitrogendioxide_summed_total_column_precision		Proc.	mol m^{-2}		f32	g x s	M
nitrogendioxide_doas_total_column	N_v^{DOAS}	Proc.	mol m^{-2}	$N_v^{DOAS} = N_v = {N_s}/{M}$	f32	g x s	M
nitrogendioxide_doas_total_column_precision	$\sigma_{\tilde{N}_v}$	Proc.	mol m^{-2}		f32	g x s	M
nitrogendioxide_doas_total_column_precision_kernel		Proc.	mol m^{-2}	Uncertainty excluding smoothing error	f32	g x s	M
nitrogendioxide_stratospheric_column_air_mass_factor	M^{strat}	Proc.	-		f32	g x s	M
nitrogendioxide_tropospheric_column_air_mass_factor	M^{trop}	Proc.	-	$M^{trop} = f_{cld}^{rad} M_{cld}^{trop} + (1 - f_{cld}^{rad}) M_{clr}^{trop}$	f32	g x s	M
nitrogendioxide_total_column_air_mass_factor	M	Proc.	-		f32	g x s	M
nitrogendioxide_clear_tropospheric_column_air_mass_factor	M_{clr}^{trop}	Proc.	-		f32	g x s	M
nitrogendioxide_cloudy_tropospheric_column_air_mass_factor	M_{cld}^{trop}	Proc.	-		f32	g x s	M
nitrogendioxide_total_column_averaging_kernel	$\mathbf{A}$	Proc.	-	Averaging kernel for the (DOAS) total column ($\mathbf{m}^*/M$).	f32	g x s x l	M
tropopause_layer_index_uvvis	l_{tp}	RI-ECA	-	Index of uppermost layer assigned to troposphere.	f32	g x s	M
Calculation of background corrections:							
nitrogendioxide_stratospheric_column_model	$N_{v,strat}^{model}$	Proc.	mol m^{-2}	Summation of the uncorrected model profile over stratospheric layers.	f32	g x s	M
nitrogendioxide_tropospheric_column_model	$N_{v,trop}^{model}$	Proc.	mol m^{-2}	Summation of the model profile over tropospheric layers.	f32	g x s	M
Other fields:							
user_flag		Proc.		Section 0	ui8	g x s	M
radius_of_curvature	$R_{curvature}$	Proc.	m	Local Gaussian radius of curvature of the WGS84 reference ellipsoid at the nominal pixel centre.	f32	g x s	M
aerosol_index_340_380		L2-UAI	-		f32	g x s	M
boundary_layer_height_uvvis		RI-ECA	m	height a.g.l	f32	g x s	M

Lambertian_equivalent_reflectivity_for_isotropic_illumination	A_{spher}	Proc.	-	The spherical albedo or the bi-hemispherical reflectance for isotropic illumination. Given at the wavelength of the air mass factor. Treatment of mixed land-water pixel…? [Preferably, the spherical albedo reported should be calculated by the NO2 processor itself, so that it can later be compared with the spherical albedo in the GSR product for consistency checking.]	f32	g x s	M
qa_value		Proc	1	continuous quality indicator from 0..1	u8	g x s	M

Several variables are directly copied from L1b to L2 files. These include the nominal geolocation of the pixel centre and the derived pixel corners, the terrain-corrected PSF-weighted mean geolocation, the terrain-corrected PSF-weighted mean elevation and its standard deviation, the pixel's water fraction, the surface classification and the snow / ice descriptive flags.

7 Retrieval characterisation and error analysis

7.1 Vertical sensitivity

7.1.1 Box air mass factors

Figure 7.1 shows box air mass factors for several example scenarios to illustrate the main dependencies. Box air mass factors are taken from the NO_2 box air mass factor look-up table for Sentinel-4. The settings for the radiative transfer calculations with SCIATRAN are described in Section 5.5.3. Box air mass factors are plotted up to an altitude of 40 km.

The geometric approximation to the altitude-resolved air mass factor holds when all atmospheric scattering takes place below the target altitude and only direct paths through the slab or shell of the incoming and outgoing light need to be considered. In a plane-parallel geometry, the geometric air mass factor has the familiar expression $1/\mu$ for both incoming and outgoing light. In a spherical-shell geometry, the length of an incoming direct path through a shell depends on the particular path of the photon to the sensor. When photons are only reflected by the surface, the geometric air mass factor is $\{1-(R/(R+h))^2(1-\mu^2)\}^{-1/2}$ for both incoming and outgoing light. Here, R is the radius of the spherical earth, $R+h$ is the radius of the spherical shell under consideration, and zenith angles μ and μ_0 are defined at radius R (i.e. at the geoid).

In the top left panel of Figure 7.1, box air mass factors are plotted for a solar zenith angle of 46°, several viewing zenith angles, a relative azimuth angle of 0° and a dark surface with an albedo of 4%. Solid lines show box air mass factors from the look-up tables, while the dashed lines show geometric box air mass factors for a spherical-shell atmosphere down to 10 km, where it is assumed that all atmospheric scattering takes place close to the surface. Focussing first on a single plot line, for example the red line corresponding to a viewing zenith angle of 37°, one can see that box air mass factors start deviating from the geometric approximation below an altitude of about 25 km. Apparently, the contribution of scattering at these altitudes is becoming significant. Initially the box air mass factor increases because path lengths in the spherical shell get longer due to multiple scattering. Going further down in the atmosphere, the box air mass factor decreases again. This is due to less light reaching the lower levels in the first place because of the scattering of incoming light in the atmosphere above, and therefore the relative contribution to the intensity at the satellite of photons passing through these lower layers decreases. Furthermore, because the surface is relatively dark, any contribution to the diffuse field in the target layer from the atmospheric column below mainly comes from the atmosphere itself. This is another reason why the box air mass factors decreases with decreasing altitude, because the atmospheric partial column below the target layer simply becomes smaller.

When the viewing zenith angle increases, box air mass factors generally increase, because the outgoing geometric slant path in the shell is longer. This effect is reduced for the lowest layers because the line-of-sight above the target layer becomes longer as well, and hence so will the scattering of light out of the line-of-sight increase. This might explain why box air mass factors close to the surface become actually slightly larger for the smaller viewing zenith angles.

In the top right panel of Figure 7.1, box air mass factors are plotted for several solar zenith angles, a viewing zenith angle of 53°, a relative azimuth angle of 0° and again a dark surface with an albedo of 4%. The same altitude dependence of box air mass factors can be observed. Box air mass factors generally increase with increasing solar zenith angle, because incoming geometric slant paths in the shell are longer. Close to the surface the effect reverses and box air mass factors are slightly smaller for increasing solar zenith angle. Apparently, the increased scattering along the incoming slant path in the overhead atmosphere causing less light to be available in the lowest layers starts dominating.

In the bottom left panel of Figure 7.1, we show box air mass factors for various surface altitudes. Box air mass factors decrease with increasing surface altitudes at all altitude levels where atmospheric scattering makes a significant contribution, because the atmospheric partial column below the target layer becomes smaller.

Finally, the bottom right panel of Figure 7.1 plots box air mass factors for a solar zenith angle of 46°, a viewing zenith angle of 53°, a relative azimuth angle of 0° and several surface albedos. Here, one can see that the surface albedo has a strong effect on the measurement sensitivity near the surface. This also implies that the derivative of the air mass factor with respect to the albedo is large, and that small uncertainties in the albedo value can still result in significant contributions to the total NO_2 tropospheric column uncertainty. The decrease of box air mass factors with decreasing altitude becomes less pronounced for brighter surfaces, as the contribution to the diffuse field from surface reflection becomes significant. In the limit case of an albedo of one, the combination of surface reflection and atmospheric scattering even causes the box air mass factors to peak at the surface. Of course, a similar reasoning holds for the cloud albedo.

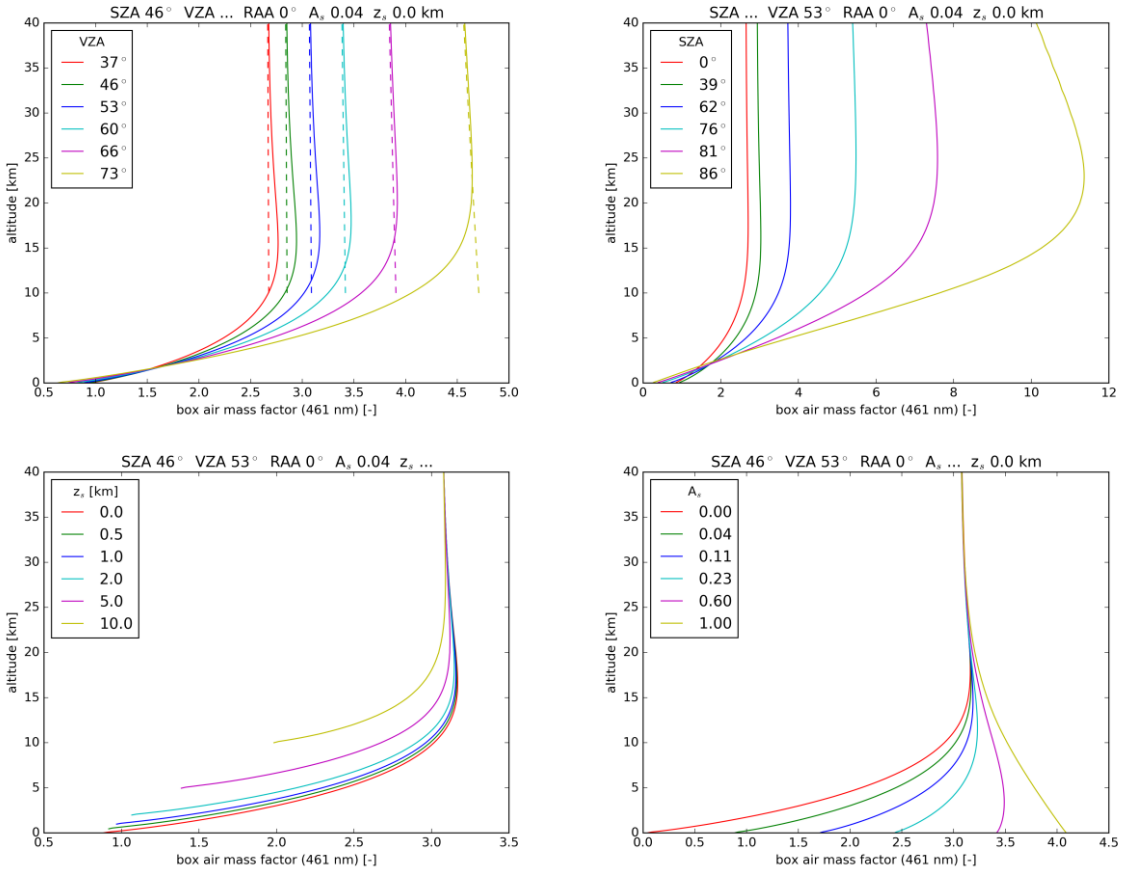

Figure 7.1. NO_2 box air mass factors for several example scenarios: as a function of viewing zenith angle (top left), solar zenith angle (top right), surface albedo (bottom left) and surface altitude (bottom right). Box air mass factors are read from the NO_2 BAMF look-up table calculated with SCIATRAN as described in Section 5.5.3. Calculations are for Rayleigh atmosphere bounded by a Lambertian ground surface. The dashed lines in the top left plot shows the geometric box air mass factors in a spherical atmosphere.

7.1.2 Averaging kernels

Figure 7.2 shows clear-sky tropospheric averaging kernels at summer and winter solstice for three representative locations from the set of reference locations defined in the S4 Geophysical Algorithm Verification subproject ([AD06]). Averaging kernels are calculated with the S4 bread-board algorithm setup. Model data (NO_2, pressure and temperature profiles) were generated for the S4 verification exercise with TM5 and LOTOS-EUROS within the framework of the ISOTROP project ([RD20]). The figure depicts averaging kernels for the tropospheric column in clear-sky conditions. The albedo of the Lambertian ground surface for the specific time and location was taken from the S4 verification Test Data Set (TDS): the spherical albedo derived from the BRF was used as a Lambertian-equivalent reflectivity. The temperature corrections of the box air mass factors are included in the calculations.

The figure illustrates that the retrieval sensitivity to NO_2 in the lowest part of the troposphere is generally low for cloud-free pixels and a dark surface. Roughly speaking, the averaging kernel is about one at the point where the a priori profile peaks. As one can see, all a priori profiles peak in the lowest kilometre, which makes sense because profiles for all three locations are dominated by pollution NO_2. Averaging kernels increase towards the upper part of the troposphere, which means that the retrieved tropospheric column becomes more sensitive to NO_2 at these altitudes. This is caused by the combination of two effects. NO_2 in the free troposphere causes a relatively large increase of the measured slant column because the box air mass factors are larger there (see previous section). However, the retrieval expects any NO_2 to be primarily located near the surface, as this is where the a piori profile shape has its peak. Because the measurement sensitivity is smaller in the lower part of the troposphere, the same slant column will lead to a larger retrieved vertical column.

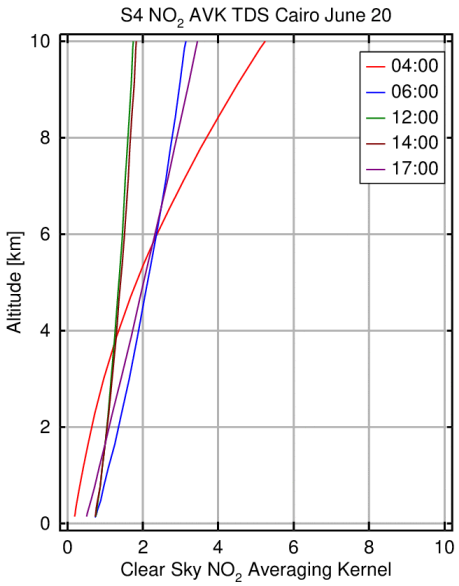
S4 NO2 AVK TDS Cairo June 20
Altitude [km]
Clear Sky NO2 Averaging Kernel
04:00
06:00
12:00
14:00
17:00

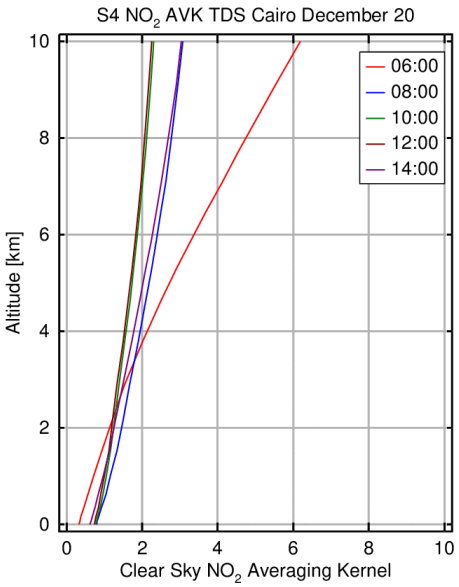
S4 NO2 AVK TDS Cairo December 20
Altitude [km]
Clear Sky NO2 Averaging Kernel
06:00
08:00
10:00
12:00
14:00

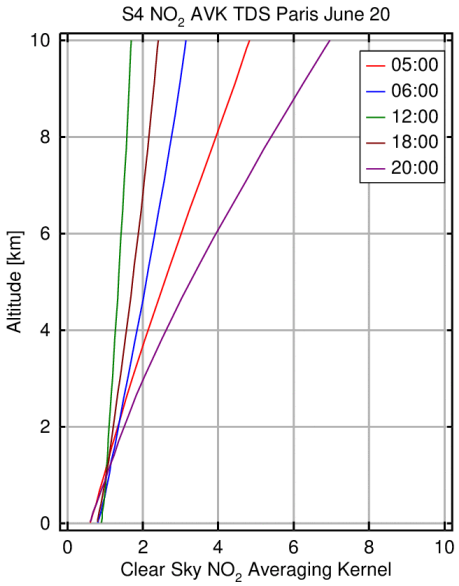
S4 NO2 AVK TDS Paris June 20
Altitude [km]
Clear Sky NO2 Averaging Kernel
05:00
06:00
12:00
18:00
20:00

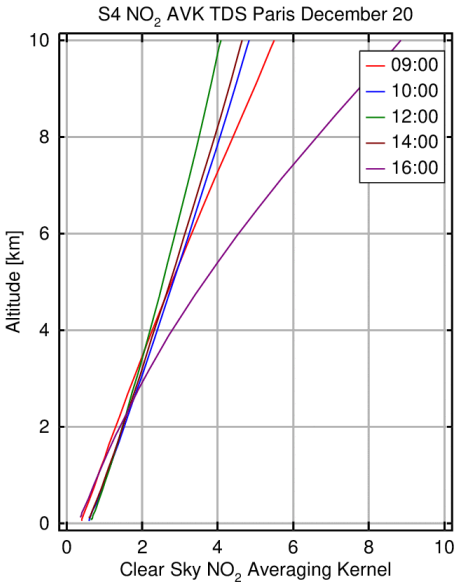
S4 NO2 AVK TDS Paris December 20
Altitude [km]
Clear Sky NO2 Averaging Kernel
09:00
10:00
12:00
14:00
16:00

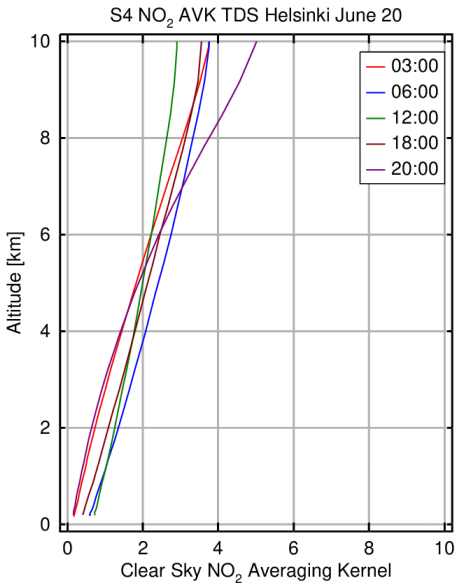
S4 NO2 AVK TDS Helsinki June 20
Altitude [km]
Clear Sky NO2 Averaging Kernel
03:00
06:00
12:00
18:00
20:00

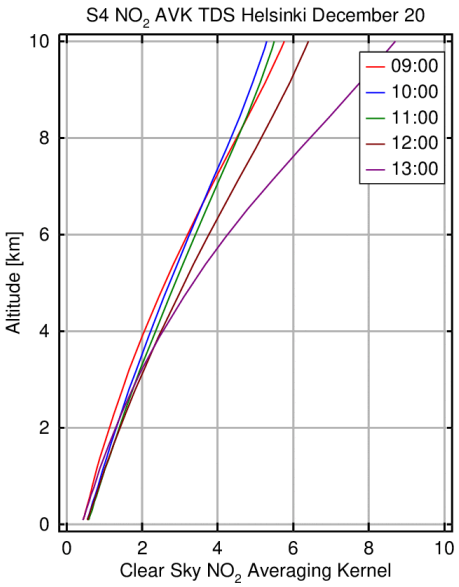
S4 NO2 AVK TDS Helsinki December 20
Altitude [km]
Clear Sky NO2 Averaging Kernel
09:00
10:00
11:00
12:00
13:00

Figure 7.2 (previous page). Averaging kernels for the tropospheric column in clear-sky conditions: panels show averaging kernels for three representative locations (rows) and for several times on June 20 and December 20, 2003 (columns). The times listed in the legend are in UTC. Paris and Helsinki are observed by S4 during the entire day, but Cairo will only be observed in the morning due to the westward shift of the scan area in the afternoon (this is not taken account in these plots). Averaging kernels are calculated with the S4 bread-board algorithm.

7.2 Error budget

7.2.1 Approach

The components of the error budget for the retrieved tropospheric NO_2 columns follow the retrieval steps described in Section 5. In the following sections we provide estimates for each of these components. The general framework to estimate the total error budget for tropospheric vertical columns is described in Section 5.6.2, but this approach and its implementation has to be further developed. At this point, we therefore estimate the total error budget based on (the simplified) Equation 5-79. The total error consists of three aggregated components resulting from the slant column fit, the stratospheric correction and the air mass factor application (error components: $\sigma_{N_S^{fit}}$, $\sigma_{N_S^{strat}}$ and $\sigma_{M^{trop}}$). At a later stage, the more general Equation 5-85 may be used with error components $\sigma_{N_S^{fit}}$, $\sigma_{A^{stripe}}$, $\mathbf{S}_{\mathbf{N_v^*}}$, $\mathbf{S}_{\mathbf{T}}$ and $\mathbf{S}_{\mathbf{m}}$. We will start by giving an estimate of the total error based on experience with previous instruments.

7.2.2 Error budget for previous instruments

Within the S4 NO_2 processor, uncertainties are computed for each satellite pixel as discussed above. How large the uncertainties are for individual measurements cannot be determined at this point as these values depend on instrument performance, the accuracy of the various input parameters and the exact measurement conditions. However, total uncertainty budgets have been derived for satellite NO_2 data products in the literature, and given the similarity between the S4 NO_2 algorithm and the heritage products, these estimates can also give an idea of the uncertainties to be expected for tropospheric NO_2 columns from S4. In the following, a brief overview is given on NO_2 error budgets reported in the literature.

Spectral retrieval

Uncertainties in the spectral retrieval result from photon shot noise, instrumental noise, inaccurate cross-sections, spectral features in the surface reflectance and approximations in the DOAS method. Inaccuracies in the cross-sections create systematic errors of a few percent, which usually can be ignored compared to other uncertainties of the NO_2 retrieval. Spectral surface features including vibrational Raman scattering in surface waters can become significant over specific regions at some times (Vountas et al., 2003; Richter et al., 2011) but are usually small over polluted regions. Details of the fitting window selected and the fitting algorithm used can amount to systematic differences in the NO_2 slant columns of up to $5 \cdot 10^{14}$ molec. cm^{-2} (van Geffen et al., 2015). The main contribution to the random uncertainty in the spectral retrieval is noise and has been estimated to be $5 \cdot 10^{14} – 1 \cdot 10^{15}$ molec. cm^{-2} in GOME measurements (Martin et al., 2002, Boersma et al., 2004), $4 \cdot 10^{14}$ molec. cm^{-2} in GOME-2 measurements (Richter et al., 2011) and $7 \cdot 10^{14}$ molec. cm^{-2} in OMI observations (Boersma et al., 2007). For estimates on the expected noise for S4 NO_2 retrievals, see Section 7.2.3. As noise-related uncertainties in the spectral retrieval are absolute errors, the resulting relative errors depend strongly on the measurement scenario and are of the order of a few percent over polluted regions while exceeding 100% in clean regions.

Stratospheric correction

The stratospheric correction also introduces uncertainties in the tropospheric NO_2 columns. In the approach followed in the S4 NO_2 processor, stratospheric columns are taken from a model using data assimilation to constrain the stratospheric NO_2 fields, with additional daily bias correction in the processor. The uncertainty of this corrected product can only be assessed by validation with independent observations and the discussion is further complicated by the fact that some cancellation of errors can occur when assimilating biased satellite data and then correcting the same biased values for the stratospheric contribution as was the case for OMI data (see e.g. van Geffen et al., 2015). The uncertainty for the assimilated vertical stratospheric NO_2 column of the TEMIS GOME product is given as $2 \cdot 10^{14}$ molec. cm^{-2} in Boersma et al. (2004). Dirksen et al. (2011) reported annual differences of $3 \cdot 10^{14}$ molec. cm^{-2} between OMI stratospheric vertical columns and ground-based measurements. These estimates are confirmed by the study of Beirle et al. (2016), who compared several different stratospheric correction schemes and found deviations between them with a similar order of magnitude on monthly averages. For individual pixels, uncertainties can be much larger. For polluted situations, the contribution of the stratospheric uncertainty to the total error of the tropospheric NO_2 column is small. However, in clean regions, the contribution of the stratospheric uncertainty is comparable to that of the noise and thus not negligible. In contrast to the noise contribution, the stratospheric uncertainty is often not random but can lead to persistent biases depending on region and season.

Air mass factors

The largest source of uncertainty in tropospheric NO_2 retrievals are the tropospheric air mass factors. Three different error sources contribute to the uncertainties: (i) uncertainties in the calculation of AMFs using radiative transfer models and look-up-tables, (ii) uncertainties in the input parameters and (iii) uncertainties in the temperature correction also performed in the AMF calculation. While RTM and LUT uncertainties are estimated to be relatively small and of the order of 2 – 3% (Lorente et al., 2016), the overall uncertainties from AMF calculations however are large and have been estimated to be 17% for clean regions and 20 – 29% for polluted regions (Boersma et al., 2004), 40 – 60% for polluted regions (Richter et al., 2005) and 20 – 50% depending on region (Lamsal et al., 2014). In Lorente et al. (2016), AMF calculations from different groups using various levels of harmonisation are compared and a structural uncertainty of 30 – 40% is estimated for the AMFs. For the S4 NO_2 product, some of the parameters will have less importance than in the study of Lorente et al. (2016), as aerosol load over Europe is usually lower than over Asia and surface reflectance is provided by concurrent retrievals and not a static climatology, but the larger observation angles reduce sensitivity to the lower atmosphere and thereby increases uncertainties.

Overall error budget

In most studies in the literature, the overall uncertainty has been given by combining the random and stratospheric uncertainties to an absolute error and the AMF uncertainties to a relative error. Typical values are $0.5 - 1.5 \cdot 10^{15}$ molec. cm^{-2} and 10 – 40% (Boersma et al, 2007) or $0.5 - 1 \cdot 10^{15}$ molec. cm^{-2} and 40 – 60% (Richter et al., 2005). These rule of thumb estimates are expected to also hold for S4 retrievals.

Total column uncertainty

Uncertainties for total NO_2 columns are not discussed in the literature as these are rarely used in atmospheric applications. As total columns are computed from the sum of the retrieved tropospheric and the model provided stratospheric column, the uncertainty of the total column is a combination of both. Over polluted regions, the error budget is dominated by the tropospheric part which has much larger uncertainties and often also larger absolute values and has been discussed above. Over clean regions however, the stratospheric contribution dominates and the uncertainty of the total column will be close to the uncertainty of the stratospheric column which depends on season, latitude and solar zenith angle and usually is largest at high latitudes in spring.

7.2.3 Errors in fitted slant columns

Slant column errors in the operational retrieval are calculated from the fit residuals and subsequent error propagation based on the coefficients of the DOAS equation. The assumption is made that the fit residual is dominated by uncorrelated random errors with a constant magnitude across the fit window (white noise). This is described towards the end of Section 5.2.1. For the purposes of the sensitivity studies and the calculation of the expected error budget, we need to estimate the noise error in the slant column based on the latest model for S4's signal-to-noise ratio. We take the following approach to constructing a look-up table of slant column errors.

Instead of performing calculations of radiance spectra across the entire fit window for many scenarios, which would take too much time, we use SCIATRAN to simulate radiances at S4 instrument resolution for only three wavelengths. These wavelengths are at the start, in the middle and at the end of the fit window (425, 461 and 497 nm, respectively). The S4 radiance and irradiance noise models are then used to determine the 1-σ noise error in the logarithm of the convolved sun-normalized radiance ($\ln(I_n)$ or y in Equation 5-15). These noise errors are divided by the root-mean-square of the differential NO_2 absorption cross-section used in the DOAS fit and the maximum of the three values divided by the square root of the number of spectral channels (spectral sampling interval is 1/6 nm which implies 432 spectral points) is reported as the expected slant column noise error. Division of the noise error by the root-mean-square of the differential cross-section follows from linear error propagation assuming that the absorption cross-sections are completely orthogonal. The settings for the radiative transfer calculations and the dimensions and nodes of the resulting look-up table are similar to the settings and scenarios for the box air mass factor look-up table (Section 5.5.3).

This approach was verified by doing a full simulation of slant column noise errors for a small subset of scenarios (n = 10) spanning the range of intensities typically encountered (e.g. surface albedo varied between 0.05 and 0.8). High-resolution spectra were calculated for the complete fit window, they were subsequently convolved with the S4 ISRF and Gaussian noise according to the S4 noise models was added to the radiance and irradiance spectra repeatedly (500 times). These spectra were used in a slant column fit using S4 settings as much as possible and the standard deviations of the slant columns fitted from the noisy spectra were calculated. These standard deviations are taken as the true slant column error estimates. The true slant column noise errors and the noise errors from the look-up table following the approach described earlier correlate very well (r = 0.99). In the range of slant column errors typically encountered (1 - 4 · 10^{14} molec. cm^{-2}), the difference between the regression and the $y=x$ line is -16% at 1 · 10^{14} molec. cm^{-2} and +5% at 4 · 10^{14} molec. cm^{-2}. These differences are significant and most likely primarily due to absorption cross-sections being not completely orthogonal, as we assumed in calculation of the look-up table noise errors. Nevertheless, for our purposes the agreement is good enough.

As an illustration, Figure 7.3 shows expected NO_2 slant column noise errors for four times of the day at equinox. These maps are for cloud-free pixels, but noise errors for partly cloudy pixels can be easily calculated from the look-up table. The Lambertian-equivalent reflectivity for the isotropically reflecting ground surface is derived from the minimum LER in the SCIAMACHY climatology (Tilstra et al., submitted), surface altitudes are calculated from the DEM in the SDP toolkit and the atmosphere is US Standard. Also drawn is the contour corresponding to a viewing zenith angle of 85° (purple line). Currently, tropospheric slant columns are not retrieved for viewing (and solar) zenith angles larger than this value. Finally, the area covered by a single scan in the morning is approximately the region between the solid grey contours, while the area covered by a single scan in the afternoon is approximately the region between the dashed grey contours.

According to the S4 noise model provided by ESA, instrument noise is by far dominated by shot noise. Since the relative irradiance noise error is much smaller than the relative radiance noise error, the relative noise error in the sun-normalized radiance is about inversely proportional to the square root of the measured radiance (in photons) and so must then be the absolute noise error in slant columns. Patterns in slant column noise errors as illustrated in Figure 7.3 thus follow patterns in radiances. The overall order of magnitude of expected slant column errors for S4 is between 10^{14} and 10^{15} molec. cm^{-2}. Generally, intensities for a Rayleigh atmosphere are larger (i.e. slant column errors are smaller) when the viewing zenith angle increases, the solar zenith angle decreases and the ground surface is brighter or less elevated (not further explained). All these major effects can be seen in Figure 7.3. Modulating effects are related to the anisotropy of the phase function, the spherical shell geometry and of course the multiple scattering contribution (not further explained). As a final remark, a small error in the slant column does not necessarily imply a small error in the tropospheric vertical column as the smaller slant column error may be offset by a decrease in the tropospheric air mass factor (e.g. reduced sensitivity in the troposphere for large viewing zenith angles), see Equation 5-79 and below.

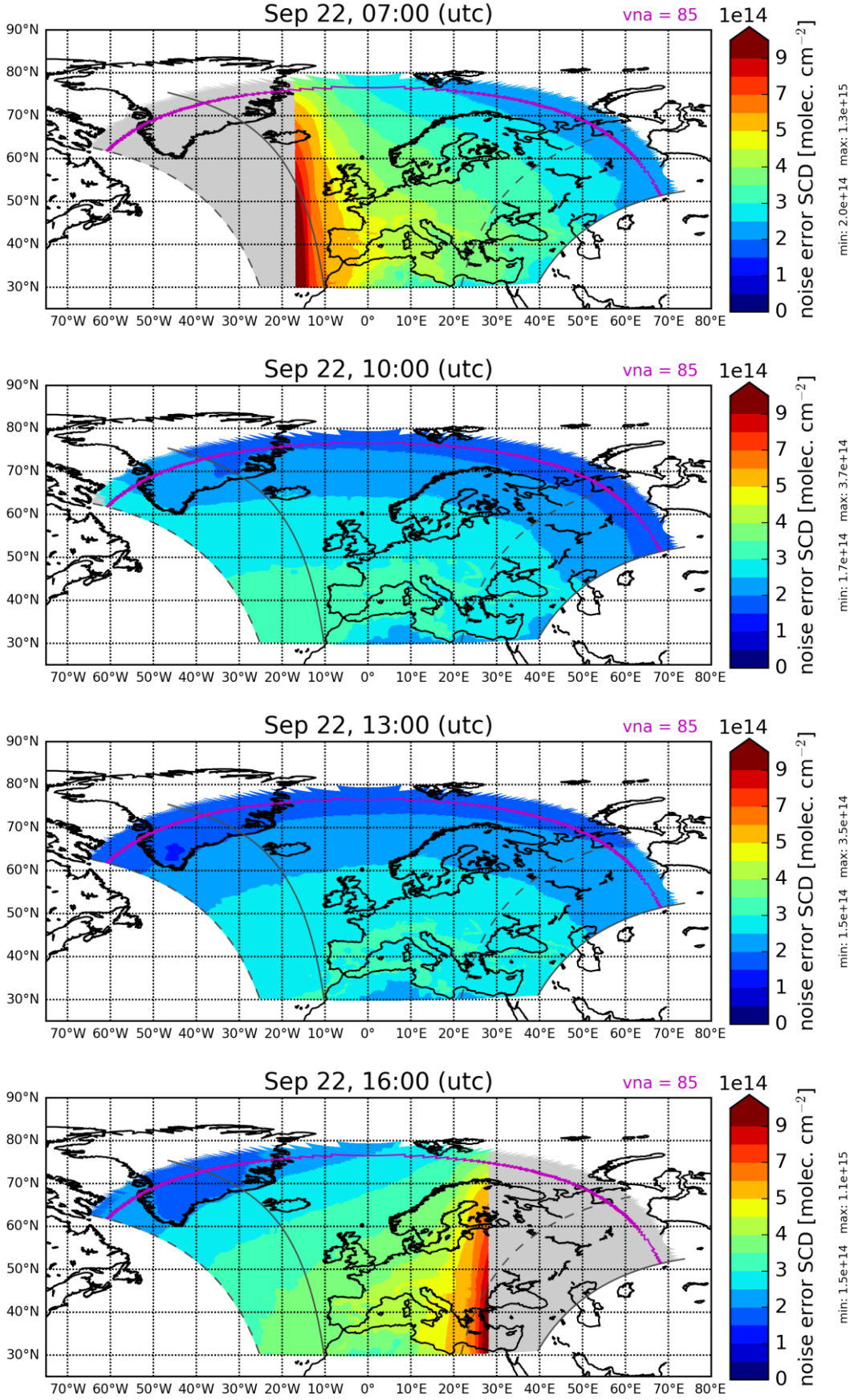
Sep 22, 07:00 (utc)
vna = 85
1e14
noise error SCD [molec. cm^{-2}]
min: 2.0e+14 max: 1.3e+15
Sep 22, 10:00 (utc)
vna = 85
1e14
noise error SCD [molec. cm^{-2}]
min: 1.7e+14 max: 3.7e+14
Sep 22, 13:00 (utc)
vna = 85
1e14
noise error SCD [molec. cm^{-2}]
min: 1.5e+14 max: 3.5e+14
Sep 22, 16:00 (utc)
vna = 85
1e14
noise error SCD [molec. cm^{-2}]
min: 1.5e+14 max: 1.1e+15
90°N 80°N 70°N 60°N 50°N 40°N 30°N
70°W 60°W 50°W 40°W 30°W 20°W 10°W 0° 10°E 20°E 30°E 40°E 50°E 60°E 70°E 80°E

Figure 7.3 (previous page). Expected noise errors in NO_2 slant column densities under cloud-free conditions for four times of the day (rows) at equinox. Calculations are based on anticipated S4 instrument specifications. Pixels with viewing zenith angles larger than 90° are masked. The purple contour corresponds to a viewing zenith / nadir angle of 85°. The two solid grey contours indicate the region that is covered by a single scan in the morning; the two dashed grey contours indicate the westward shifted region that is covered by a single scan in the afternoon.

7.2.4 Errors in stratospheric slant columns

Stratospheric columns are calculated from NO_2 profile forecasts. These forecasts are made by a model that assimilates NO_2 columns from polar orbiting satellites. Within the NO_2 processor, profile forecasts are further corrected for any spatial and temporal model biases. Model forecasts for the operational processor are in principle delivered by CAMS: the specifications of the model output for Sentinel-4 is currently under discussion. As explained already in Section 5.6.2, the main contribution to the error in stratospheric slant column estimates comes from these bias-corrected profile forecasts (stratospheric vertical column as well as the stratospheric profile shape). A secondary contribution might be from the temperature profile.

Once more information is available on the model output that we can expect from CAMS, error estimates for the stratospheric correction will be added in Phase 2.

7.2.5 Errors in tropospheric column air mass factors

Several error sources contribute to the error in the tropospheric column air mass factor, which have been identified already in Section 5.6.2. The most important ones are related to the a priori tropospheric profile shape, directional surface reflectance, the cloud correction, the treatment of aerosols, and perhaps the temperature correction. A priori profiles for S4 will be provided by regional air quality models from CAMS, which is a new development. The S4 cloud retrieval concept has not yet been used for scattering correction in NO_2 retrievals and also the retrieval of directional surface reflection has no heritage.

Sensitivity studies will be performed in Phase 2 based on the information from the Cloud and SUR developers provided in the v1.5 ATBDs.

7.2.6 Expected total error in tropospheric NO_2 columns

Figure 7.4 shows absolute errors in tropospheric vertical columns when the only error contribution is from S4 measurement noise. The error in the tropospheric vertical column in that case is the slant column noise error from the DOAS fit (Figure 7.3) divided by the tropospheric air mass factor. As already explained above, the noise error is calculated following the S4 measurement noise model. Tropospheric column air mass factors are calculated from the S4 box air mass factor look-up table assuming Lambertian surface reflection. A priori profiles are calculated with TM5 and LOTOS-EUROS within the ISOTROP project and also used for the S4 Verification exercise.

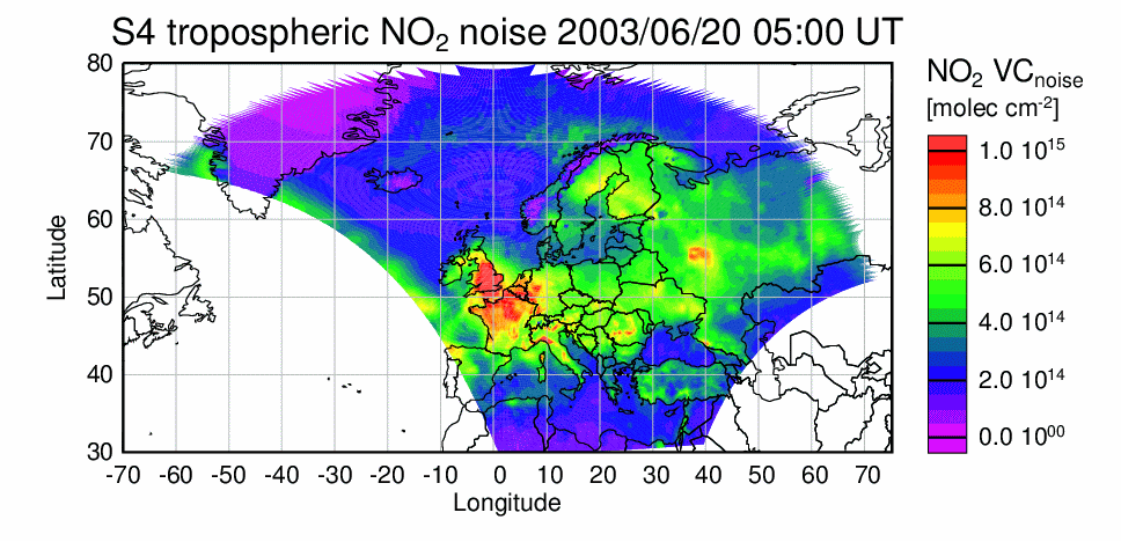
S4 tropospheric NO2 noise 2003/06/20 05:00 UT
Latitude
Longitude
NO2 VCnoise
[molec cm-2]
1.0 10^15
8.0 10^14
6.0 10^14
4.0 10^14
2.0 10^14
0.0 10^00

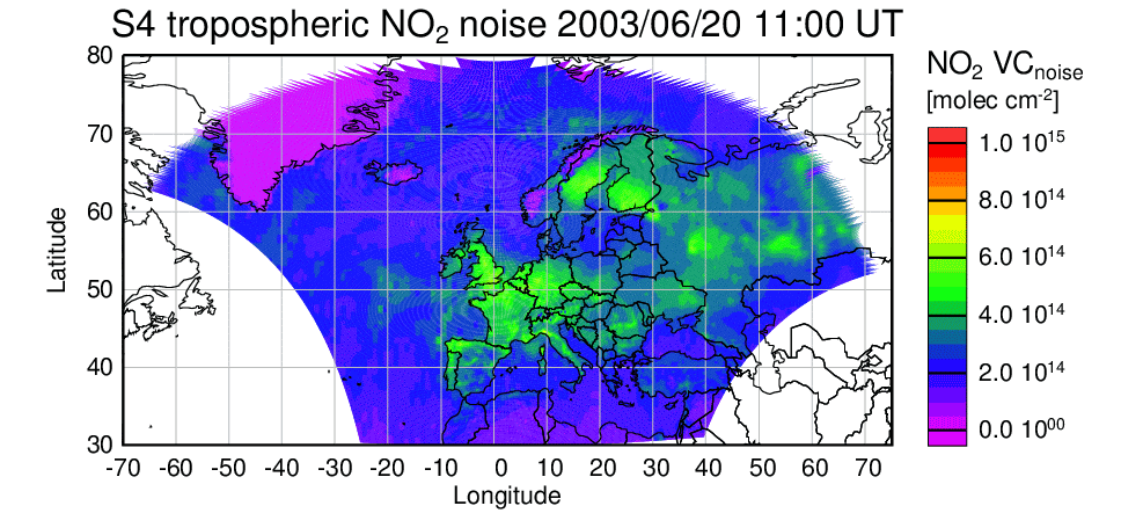
S4 tropospheric NO2 noise 2003/06/20 11:00 UT
Latitude
Longitude
NO2 VCnoise
[molec cm-2]
1.0 10^15
8.0 10^14
6.0 10^14
4.0 10^14
2.0 10^14
0.0 10^00

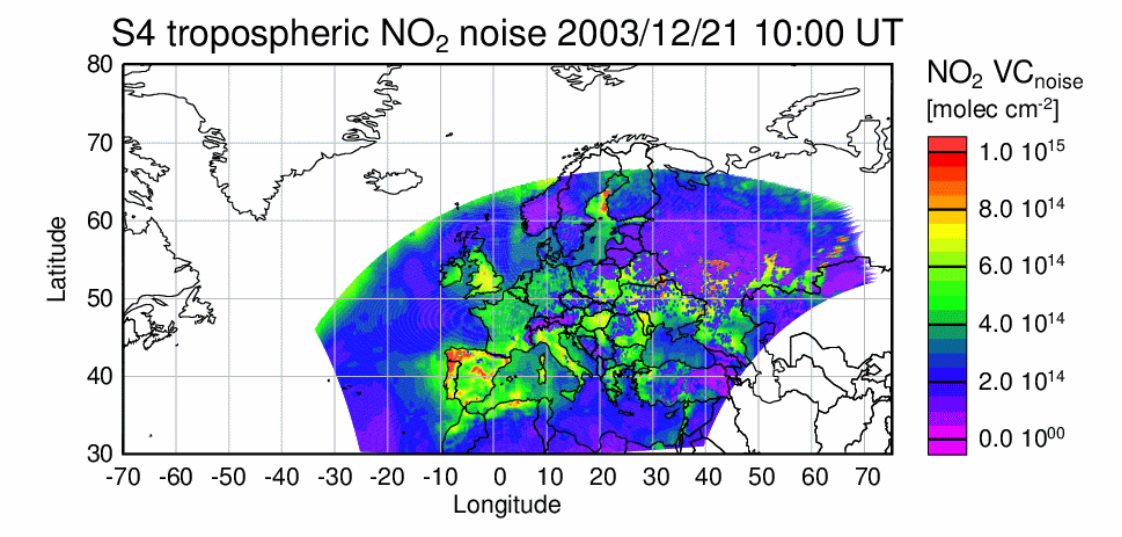
S4 tropospheric NO2 noise 2003/12/21 10:00 UT
Latitude
Longitude
NO2 VCnoise
[molec cm-2]
1.0 10^15
8.0 10^14
6.0 10^14
4.0 10^14
2.0 10^14
0.0 10^00

Figure 7.4. Absolute noise errors in tropospheric vertical columns for clear-sky conditions: noise errors are shown for 5 h UTC, June 20 (top panel), 11 h UTC, June 20 (middle panel) and 10 h UTC, December 21, 2003 (bottom panel). Errors are calculated with the S4 bread-board algorithm for anticipated S4 settings. Maps show the entire geographic coverage area of S4, but note that part of this area in the west will not be observed in the morning while part of that area on the east will not be observed in the afternoon.

We focus first on the middle panel of Figure 7.4, where we show the noise error for 11 h UTC on June 20, 2003. Because of Daylight Saving Time, this corresponds to 13 h Central European Time (CET). Overall, errors are larger over continental Europe (green colours) compared to for example the open ocean (blue colours) because of the increased boundary layer pollution: the a priori profiles are peaked near the surface where the box air mass factors are small. The tropospheric column air mass factor will be small accordingly and this results in a large error. In the top panel we show the noise error for 5 h UTC or 7 h CET on June 20, 2003. The sharp increase in the error observed here is probably due to the combination of the morning rush hour and the shallower boundary layer at the start of the day. This causes the profile to be more sharply peaked close to the surface. Of course, also patterns in tropospheric column noise errors related to the dependencies of the slant column noise error discussed above can be appreciated, particularly at those places where no tropospheric pollution is expected and the profile is more smooth. As an example, smaller errors can be observed over bright and unpolluted Greenland and increasing errors can be seen when the solar zenith angle is large (at high latitudes or at the start and end of the day).

Finally, we remark that the total error in the tropospheric column will be dominated by measurement noise only under clean conditions. In pollution conditions, however, errors in air mass factors related particularly to the a priori profile will be much larger.

7.3 Other sensitivity studies

7.3.1 Temperature dependence of the ISRF

ISRF data for three spectrometer temperatures (19.5°C, 20.0°C and 20.5°C) and several wavelengths and field angles were provided by ESA. The effect of the ISRF's temperature dependence on the retrieval of NO_2 was evaluated for a small set of radiance spectra calculated for the following scenarios:

- Nadir view, solar zenith angles between 0° and 85°;
- O_4, NO_2, O_3 included with T-dependence;
- Surface albedo 0.05;
- US standard atmosphere with NO_2 pollution layer added in lowest kilometre;
- No aerosols, no polarisation, no Raman scattering, no noise added;
- Chance and Kurucz (2010) solar Fraunhofer atlas as irradiance.

The resulting monochromatic radiances were convolved as discussed below and sampled at 0.15 nm (approximately S4 sampling). A standard DOAS fit was then performed using the settings of the S4 NO_2 bread-board algorithm. Results were analysed for changes in the NO_2 slant column, which would transfer directly to changes in the NO_2 vertical column, and for changes in the RMS deviation of the fit (Equation 5-15).

In all cases, the slit function at 19.5°C was used for the convolution of the absorption cross-sections. Two scenarios for the convolution of spectra were considered. In the first, the radiance was convolved with a perturbed slit function while the irradiance was convolved with the slit function at 19.5°C. This scenario probably realistically represents temperature effects, because any temperature variability of the optical bench will likely have a strong diurnal component. In the second, both radiance and irradiance were convolved with perturbed slit functions, which were however the same for the two measurements. This scenario is probably more representative of other calibration errors in the ISRF. The test slit functions are the slit functions at 20.0°C and 20.5°C, and the slit function at 19.5°C but with the wavelength axis multiplied by a factor 1.01. Stretching the wavelength axis like this produces an increase of the FWHM of 1%, which is the mission requirement on the maximum uncertainty in the ISRF's width. The results are summarised in Figure 7.5.

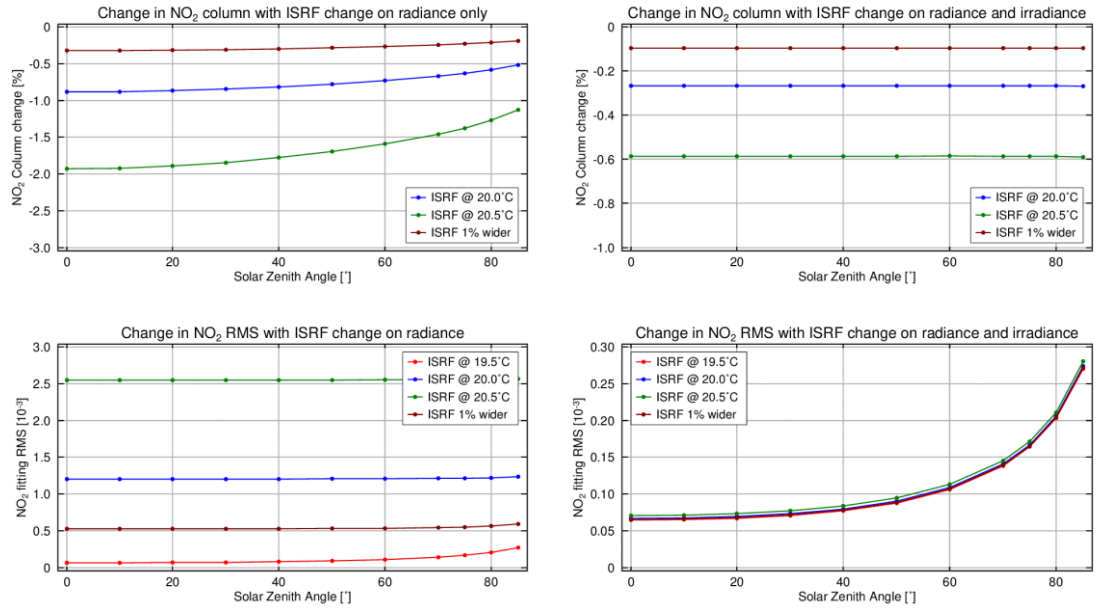

Figure 7.5. Changes in NO_2 slant column (top) and NO_2 fitting RMS (bottom) when the slit function for the radiance (left) or for the radiance and irradiance (right) are as indicated in the labels. The absorption cross-sections are always convolved with the ISRF at 19.5°C and so is in the left column also the irradiance. Note the different scales of the figures.

As can be seen in the top left panel of Figure 7.5, a change of the ISRF for the radiance measurement corresponding to a 1°C temperature difference can lead to NO_2 slant column changes of up to 2% for this set of scenarios. This error is smaller than the expected noise error (Section 7.2.3) but not completely negligible. The relative slant column error decreases with increasing SZA. For comparison, the slant column difference when the ISRF is stretched by 1% is also shown. The error is smaller in this case and typically below 0.5%. These results can be understood as follows. In the DOAS equation, an error in the radiance ISRF results in an additive error to the fitted intensity logarithm of $\ln\left(\tilde{I}(\lambda_i)/\bar{I}(\lambda_i)\right)$, where the accents indicate convolution with the assumed and true ISRFs. These residuals, whose spectral shape will be quasi-random but whose magnitude is independent of solar zenith angle, will bias the NO_2 retrieval. As the slant column increases with solar zenith angle, the relative slant column error will decrease.

If the perturbed ISRF is applied to both radiance and irradiance, the change is NO_2 slant column is smaller than 1% for all cases and does not depend on SZA (top right panel of Figure 7.5). These results can be understood as follows. In the DOAS equation, an error in the ISRF used for the convolution of the absorption cross-section results in a systematic scaling of the slant column by a factor $\tilde{\sigma}(\lambda_i)/\bar{\sigma}(\lambda_i)$ and the relative slant column error therefore does not depend on SZA. Comparison of the fitting residuals (also shown in Figure 7.5) confirms these interpretation: Large increases in RMS (more than a factor of 30) are observed if the ISRF in radiance and irradiance differ while the RMS is only slightly increased if the same ISRF is used on irradiance and radiance but not on the NO_2 absorption cross-section. Note the small non-zero residuals that increase with SZA in the bottom left panel when all ISRFs are unperturbed (light red line). These residuals are due to the assumption of wavelength independent slant columns (air mass factors).

Finally, on real data, noise and additional effects for example from Raman scattering will change the results. For the RMS, the absolute errors will become larger as the Ring effect is sensitive to slit function changes: the relative change in RMS will however be smaller. Changes in NO_2 slant column will probably be of a similar order in real data as in synthetic data.

7.3.2 Cloud Threshold values

As discussed in section 5.5.10, application of the cloud correction in the AMF calculation is limited by two threshold values: A lower threshold below which no cloud correction is applied and the measurement is treated as a clear-sky observation, and an upper threshold beyond which tropospheric columns are flagged as being unreliable as they have too little information on NO_2 below cloud top. The thresholds are configurable items (see Table 6.7) and the default values are based on good practice from earlier missions.

A sensitivity study on S5P data was performed in order to evaluate if a more solid justification for the choice of thresholds can be derived from a statistical analysis of real measurements. The test data set was produced using the following settings:

- Full year 2020 of S5P tropospheric NO_2 above Europe derived by S4-ABB algorithm
- CAMS global model a priori
- CAMS regional ensemble model a priori where available
- OCRA / ROCINN cloud product version UPAS 2.1.4
- STREAM stratosphere (CAMS stratosphere not yet available)

It should be noted that in the ROCINN cloud retrieval, scenes having less than 5% cloud cover are not processed and therefore have been treated as cloud free.

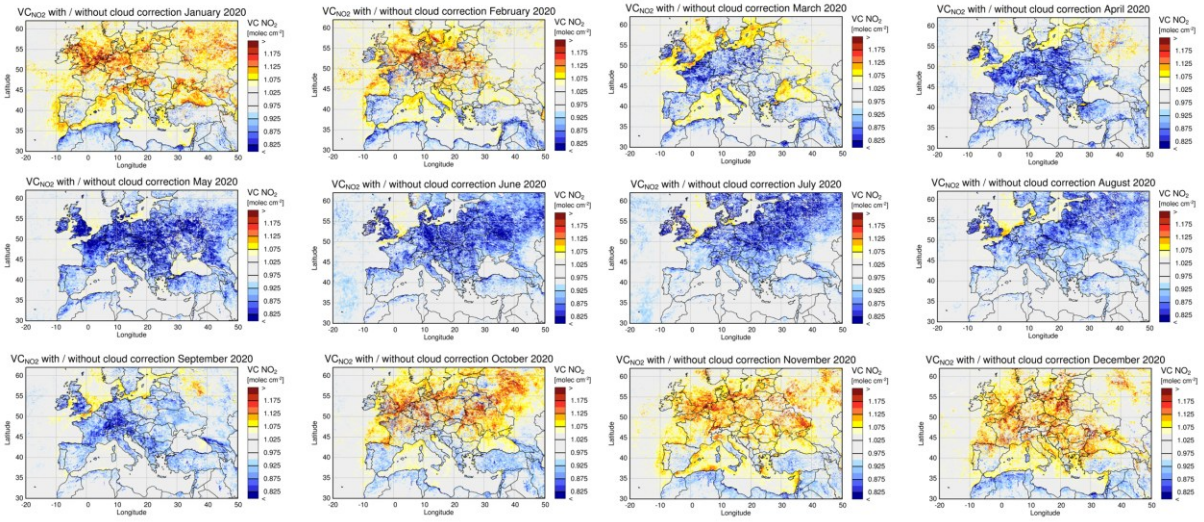

Figure 7.6: Ratio between tropospheric vertical columns with and without cloud correction. Only scenes with less than 20% cloud fraction are included. Data are from the S5P test data set described in the text.

For this test data set, monthly averages were computed with and without cloud correction in order to evaluate the effect of cloud correction on real data. It should be noted, that only scenes having cloud fractions less than 20% were included. This is a typical threshold used for other missions. Results are shown in Figure 7.6, where the ratio of the analysis with and without cloud correction is shown. While in fall and winter cloud correction increases the retrieved columns, the opposite is true in spring and summer. There also is a clear sea-land contrast visible in the ratios. The magnitude of the cloud correction is mostly smaller than +/-20% on a monthly average.

Ratios larger than one would be expected for high clouds (NO_2 is hidden below clouds) while ratios smaller than one should be found for low clouds if there is NO_2 above the cloud. That this is indeed what happens in the processor is illustrated in Figure 7.7 for the case of data over Madrid in January 2020. For large cloud pressures (low clouds), NO_2 columns without cloud correction are overestimated while for low pressures (high clouds), the opposite is true.

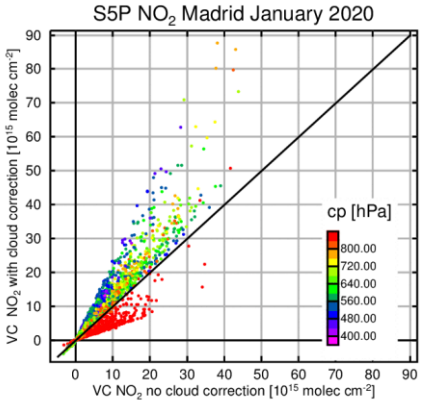

Figure 7.7: Scatter plot of tropospheric NO_2 columns without (x-axis) and with (y-axis) cloud correction. Colours indicate the corresponding cloud heights. Only measurements having cloud fractions < 20% are included.

The results shown in Figure 7.6 are surprising in several aspects: 1) There is no indication that pollution hot-spots behave differently than background regions. 2) It is not clear, why there should be relatively more NO_2 above clouds in summer than in winter. 3) When repeating the same analysis with an alternative cloud retrieval (FRESCO, not shown), different patterns are found at least for some months. This indicates that at small cloud fractions, cloud heights are not well constrained and results depend on the assumptions made in the retrievals.

In order to study the effect of cloud correction over a broader range of cloud fractions, data over several locations was collected for individual months and binned as a function of cloud fraction. In an ideal case where NO_2 levels do not depend on cloud fraction, a constant NO_2 value should be found, independent of cloud fraction. Again, data with and without cloud correction were compared. Results are shown in Figure 7.8.

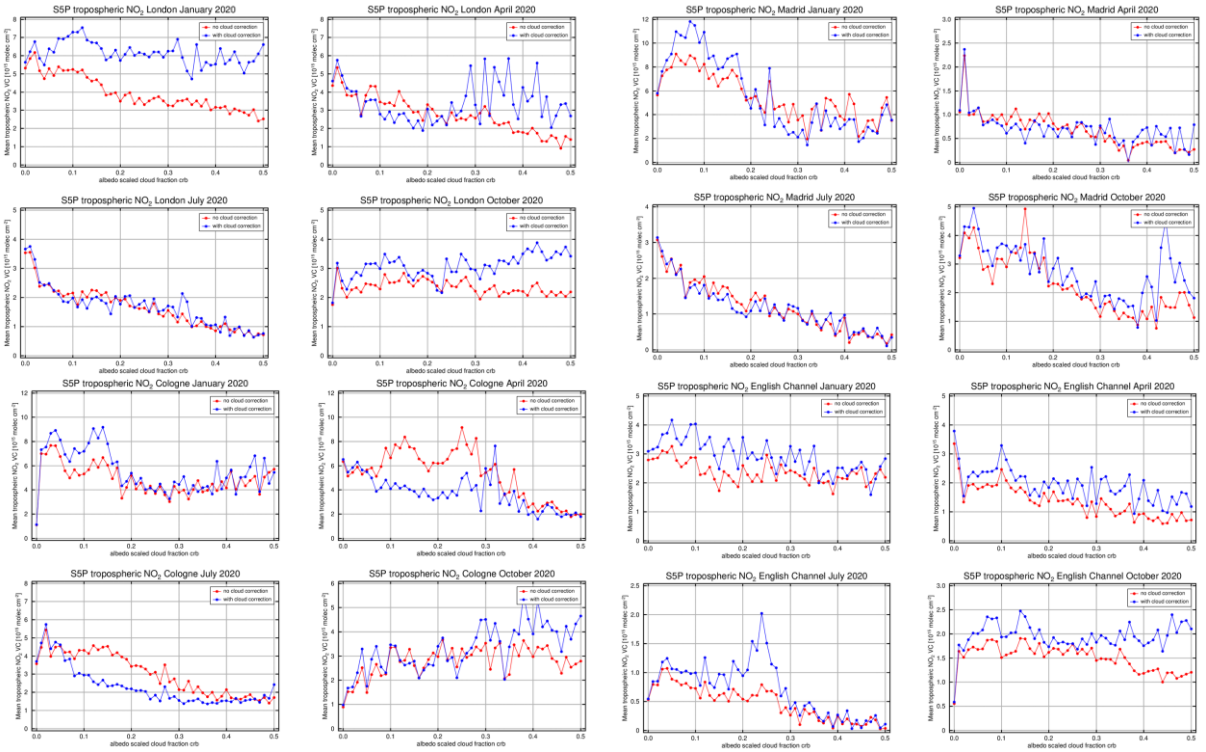

Figure 7.8: Dependence of tropospheric NO_2 column on cloud fraction for four locations: London and Madrid (top) and Cologne and the English Channel (bottom). Data for January, April, July and October 2020 are shown. The red line is for the analysis without cloud correction; the blue line shows results including cloud correction.

As can be seen from Figure 7.8, there is no clear systematic in the behaviour. Sometimes, the cloud correction leads to more consistent results (London, January 2020), often, rather small changes are introduced by the cloud correction and sometimes, the correction leads to stronger dependence on cloud fraction (Cologne, July 2020). There could be several reasons for this result: Either the assumption that NO_2 columns are independent of cloud cover is not correct as meteorology has an impact on both, cloud cover and pollution levels. Or the results are dominated by random effects of sampling as one month of data may not be enough for the study. Or cloud correction does not perform as well as one would hope, either because of uncertainties in the cloud parameters or because of a mismatch between the real vertical distribution of NO_2 and the CAMS model NO_2 profile.

In conclusion, no way was found to provide a quantitative approach for the selection of cloud correction thresholds. Therefore, it was decided to use the empirical values used for earlier missions and to revisit this question once real S4 data and validation results become available.

8 Validation

8.1 Validation requirements

Validation of satellite NO_2 observations has been performed routinely since the launch of the GOME instrument in 1995, first on stratospheric columns only and later also on tropospheric columns. Validation requirements and approaches have been discussed in detail for all previous sensors and here we start from the most recent work done for the S5 instrument ([RD21]).

The most important validation need for S4 NO_2 is for tropospheric NO_2 under polluted and clean conditions. Under polluted NO_2 conditions, column and profile information in the lower troposphere is essential for column density validation. The NO_2 data from GOME, SCIAMACHY, OMI, GOME-2, and TROPOMI has been validated in several studies over the past years, based on satellite inter-comparisons as well as comparisons against ground-based remote sensing (e.g. Multi-AXis-DOAS (MAX-DOAS), direct sun Pandora, Lidar) and in-situ (e.g. surface, aircraft, balloon) measurements. These validation activities have covered both tropospheric and stratospheric NO_2 data.

Despite these validation activities large uncertainties remain. These uncertainties are partly related to the quality of the independent NO_2 data used for the validation, which itself have non-negligible uncertainties. They are also related to the issue of representativity of the often point-sized footprint of the ground-based and in-situ measurements versus the finite-sized ground pixel of the satellite.

For the validation of S4 NO_2 data, three aspects need special attention:

- Validation of the stratospheric correction as the limited spatial coverage of S4, the lack of a large clean background region and the need for stratospheric values at different local time could potentially lead to larger uncertainties in the stratospheric correction.
- Validation of the diurnal variation of the tropospheric NO_2 columns, which is a novel product for satellite sensors and thus needs special attention.
- Validation of directional surface reflectance effects as these are for the first time taken into account explicitly and for a geostationary sensor have the potential to interfere with the retrieval of the diurnal variation in NO_2 columns.

In addition to NO_2 itself, also the relevant input parameters (NO_2 vertical profile, aerosol profile, clouds, surface BRF) should be covered by validation measurements in order to quantify and, if possible, reduce uncertainties on the air mass factors.

8.2 Algorithm testing and verification

This important activity provides confidence in the retrieval algorithms, including forward and inverse models, based on simulations, and comparisons between different techniques and software programs.

This activity is part of the S4 project and covered by the S4 Geophysical Algorithm Verification subproject. In this exercise, output of the NO_2 bread-board algorithm is compared with that from the independent NO_2 verification algorithms operated by MPIC and DLR. It is expected that most software bugs and non-optimal algorithm choices will be detected and removed by this activity.

In addition, experience has shown that some algorithmic choices can only be verified and fine-tuned after launch when real data is available. This is particularly true for a mission such as S4, which includes several novel components in measurements (diurnal variation, limited geographical coverage) and algorithms (use of aerosol and surface information from the same instrument, inclusion of BRDF effects). Thus verification activities need to ideally continue after launch.

8.3 Stratospheric NO_2 validation

For stratospheric NO_2 columns, correlative (column and profile) measurements are needed in regions that are representative for the latitude bands covered by S4. This includes columns and profiles from ground-based DOAS and FTIR stations from the Network for the Detection of Atmospheric Composition Change (NDACC) as well as limb and occultation satellite observations if available. Special attention needs to be given to situations within and close to the polar vortex in spring as these are characterised by large spatial gradients, which are difficult to reproduce.

As the stratospheric correction in the NO_2 algorithm is based on assimilated NO_2 fields from the CAMS model, validation of stratospheric NO_2 fields from the CAMS system should have high priority as the quality of these fields will directly impact on the S4 stratospheric NO_2 correction. This includes validation of the stratospheric NO_2 profiles ingested and produced by the system.

8.4 Tropospheric NO_2 validation

For validation of tropospheric NO_2 data, correlative (column and profile) measurements are needed throughout Europe. NDACC-instruments unfortunately do not meet this need, as they are often located in relatively remote and clear areas.

Information on tropospheric NO_2 concentrations – with the NO_2 in the planetary boundary layer and / or in the free troposphere – comes from in-situ instruments (at the ground, on masts, or on low-flying balloons) and from remote-sensing instruments at the ground, on balloons or aircraft. The emerging suite of MAX-DOAS and PANDORA instruments are particularly valuable for validation of S4 measurements, but homogenisation and cross-calibration of these measurements should remain a priority for successful validation.

An important issue when comparing independent NO_2 measurements with data derived from satellite-based instruments is the question of representativity. We recommend a careful investigation into the spatial representativity of any independent NO_2 measurement, in order to facilitate a meaningful comparison with the S4 pixel. NO_2 mapping instruments operated on airplanes (Meier et al., 2016) will be an important source of information to tackle in particular this representativity issue but also car-DOAS measurements (Wagner et al., 2010) and MAX-DOAS measurements including many azimuthal directions (Gratsea et al., 2016) will be useful here.

Important for the validation as well as for the data assimilation system used for the stratospheric correction is a good understanding of the vertical profile of the tropospheric NO_2. The best source of information on vertical profiles of NO_2 is still from incidental aircraft campaigns. Alternatively, experimental NO_2 profiles from (tethered) balloon sondes, and measurement towers, will provide valuable information on the vertical distribution of NO_2. Vertical profiles derived from MAX-DOAS observations also provide relevant information but lack sensitivity to the upper troposphere.

Since tropospheric retrievals depend on the concept of the air-mass factor, which has to rely on a priori information, it is important to also validate the inputs and assumptions that go into the air-mass factor calculation. This mostly concerns surface BRDF and cloud parameters – cloud fraction and cloud pressure – that should be well characterised. Another critical issue, about which very little is known as yet, is the effect of the presence of aerosols on the NO_2 retrieval (Leitao et al., 2010). Thus any tropospheric NO_2 validation data set should ideally be combined with information on surface BRDF and vertical aerosol distribution.

9 Discussion and conclusions

In this ATBD, the baseline approach for the operational retrieval of tropospheric NO_2 from Sentinel-4 is described. Sentinel-4 is a geostationary satellite observing the European region with an hourly revisit time. The data product is delivered in near real-time as part of the Copernicus Atmosphere Monitoring Service. The high spatial resolution (8 x 8 km at 45° N and 0° longitude) in combination with the high temporal sampling forms an important improvement over existing data sets.

The retrieval approach follows the heritage from several previous and current polar-orbiting satellite instruments. A DOAS fit yields slant columns, which are converted to vertical columns using air mass factors. The separation between tropospheric and stratospheric NO2 is calculated using model forecasts of the stratospheric column from the CAMS systems based on assimilation of NO_2 columns from Sentinel-5 Precursor and Sentinel-5. New developments for the retrieval of NO_2 from Sentinel-4 are the use of a surface reflectance provided on a daily basis by a dedicated retrieval from the same instrument and the use of highly spatially resolved a priori NO_2 profiles in the boundary layer from regional air quality models,

The main purpose of the data product will be pollution monitoring and emission estimation. The high spatial resolution is expected to improve the spatial detail of the retrieved fields and to reduce the number of days where clouds prevent measurements. The hourly sampling enables for the first time observation from satellite of the diurnal evolution of the NO_2 burden and emission strengths over Europe.

10 References

The following list contains references to the peer-reviewed scientific literature.

[Referencing AMT style]

Aliwell, S. R., Van Roozendael, M., Johnston, P. V., Richter, A., Wagner, T., Arlander, D. W., Burrows, J. P., Fish, D. J., Jones, R. L., Tørnkvist, K. K., Lambert, J.-C., Pfeilsticker, K., and Pundt, I.: Analysis for BrO in zenith-sky spectra: An intercomparison exercise for analysis improvement, J. Geophys. Res., 107(D14), doi:10.1029./2001JD000329, 2002.

Alvarado, L. M. A.: Investigating the role of glyoxal using satellite and MAX-DOAS measurements, Ph.D. thesis, Institut für Umweltphysik, Universität Bremen, Bremen, Germany, 2016.

Alvarado, L. M. A., Richter, A., Vrekoussis, M., Wittrock, F., Hilboll, A., Schreier, S. F., and Burrows, J. P.: An improved glyoxal retrieval from OMI measurements, Atmos. Meas. Tech., 7, 4133-4150, doi:10.5194/amt-7-4133-2014, 2014.

Beirle, S., Kühl, S., Puķīte, J., and Wagner, T.: Retrieval of tropospheric column densities of NO_2 from combined SCIAMACHY nadir/limb measurements, Atmos. Meas. Tech., 3, 283-299, doi:10.5194/amt-3-283-2010, 2010.

Beirle, S., Lampel, J., Lerot, C., Sihler, H., and Wagner, T.: Parameterizing the instrumental spectral response function and its changes by a super-Gaussian and its derivatives, Atmos. Meas. Tech., 10(2), 581–598, doi:10.5194/amt-10-581-2017, 2017.

Beirle, S., Sihler, H., and Wagner, T.: Linearisation of the effects of spectral shift and stretch in DOAS analysis, Atmos. Meas. Tech., 6, 661-675, doi:10.5194/amt-6-661-2013, 2013.

Beirle, S., Hörmann, C., Jöckel, P., Liu, S., Penning de Vries, M., Pozzer, A., Sihler, H., Valks, P., and Wagner, T.: The STRatospheric Estimation Algorithm from Mainz (STREAM): estimating stratospheric NO2 from nadir-viewing satellites by weighted convolution, Atmos. Meas. Tech., 9, 2753-2779, doi:10.5194/amt-9-2753-2016, 2016.

Bertram, T. H., Heckel, A., Richter, A., Burrows, J. P., and Cohen, R. C.: Satellite measurements of daily variations in soil NO_x emissions, Geophys. Res. Lett., 32(24), L24812, 2005.

Boersma, K. F., Eskes, H. J., and Brinksma, E. J.: Error Analysis for Tropospheric NO_2 Retrieval from Space, J. Geophys. Res., 109, D04311, doi:10.1029/2003JD003962, 2004.

Boersma, K. F., Eskes, H. J., Veefkind, J. P., Brinksma, E. J., Van der A, R. J., Sneep, M., Van den Oord, G. H. J., Levelt, P. F., Stammes, P., Gleason, J. F., and Bucsela, E. J.: Near-real time retrieval of tropospheric NO_2 from OMI, Atmos. Chem. Phys., 7(8), 2103-2118, doi:10.5194/acp-7-2103-2007, 2007

Boersma, K. F., Eskes, H. J., Dirksen, R. J., Van der A, R. J., Veefkind, J. P., Stammes, P., Huijnen, V., Kleipool, Q. L., Sneep, M., Claas, J., Leitão, J., Richter, A., Zhou, Y., and Brunner, D.: An improved tropospheric NO_2 column retrieval algorithm for the Ozone Monitoring Instrument, Atmos. Meas. Tech., 4, 1905-1928, doi:10.5194/amt-4-1905-2011, 2011.

Bucsela, E. J., Krotkov, N. A., Celarier, E. A., Lamsal, L. N., Swartz, W. H., Bhartia, P. K., Boersma, K. F., Veefkind, J. P., Gleason, J. F., and Pickering, K. E.: A new stratospheric and tropospheric NO_2 retrieval algorithm for nadir-viewing satellite instruments: applications to OMI, Atmos. Meas. Tech., 6, 2607-2626, doi:10.5194/amt-6-2607-2013, 2013.

Chance, K. and Kurucz, R.: An improved high-resolution solar reference spectrum for earth's atmosphere measurements in the ultraviolet, visible, and near infrared, J. Quant. Spectrosc. Ra., 111, 1289-1295, 2010.

Chance, K., Kurosu, T. P. and Sioris, C. E.: Undersampling correction for array detector-based satellite spectrometers, Appl. Opt., 44(7), 1296-1304, doi:10.1364/AO.44.001296, 2005.

Dirksen, R. J., Boersma, K. F., Eskes, H. J., Ionov, D. V., Bucsela, E. J., Levelt, P. F., and Kelder, H. M.: Evaluation of stratospheric NO_2 retrieved from the Ozone Monitoring Instrument: Intercomparison, diurnal cycle, and trending, J. Geophys. Res. Atmos., 116(2), 1-22, doi:10.1029/2010JD014943, 2011.

Eskes, H. J. and Boersma, K. F.: Averaging kernels for DOAS total-column satellite retrievals, Atmos. Chem. Phys., 3, 1285-1291, doi:10.5194/acp-3-1285-2003, 2003.

Fish, D. J. and Jones, R. L.: Rotational Raman scattering and the ring effect in zenith-sky spectra, Geophys. Res. Lett., 22(7), 811-814, doi:10.1029/95GL00392, 1995.

Franke, K., Richter, A., Bovensmann, H., Eyring, V., Jöckel, P., and Burrows, J.P.: Ship emitted NO2 in the Indian Ocean: comparison of model results with satellite data, Atmos. Chem. Phys., 9, 7289-7301, 2009.

Gorshelev, V., Serdyuchenko, A., Weber, M., Chehade, W., and Burrows, J. P.: High spectral resolution ozone absorption cross-sections – Part 1: Measurements, data analysis and comparison with previous measurements around 293 K, Atmos. Meas. Tech., 7, 609-624, doi:10.5194/amt-7-609-2014, 2014.

Gratsea, M., Vrekoussis, M., Richter, A., Wittrock, F., Schönhardt, A., Burrows, J., Kazadzis, S., Mihalopoulos, N., and Gerasopoulos, E.: Slant Column MAX-DOAS measurements of nitrogen dioxide, formaldehyde, glyoxal and oxygen dimer in the urban environment of Athens, Atmos. Environ., 135, 118–131, doi:10.1016/j.atmosenv.2016.03.048, 2016.

Heckel, A., Kim, S.-W., Frost, G. J., Richter, A., Trainer, M., and Burrows, J. P.: Influence of low spatial resolution a priori data on tropospheric NO_2 satellite retrievals, Atmos. Meas. Tech., 4, 1805-1820, doi:10.5194/amt-4-1805-2011, 2011.

Hilboll, A., Richter, A., and Burrows, J. P.: Long-term changes of tropospheric NO_2 over megacities derived from multiple satellite instruments, Atmos. Chem. Phys., 13, 4145-4169, doi:10.5194/acp-13-4145-2013, 2013a.

Hilboll, A., Richter, A., Rozanov, A., Hodnebrog, Ø., Heckel, A., Solberg, S., Stordal, F., and Burrows, J. P.: Improvements to the retrieval of tropospheric NO_2 from satellite – stratospheric correction using SCIAMACHY limb/nadir matching and comparison to Oslo CTM2 simulations, Atmos. Meas. Tech., 6, 565-584, doi:10.5194/amt-6-565-2013, 2013b.

Huijnen, V., Eskes, H. J., Poupkou, A., Elbern, H., Boersma, K. F., Foret, G., Sofiev, M., Valdebenito, A., Flemming, J., Stein, O., Gross, A., Robertson, L., D'Isidoro, M., Kioutsioukis, I., Friese, E., Amstrup, B., Bergstrom, R., Strunk, A., Vira, J., Zyryanov, D., Maurizi, A., Melas, D., Peuch, V.-H., and Zerefos, C.: Comparison of OMI NO_2 tropospheric columns with an ensemble of global and European regional air quality models, Atmos. Chem. Phys., 10, 3273-3296, doi:10.5194/acp-10-3273-2010, 2010.

Kim, J.: GEMS (Geostationary Enviroment Monitoring Spectrometer) onboard the GeoKOMPSAT to monitor air quality in high temporal and spatial resolution over Asia-Pacific region, in EGU General Assembly, Vienna, Austria, 22– 27 April 2012, EGU2012-4051, 2012.

Kim, S.-W., Heckel, A., McKeen, S. A., Frost, G. J., Hsie, E.-Y., Trainer, M. K., Richter, A., Burrows, J. P., Peckham, S. E., and Grell, G. A.: Satellite observed U.S. power plant NO_x emission reductions and their impact on air quality, Geophys. Res. Lett., 33, L22812, doi:10.1029/2006GL027749, 2006.

Kleipool, Q. L., Dobber, M. R., De Haan, J. F., and Levelt, P. F.: Earth surface reflectance climatology from 3 years of OMI data, J. Geophys. Res., 113, D18308, doi:10.1029/2008JD010290, 2008.

Lamsal, L. N., Krotkov, N. A., Celarier, E. A., Swartz, W. H., Pickering, K. E., Bucsela, E. J., Gleason, J. F., Martin, R. V., Philip, S., Irie, H., Cede, A., Herman, J., Weinheimer, A., Szykman, J. J., and Knepp, T. N.: Evaluation of OMI operational standard NO_2 column retrievals using in situ and surface-based NO_2 observations, Atmos. Chem. Phys., 14(21), 11587–11609, doi:10.5194/acp-14-11587-2014, 2014.

Leitão, J., Richter, A., Vrekoussis, M., Kokhanovsky, A., Zhang, Q. J., Beekmann, M., and Burrows, J. P.: On the improvement of NO_2 satellite retrievals – aerosol impact on the airmass factors, Atmos. Meas. Tech., 3, 475-493, 2010.

Leue, C., Wenig, M., Wagner, T., Platt, U., and Jähne, B.: Quantitative analysis of NO_x emissions from GOME satellite image sequences, J. Geophys. Res.,106, 5493-5505, 2001.

Litvinov, P., Hasekamp, O., and Cairns, B.: Models for surface reflection of radiance and polarized radiance: Comparison with airborne multi-angle photopolarimetric measurements and implications for modeling top-of-atmosphere measurements, Remote Sens. Environ., 115, 781-792, doi:10.1016/j.rse.2010.11.005, 2011.

Lorente, A., Boersma, K. F., Yu, H., Dörner, S., Hilboll, A., Richter, A., Liu, M., Lamsal, L. N., Barkley, M., De Smedt, I., Van Roozendael, M., Wang, Y., Wagner, T., Beirle, S., Lin, J. T., Kroktov, N., Stammes, P., Wang, P., Eskes, H. J., and Krol, M.: Structural uncertainty in air mass factor calculation for NO_2 and HCHO satellite retrievals, Atmos. Meas. Tech., 10, 759–782, doi:10.5194/amt-10-759-2017, 2017.

Martin, R. V., Chance, K., Jacob, D. J., Kurosu, T. P., Spurr, R. J. D., Bucsela, E., Gleason, J. F., Palmer, P. I., Bey, I., Fiore, A. M., Li, Q., Yantosca, R. M., and Koelemeijer, R. B.: An improved retrieval of tropospheric nitrogen dioxide from GOME, J. Geophys. Res, 107, 4437-4456, 2002.

Meier, A. C., Schönhardt, A., Bösch, T., Richter, A., Seyler, A., Ruhtz, T., Constantin, D.-E., Shaiganfar, R., Wagner, T., Merlaud, A., Van Roozendael, M., Belegante, L., Nicolae, D., Georgescu, L. and Burrows, J. P.: High-resolution airborne imaging DOAS-measurements of NO_2 above Bucharest during AROMAT, Atmos. Meas. Tech., 10, 1831–1857, doi:10.5194/amt-10-1831-2017, 2017.

Merchant, C. J., Paul, F., Popp, T., Ablain, M., Bontemps, S., Defourny, P., Hollmann, R., Lavergne, T., Laeng, A., de Leeuw, G., Mittaz, J., Poulsen, C., Povey, A. C., Reuter, M., Sathyendranath, S., Sandven, S., Sofieva, V. F., and Wagner, W.: Uncertainty information in climate data records from Earth observation, Earth Syst. Sci. Data, 9, 511-527, https://doi.org/10.5194/essd-9-511-2017, 2017.

Miyazaki, K., Eskes, H. J., Sudo, K., Takigawa, M., Van Weele, M., and Boersma, K. F.: Simultaneous assimilation of satellite NO_2, O_3, CO, and HNO_3 data for the analysis of tropospheric chemical composition and emissions, Atmos. Chem. Phys., 12, 9545-9579, doi:10.5194/acp-12-9545-2012, 2012.

Noël, S., Bramstedt, K., Bovensmann, H., Gerilowski, K., Burrows, J. P., Standfuss, C., Dufour, E., and Veihelmann, B.: Quantification and mitigation of the impact of scene inhomogeneity on Sentinel-4 UVN UV-VIS retrievals, Atmos. Meas. Tech., 5, 1319-1331, doi:10.5194/amt-5-1319-2012, 2012.

Noguchi, K., Richter, A., Rozanov, V., Rozanov, A., Burrows, J. P., Irie, H., and Kita, K.: Effect of surface BRDF of various land cover types on geostationary observations of tropospheric NO_2, Atmos. Meas. Tech., 7, 3497-3508, doi:10.5194/amt-7-3497-2014, 2014.

Platt, U. and Stutz, J.: Differential Optical Absorption Spectroscopy: Principles and Applications, Springer Verlag, Berlin, Germany, 2008.

Pope, R. M. and Fry, E. S.: Absorption spectrum (380–700 nm) of pure water, II. Integrating cavity measurements, Appl. Optics, 36, 8710–8723, doi:10.1364/AO.36.008710, 1997.

Puķīte, J., Kühl, S., Deutschmann, T., Platt, U., and Wagner, T.: Extending differential optical absorption spectroscopy for limb measurements in the UV, Atmos. Meas. Tech., 3, 631-653, doi:10.5194/amt-3-631-2010, 2010.

Richter, A. and Burrows, J. P.: A multi-wavelength approach to the retrieval of tropospheric NO_2 from GOME measurements, in: Proceedings of the ERS-ENVISAT symposium, Gothenburg, Sweden, October 2000, ESA publication SP-461, available at: http://earth.esa.int/pub/ESA DOC/gothenburg/244richt.pdf, 2000.

Richter, A. and Burrows, J. P.: Retrieval of Tropospheric NO_2 from GOME Measurements, Adv. Space Res., 29(11), 1673-1683, 2002.

Richter, A. and Wagner, T.: Solar Backscattered Radiation: UV, Visible and Near IR – Trace Gases, in: The Remote Sensing of Atmospheric Composition from Space, J. P. Burrows, U. Platt, P. Borrell (Eds.), Springer Verlag, Berlin, Germany, 2011.

Richter, A., Eyring, V., Burrows, J. P., Bovensmann, H., Lauer, A., Sierk, B., and Crutzen, P. J.: Satellite Measurements of NO_2 from International Shipping Emissions, Geophys. Res. Lett., 31, L23110, doi:10.1029/2004GL020822, 2004.

Richter, A., Burrows, J. P., Nüß, H., Granier, C, Niemeier, U.: Increase in tropospheric nitrogen dioxide over China observed from space, Nature, 437, 129-132, doi: 10.1038/nature04092, 2005.

Richter, A., Begoin, M., Hilboll, A., and Burrows, J. P.: An improved NO_2 retrieval for the GOME-2 satellite instrument, Atmos. Meas. Tech., 4, 1147-1159, doi:10.5194/amt-4-1147-2011, 2011.

Rodgers, C.D.: Inverse methods for atmospheric sounding: Theory and practice, World Scientific Publishing, Singapore, 2000.

Rothman, L. S., et al.: The HITRAN 2012 molecular spectroscopic database, J. Quant. Spectrosc. Ra., 130, 4-50, doi:10.1016/j.jqsrt.2013.07.002, 2013.

Rozanov, V. V. and Rozanov, A. V.: Relationship between different approaches to derive weighting functions related to atmospheric remote sensing problems, J. Quant. Spectrosc. Ra., 105, 217-242, doi:10.1016/j.jqsrt.2006.12.006, 2007.

Rozanov, V. V. and Rozanov, A. V.: Differential optical absorption spectroscopy (DOAS) and air mass factor concept for a multiply scattering vertically inhomogeneous medium: theoretical consideration, Atmos. Meas. Tech., 3, 751-780, doi:10.5194/amt-3-751-2010, 2010.

Rozanov, V. V., Rozanov, A. V., Kokhanovsky, A. A., and Burrows, J. P.: Radiative Transfer through Terrestrial Atmosphere and Ocean: Software Package SCIATRAN, J. Quant. Spectrosc. Ra., 133, 13-71, doi:10.1016/j.jqsrt.2013.07.004, 2014.

Schaepman-Strub, G., Schaepman, M. E., Painter, T. H., Dangel, S., and Martonchik, J. V.: Reflectance quantities in optical remote sensing–definitions and case studies, Remote Sens. Environ., 103, 27-42, doi:10.1016/j.rse.2006.03.002, 2006.

Schreier, S. F., Richter, A., Kaiser, J. W., and Burrows, J. P.: The empirical relationship between satellite-derived tropospheric NO_2 and fire radiative power and possible implications for fire emission rates of NO_x, Atmos. Chem. Phys., 14, 2447-2466, doi:10.5194/acp-14-2447-2014, 2014.

Serdyuchenko, A., Gorshelev, V., Weber, M., Chehade, W., and Burrows, J. P.: High spectral resolution ozone absorption cross-sections – Part 2: Temperature dependence, Atmos. Meas. Tech., 7, 625-636, doi:10.5194/amt-7-625-2014, 2014.

Thalman, R. and Volkamer, R.: Temperature dependent absorption cross-sections of O_2-O_2 collision pairs between 340 and 630 nm and at atmospherically relevant pressure, Phys. Chem. Chem. Phys., 15(37), 15371-15381, doi:10.1039/C3CP50968K, 2013.

Thomas, G. E. and Stamnes, K.: Radiative transfer in the atmosphere and ocean, Cambridge University Press, Cambridge, United Kingdom, 2002.

Tilstra, L. G., Tuinder, O. N. E., Wang, P., and Stammes, P.: Surface reflectivity climatologies from UV to NIR determined from Earth observations by GOME-2 and SCIAMACHY, J. Geophys. Res., 122, 4084-4111, doi:10.1002/2016JD025940, 2017.

Valks, P., Pinardi, G., Richter, A., Lambert, J.-C., Hao, N., Loyola, D., Van Roozendael, M., and Emmadi, S.: Operational total and tropospheric NO_2 column retrieval for GOME-2, Atmos. Meas. Tech., 4, 1491-1514, doi:10.5194/amt-4-1491-2011, 2011.

Vandaele, A., Hermans, C., Simon, P., Carleer, M., Colin, R., Fally, S., Mérienne, M., Jenouvrier, A., and Coquart, B.: Measurements of the NO_2 absorption cross-section from 42 000 cm-1 to 10 000 cm-1 (238–1000 nm) at 220 K and 294 K, J. Quant. Spectrosc. Ra., 59, 171-184, 1998.

Van de Hulst, H. C.: Multiple light scattering: Tables, formulas, and applications, Academic Press, New York, United States, 1980.

Van Diedenhoven, B., Hasekamp, O. P., and Landgraf, J.: Retrieval of cloud parameters from satellite-based reflectance measurements in the ultraviolet and the oxygen A-band, J. Geophys. Res., 112, D15208, doi:10.1029/2006JD008155, 2007.

Van Geffen, J. H. G. M., Boersma, K. F., Van Roozendael, M., Hendrick, F., Mahieu, E., De Smedt, I., Sneep, M., and Veefkind, J. P.: Improved spectral fitting of nitrogen dioxide from OMI in the 405–465 nm window, Atmos. Meas. Tech., 8(4), 1685–1699, doi:10.5194/amt-8-1685-2015, 2015.

Vasilkov, A., Qin, W., Krotkov, N., Lamsal, L., Spurr, R., Haffner, D., Joiner, J., Yang, E.-S., and Marchenko, S.: Accounting for the effects of surface BRDF on satellite cloud and trace-gas retrievals: a new approach based on geometry-dependent Lambertian equivalent reflectivity applied to OMI algorithms, Atmos. Meas. Tech., 10, 333-349, doi:10.5194/amt-10-333-2017, 2017.

Vountas, M., Rozanov, V. V., and Burrows, J. P.: Ring Effect: Impact of rotational Raman Scattering on Radiative Transfer in Earth's Atmosphere, J. Quant. Spectrosc. Ra., 60(6), 943-961, 1998.

Vountas, M., Richter, A., Wittrock, F., and Burrows, J. P.: Inelastic scattering in ocean water and its impact on trace gas retrievals from satellite data, Atmos. Chem. Phys., 3, 1365-1375, 2003.

Wagner, T., Ibrahim, O., Shaiganfar, R. and Platt, U.: Mobile MAX-DOAS observations of tropospheric trace gases, Atmos. Meas. Tech., 3(6), doi:doi:10.5194/amt-3-129-2010, 2010.

Zara et al., in preparation.

Zhang, Q., Streets, D. G., and He, K.: Satellite observations of recent power plant construction in Inner Mongolia, China, Geophys. Res. Lett., 36, L15809, doi:10.1029/2009GL038984, 2009.

Zien, A. W., Richter, A., Hilboll, A., Blechschmidt, A.-M., and Burrows, J. P.: Systematic analysis of tropospheric NO_2 long-range transport events detected in GOME-2 satellite data, Atmos. Chem. Phys., 14, 7367-7396, doi:10.5194/acp-14-7367-2014, 2014.

Zoogman, P., et al.: Tropospheric emissions: Monitoring of pollution (TEMPO), J. Quant. Spectrosc. Ra., in press, doi:10.1016/j.jqsrt.2016.05.008, 2016.